Title
Numerical Investigation of Operational Shocks and Vibrations in Mobile Hard Disk Drives

Author
Rai, Rahul

Publication Date
2011

Peer reviewed|Thesis/dissertation

Numerical Investigation of Operational Shocks and Vibrations in Mobile Hard Disk Drives

by

Rahul Rai

A dissertation submitted in partial satisfaction of the

requirements for the degree of

Doctor of Philosophy

in

Engineering–Mechanical Engineering

in the

Graduate Division

of the

University of California, Berkeley

Committee in charge:

Professor David B. Bogy, Chair
Professor Tarek I. Zohdi
Professor Jon Wilkening

Fall 2011

Numerical Investigation of Operational Shocks and Vibrations in Mobile Hard Disk Drives

by

Rahul Rai

Abstract

Numerical Investigation of Operational Shocks and Vibrations in Mobile Hard Disk Drives

by

Rahul Rai

Doctor of Philosophy in Engineering–Mechanical Engineering

University of California, Berkeley

Professor David B. Bogy, Chair

Over the last decade, there has been a continuous increase in the demand of hard disk drives (HDDs) for the mobile applications. In such devices, HDDs are often subjected to mechanical shocks and vibrations. Such external disturbances can degrade the read/write (R/W) performance of mobile drives and in extreme cases it can even cause the loss of stored magnetic information. Hence the ability of the head-disk interface (HDI) to withstand such excitation becomes critical in determining the reliability of a mobile disk drive. This dissertation presents a simulation method to accurately model the response of a mobile HDD to external disturbances which can aid the design process.

A numerical investigation was conducted on a 2.5 inch form factor laptop drive to understand the dynamics of the HDI during dynamic events such as operational shocks. A detailed model for the mobile disk drive was developed which includes a spinning disk, a fluid dynamic bearing (FDB) based spindle motor, a base plate and an actuator. The behavior of the HDI subjected to various disturbances was determined by solving a fluid-structure interaction problem in which a spinning disk and a head (slider) were coupled through an air bearing. Case studies were conducted to determine the effect of parameters like shock pulse width, HDD orientation, parking ramp contact and FDB dynamic coefficients on the performance of a HDD during the excitation.

It was observed that the proximity of the pulse to the HDD component's natural frequencies has an adverse effect on the shock resistance of the HDI. Furthermore, the orientation of the HDD during the shock can also affect the stability of the HDI. In the case of planar excitations, the FDB dynamics becomes critical in determining the slider's vibration amplitude. This knowledge about the HDI failure mechanism and its vibration characteristics can be helpful in designing a mobile HDD with a better shock performance.

To my Parents

Contents

List of Figures

List of Tables

List of Abbreviations

ABS	Air Bearing Surface
BB	Ball Bearing
BC	Boundary Condition
BEM	Boundary Element Method
BMR	Bit Patterned Media Recording
CML	Computer Mechanics Laboratory
CMS	Component Mode Synthesis
CSS	Contact Start Stop
DOF	Degree of Freedoms
FDB	Fluid Dynamic Bearing
FDM	Finite Difference Method
FEM	Finite Element Method
FFT	Fast Fourier Transform
FH	Flying Height
FVM	Finite Volume Method
GH	Glide Height
HAMR	Heat Assisted Magnetic Recording

HDD	Hard Disk Drive
HGA	Head Gimbal Assembly
HMS	Head Media Spacing
HSA	Head Stack Assembly
ID	Inner Diameter
IRS	Iterative Reduction Scheme
L/UL	Load/Unload
MD	Middle Diameter
NFH	Nominal Flying Height
NRRO	Non Repeatable Run Out
OD	Outer Diameter
ODE	Ordinary Differential Equation
PDE	Partial Differential Equation
R/W	Read/Write
TFC	Thermal Flying Controlled
TPI	Tracks Per Inch
VCM	Voice Coil Motor

Acknowledgments

First and foremost I would like to thank my advisor, Prof. David Bogy for his supervision during my doctoral studies at UC Berkeley. I am grateful to him for not only his excellent technical advice, but also the professional development that I received under him. Throughout my research career he has given me the freedom to explore research areas of my interest while at the same time not letting me stray off course. I am really fortunate to have him both as an advisor and a mentor.

During my research at Computer Mechanics Laboratory, I had a great opportunity to interact with the members for the hard drive industry. In particular, I would like to thank Jih-Ping Peng of Western Digital Corporation and Samuel Gan of Seagate Technologies Singapore for their helpful discussions and insightful feedbacks.

A big thanks is also due to fellow CMLers. Technical discussions with them have helped me gain a broader education. Brendan Cox, Vineet Gupta, Puneet Bhargava and Dolfakar Adnan Al Emara deserve a special thanks.

Life in Berkeley would not have been so much enjoyable without my wonderful friends. More than friends, Siddharth Dey, Shashank Nawathe, Shradha Sanghvi and Pallavi Joshi have been an extended family to me.

Finally, I attribute all my success to my wonderful family. I am indebted to them for their sacrifices and unconditional love throughout my life. Last but not the least, I would like to thank my soon to be wife Rashmeet Sangari, for her immense love and support throughout my stay in graduate school.

Chapter 1

Introduction

A hard disk drive (HDD) is a non-volatile, random access device used for storing digital information on the magnetic surfaces of spinning disks. The first generations of hard disk drives were introduced back in the mid -1950's. They had a limited storage capacity of 5MB and weighed more than a ton! The HDD technology has improved a lot since then. These days a pocket size portable drive can store more than 500GB of digital data. Conventionally HDDs have been used for data storage in devices like desktop computers and enterprise servers where their exposure to external disturbance is minimal. However, over the past decade, there has been continuous increase in the demand of HDDs for mobile applications where they are often subject to harsh working environments. The research presented in this dissertation is focused on understanding the issues related to mechanical performance of HDDs in mobile devices. The following section describes the basic working principals of a hard disk drive followed by a section on the brief history of the evolution of HDD technology. The motivation behind the current research with its specific goals are also presented in this chapter, and it concludes with a brief overview of this dissertation.

1.1 Basics

A typical modern hard disk is shown in Fig. 1.1. It consist of multiple disks (usually 2 or 3) mounted on a spindle rotating at a RPM that can range from 5400 in mobile drives to 15000 in enterprise drives. The HDD modeled here contains one read/write head for each side of the disk surface. This read/write head is embedded in a slider which is mounted on a suspension. This slider–suspension assembly is known as head gimbal assembly (HGA).

The suspension is attached to an "E-Block" arm that gets actuated by a voice coil motor (VCM). This enables the head to access the data tracks across the radius on a disk. The HGA–E-Block-VCM together is known as head stack assembly (HSA).

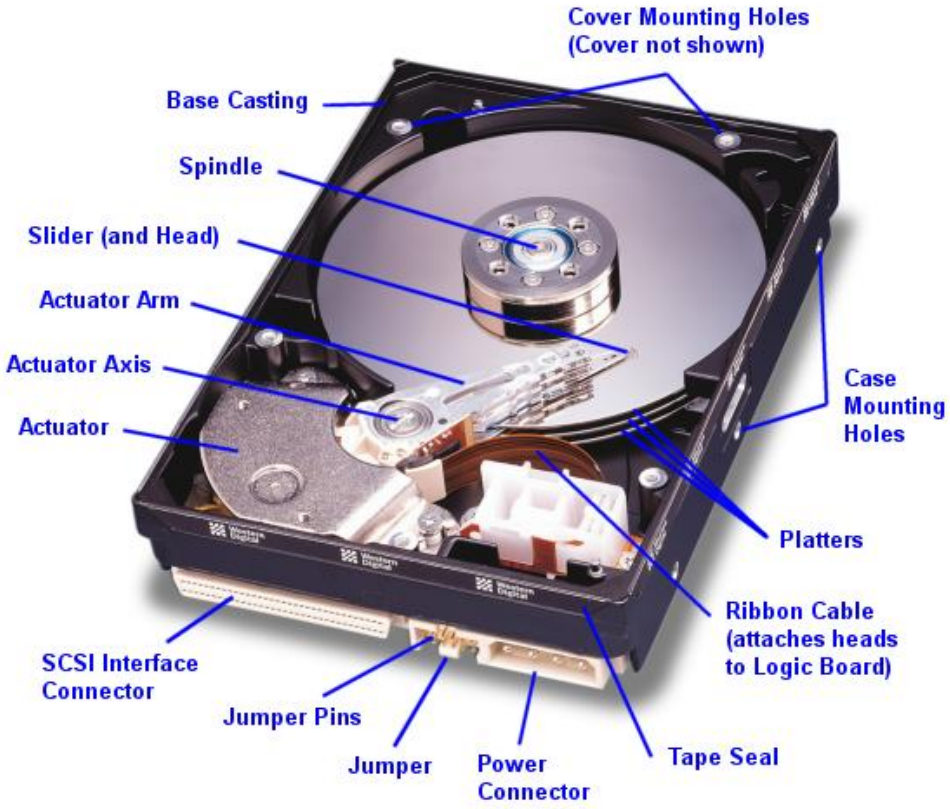

Figure 1.1: Basic components of a hard disk drive [PC Guide]

The disks used in HDDs are very smooth with RMS value for roughness ~ 0.2 nm. These are usually made of aluminum or glass substrate with multiple layers deposited on the top of it (Fig. 1.2). The digital information is stored by magnetically polarizing the grains present in the ferromagnetic layer, which is about 30 nm thick. A thin (1–3 nm) carbon overcoat layer (Diamond like carbon or DLC) is present on the top of magnetic layer to protect it from wear and corrosion. A thin layer (1 nm) of a long chain polymer lubricant is provided on the top of DLC layer in order to increase the durability of head-disk interface.

When a slider is moved onto the spinning disk, the suspension presses it against the disk by applying a fixed *preload*. The spinning action of the disk causes an air flow that applies pressure on the surface of the slider. This counter pressure on the slider balances the applied suspension force and causes the slider to lift up, *fly*, on the spinning disk (Fig. 1.3). The

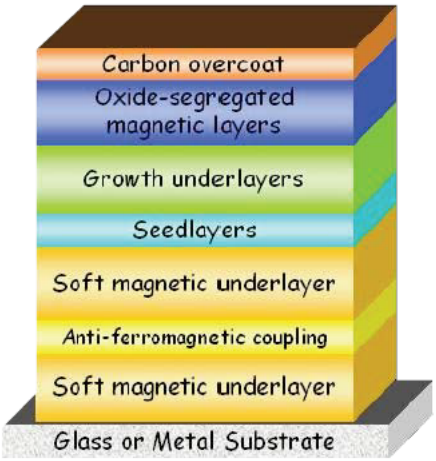

Figure 1.2: Layered structure of a perpendicular media disk [Hitachi 2007b]

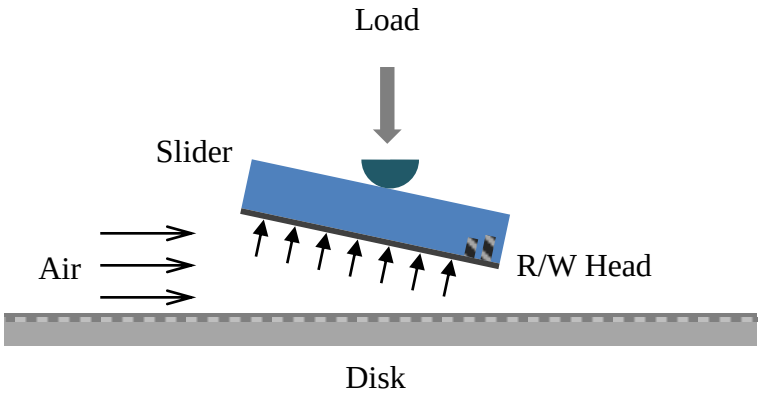

Figure 1.3: Basic working principal of a HDI

mechanical clearance between the read/write head and the disk is known as *flying height* of the slider. A special design is etched on the slider surface facing the disk. It is called the air bearing surface (ABS). The etch depths and design on the ABS controls the air flow under the slider and determines its flying attitude. The strength of the read back signal depends on the separation between the head (usually located at the trailing edge of the slider) and the magnetic layer. This distance is known as head-media separation (HMS). The high areal densities of current HDDs[1] requires the HMS to be less than 10 nm, which results in a flying height of less than 5 nm. This low mechanical spacing has been achieved by thermal flying height controlled slider technology [Kurita et al. 2005; Shiramatsu et al. 2008]. This technology uses a special slider in which a heater is embedded in the vicinity of the read/write head. When the power is tuned on, heater produces a thermal protrusion near the trailing edge which brings the HMS to the required range.

1.2 Evolution

The first hard disk drive was invented by a team of engineers lead by Reynold B. Johnson at IBM in 1956 [Source: Wikipedia]. It was called RAMAC (Random Access Method of Accounting and Control) (Fig. 1.4) and it contained 50 disks, each of them being 2 feet in diameter. This drive assembly was enormous in size and weighed more than a ton! Disk rotated at 1200 RPM, and had an areal density of 100 Bits/in^2 [Source: IBM]. It had total capacity of 5 MB and could be leased at $3200 per month.

HDD technology have came a long way since then. Recently Seagate Technology has released the Momentus® (Fig. 1.5), an ultra thin laptop drive [Source: Seagate]. This disk drive has a thickness of 7 mm and weighs less than 100 gms. It operates at 7200 RPM and has an areal density of more than 400 GBits/in^2. The model with the highest storage capacity of 320 GB cost around $100.

This incredible growth in the storage capacity has been achieved by reducing the size of the recording bit. Fig. 1.6 summarizes the trends in the areal density growth over the past 55 years. This improvement in the recording technology has reduced the storage cost ($/MB) made HDD's more affordable. A good summary about the evolution of magnetic recording technology has been provided in Daniel, Mee, and Clark [1999].

[1]The *areal density* is defined as amount of digital data that can be stored in a unit area of recording medium. It is usually expressed in bits per sq. inch.

Figure 1.4: The first hard disk drive - IBM 305 RAMAC [IBM]

Figure 1.5: The Seagate Momentus® [Seagate]

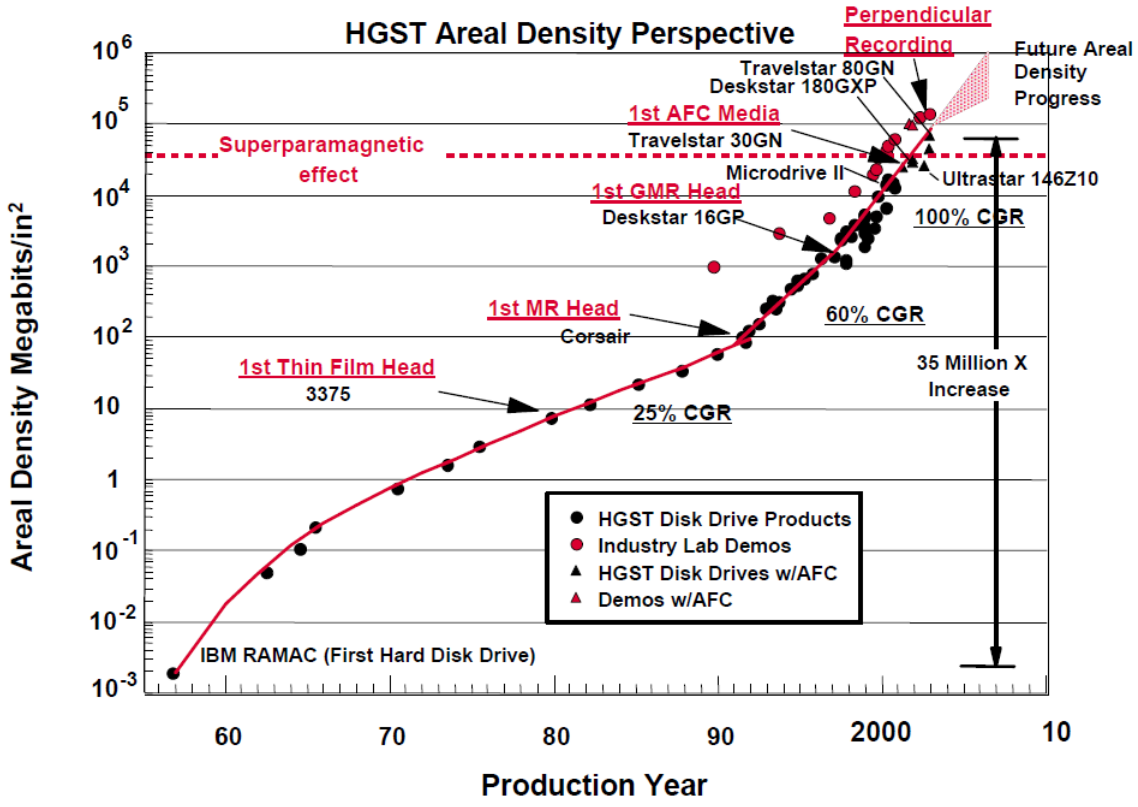

Figure 1.6: Areal density growth trends [Hitachi 2003]

In order to compete with the solid state drives (SSD), hard disk drive industry is exploring various technological options to push for ultra high areal density (> 10 TB/in^2) beyond the superparamagnetic limit [Shiroishi et al. 2009; Park et al. 2011]. One of the most promising of them is heat assisted magnetic recording (HAMR). In this technology, a laser is used to heat the ferromagnetic media to reduce its coercivity (Fig. 1.7). After the media cools the coercivity again increases, and this allows a much smaller recording bit without reaching the superparamagentic limit [Rottmayer et al. 2006; Kryder et al. 2008]. Due to the involvement of a laser, the biggest challenge here is to design a robust HDI for proper heat management. An alternative approach is the bit pattern media recording [Albrecht et al. 2002; Li and Talke 2009]. In this method, smaller bit size is achieved by storing them of an individual magnetic island of dimension around 10 nm (Fig. 1.8). The manufacturing technology required to produce the features in 10 nm scale has not been completely developed yet. A combination of these two technologies can help the hard disk drive industry to remain competent in the digital storage business.

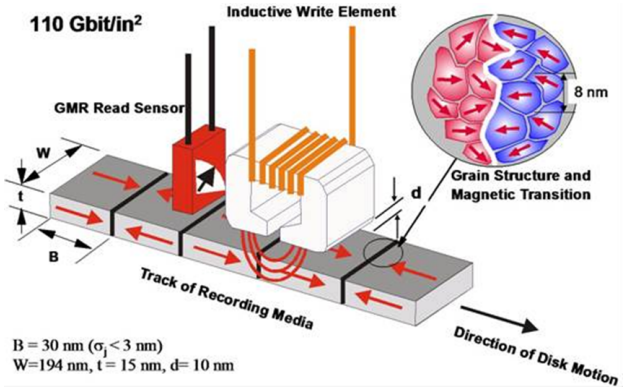

Figure 1.7: Heat assisted magnetic recording [INSIC]

1.3 Motivation

Over the past decade, the use of disk drives have been expanded from conventional desktop computers to mobile platforms like laptops, digital video recorders, video game consoles and automobiles to name a few. In contrast to a conventional computer, where a HDD remains stationary for its lifetime, in the mobile applications disk drives are often used in a harsh working environment. In such operating conditions, HDDs are often subjected

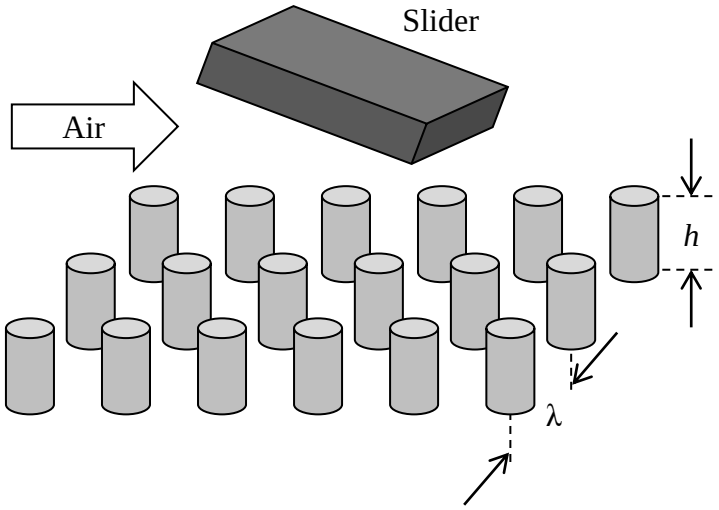

Figure 1.8: Bit pattern media recording

to mechanical disturbances which can degrade their R/W performance, and in the worst scenario it can lead to the loss of magnetic information. Furthermore, the increase in areal and track density[2] has left a very tight tolerance for permissible in-plane and out of plane vibration of the slider. Hence in order to increase the reliability of the HDD, it is important to design a robust head disk interface which can withstand any typical external disturbance. An ability to accurately simulate the response of a HDI during a dynamic event like a shock or a vibration can aid the design process.

In the past, there have been various investigations conducted to study the slider dynamics during a mechanical shock. Much of the earlier work [Kumar et al. 1994; Kouhei et al. 1995; Lin 2002] was focused on evaluating the performance of the HDD during the non-operating conditions. But with the introduction of load/unload technology, wherein the head is moved onto a ramp out past the outer radius of the disk, the problems with non-operational shocks has been reduced, and the focus has shifted to the operational state. Jiang et al. numerically studied the slider dynamics during an operational shock. They developed a detailed model for the disk but the air bearing and suspension were modeled as set of linear springs. In an alternative approach, Harrison and Mundt in their study used a detailed air bearing model. They measured the disk response under the slider and used it as an input for evaluating the FH numerically. Due to difficulty of making measurements for each case, this procedure

[2]The *track density* is defined as the number of tracks present in unit radial length. It is usually expressed in track per inch (TPI).

was inconvenient in practice. In 2002, Zeng and Bogy proposed a finite element (FE) based approach to study the HDI dynamics. It was a two-step process. In the first step, a structural dynamics problem was solved in which the air bearing was represented as a linear spring. The stiffness for air bearing was evaluated by solving the perturbed Reynold's equation. In the second step, the component displacements evaluated in the previous step were used as an input to solve the Reynold's equation for computing the slider's flying attitude. This approach was based on the assumption that the two simulations remain uncoupled. This approximation gives good results when the excitation magnitudes are small. However, for a large modulation in the slider attitude, the perturbation analysis cannot be used to evaluate the air bearing dynamic coefficients. Later this method was adopted by Jayson et al. to study the effect of air bearing design on the shock performance [Jayson et al. 2003a; Murthy et al. 2006]. Jang et. al. [Jang et al. 2006; Jang and Seo 2007] extended the finite element approach to include more details present in a disk drive. However, the air bearing was still modeled as linear springs in all these FE based models. To overcome this, Bhargava and Bogy proposed a new coupled approach to solve the operational shock problem. In their method, the structural dynamics and Reynold's equation for the air bearing were solved simultaneously using the fixed point iteration method. This method offered a better accuracy in predicting HDI dynamics when compared to the previous counterparts. However, in their study the disk was modeled as stationary, which is a good approximation for a spinning disk only for the case of axi-symmetric excitation. Thus this model was unable to capture the HDI response for a generalized disturbance which involves disk asymmetric motion. This motivated us to focus our efforts in developing a comprehensive model for a mobile hard disk drive that can be used to predict the behavior of the disk-air bearing-slider system for any general excitation.

1.4 Objectives

Briefly, *the objective of this research is to develop an accurate model for a mobile hard disk drive to study the head-disk interface dynamics during a shock or a vibration event.*

1.5 Outline

This dissertation is divided into 7 chapters. The chapter 1 gives a brief overview of the hard disk drive technology and its evolution over the past 60 years. A numerical model for a spinning disk is introduced in the chapter 2. Chapter 3 gives the details about the modeling of the disk support system, which consist of a spindle motor and a base plate. Chapter 4 describes the details about the fluid-structure interaction problem required to be solved for simulating the HDI dynamics. Chapter 5 presents a numerical study on the vertical operational shocks in a mobile HDD. The effect of component dynamics, excitation frequency and disk orientation on the shock performance of the HDI has been discussed in this chapter. A study of in-plane disturbances is presented in chapter 6. The final chapter 7 contains a summary of the significant findings from the current research and discusses the possible avenues for the future research.

Chapter 2

Dynamics of a spinning disk

To predict the behavior of the head-disk interface during a dynamic event, we must accurately capture the dynamics of the spinning disk. In the previous studies [Zeng and Bogy 2002; Bhargava and Bogy 2007], researchers used a stationary disk model to predict the response of a rotating disk. This approximation is valid for the case when the disk is symmetrically excited along its axis of rotation. However, this assumption does not hold for the case of an oblique shock. Even for a perfectly vertical excitation, the asymmetry present in the design of base plate can excite the disk in its non-axisymmetric modes. In order to overcome the above mentioned shortcomings, we introduce a new spinning disk model in this chapter. The following sections contain the details about the governing equation of a rotating disk and the numerical scheme used to solve it. A validation study for the spinning disk model presented is presented in the end of this chapter.

2.1 Governing Equation

Many researchers in the past have investigated the dynamics of a spinning disk. Most of these studies have been based on the original work by Lamb and Southwell in 1921. In their work, they modeled the disk as a spinning membrane and added the bending stiffness to it. However, this method neglects the in-plane and rotatory inertia of the disk. To overcome this shortcoming, in 2001 Baddour [Baddour and Zu 2001a,b] proposed a method to derive the governing equations based on the Hamiltonian principle. In this approach, they have used the linear *Kirchoff* plate theory and non-linear *von Karman* strain expressions to derive the equations of motion for a spinning flexible disk, which is presented in this section.

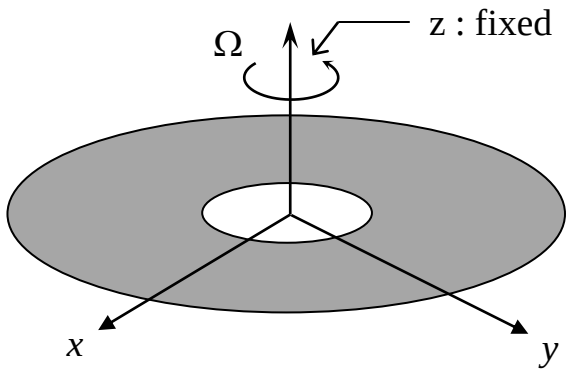

Figure 2.1: A schematic diagram of a spinning disk

Fig. 2.1 shows a schematic diagram of a spinning disk. The disk rotates with a constant angular speed Ω about the fixed vertical z axis. For an isotropic-linearly elastic disk, the governing equation for the in-plane motion is:

$$\rho h \Omega^2 r + \frac{\partial q_r}{\partial r} + \frac{q_r - q_\theta}{r} = 0 \tag{2.1}$$

where ρ is the density of the disk, h is its thickness, and q_r and q_θ are the linearized internal forces in the radial and circumferential directions respectively. They can be expressed in terms of the radial displacement u and membrane rigidity of the disk $D^\circ = Eh/(1-\nu^2)$ as:

$$q_r = D^\circ \left(\frac{\partial u}{\partial r} + \nu \frac{u}{r} \right) \tag{2.2a}$$

$$q_\theta = D^\circ \left(\frac{u}{r} + \nu \frac{\partial u}{\partial r} \right) \tag{2.2b}$$

where E and ν are the Young's modulus and Poisson's ratio of the disk material. By substituting the expression for the internal forces (eq. 2.2), we can express the equation of planar motion (eq. 2.1) in terms of the radial displacement u as follows:

$$\frac{\partial^2 u}{\partial r^2} + \frac{\partial u}{r \partial r} - \frac{u}{r^2} = -\frac{\rho h \Omega^2}{D^\circ} r \tag{2.3}$$

In the configuration shown in Fig. 2.1, the disk is fixed at it's inner rim ($r = r_i$) and the outer edge ($r = r_o$) is traction free. The corresponding boundary conditions can be expressed as:

$$u|_{(r=r_i)} = 0 \tag{2.4a}$$

$$q_r|_{(r=r_i)} = 0 \tag{2.4b}$$

The equation for in-planar motion (eq. 2.3) with the prescribed boundary conditions (eq. 2.4) can be solved for analytically. The closed form solution for the radial displacement u is given as follows:

$$u(r) = c_1 r + \frac{c_2}{r} - \frac{\rho h \Omega^2}{8D^\circ} r^3 \tag{2.5}$$

where

$$c_1 = \frac{\rho h \Omega^2}{8D^\circ} \left(\frac{r_o^4(3+\nu) + r_i^4(1-\nu)}{r_o^2(1+\nu) - r_i^2(1-\nu)} \right) \tag{2.6a}$$

$$c_2 = -\frac{\rho h \Omega^2}{8D^\circ} r_o^2 r_i^2 \left(\frac{r_o^2(3+\nu) - r_i^2(1+\nu)}{r_o^2(1+\nu) - r_i^2(1-\nu)} \right) \tag{2.6b}$$

The internal forces (q_r and q_θ) can be computed by substituting the expression for u (eq. 2.5) in eq. 2.2.

The governing equation for the transverse displacement w of the spinning disk is given as follows:

$$\rho h \left(\frac{\partial^2 w}{\partial t^2} + 2\Omega \frac{\partial^2 w}{\partial t \partial \theta} + \Omega^2 \frac{\partial^2 w}{\partial \theta^2} \right) + D\nabla^4 w - \frac{\partial}{r\partial r} \left(r q_r \frac{\partial w}{\partial r} \right) - \frac{\partial}{r\partial \theta} \left(q_\theta \frac{\partial w}{r \partial \theta} \right) = p(r, \theta, t) \tag{2.7}$$

where $D = Eh^3/(12(1-\nu^2))$ is the flexural rigidity of the disk and $p(r, \theta, t)$ is the applied external pressure as a function of time t. The boundary conditions for transverse problem corresponding to fixed ($r = r_i$) and free ($r = r_o$) edges are given as follows:

$$w|_{r=r_i} = 0 \tag{2.8a}$$

$$\left. \frac{\partial w}{\partial r} \right|_{r=r_i} = 0 \tag{2.8b}$$

$$\left. \int_{-\frac{h}{2}}^{\frac{h}{2}} \sigma_{zz} \mathrm{d}z \right|_{r=r_0} = 0 \tag{2.8c}$$

$$V_r = -D \left[\frac{\partial \nabla^2 2}{\partial r} + \frac{1-\nu}{r^2} \frac{\partial^2}{\partial \theta^2} \left(\frac{\partial w}{\partial r} - \frac{w}{r} \right) \right] \Bigg|_{r=r_0} = 0 \tag{2.8d}$$

where σ_{zz} and V_r are the edge normal traction and edge vertical shear resultant respectively.

2.2 Finite Element Formulation

In the past, many researchers [Eversman 1968; Eversman and Dodson 1969; Advani and Bulkeley 1969] have used an analytical approach to study the transverse vibration problem

of a spinning disk. However, in order to get a closed form solution, they had to limit their analysis to special cases such as axi-symmetric excitation. Later, researchers [Iwan and Stahl 1973; Benson and Bogy 1978] extended the analytical approach to study the dynamics of a spinning disk under a transverse load. But still for a general case, it is not always possible to find a closed form solution. Hence in order to solve the current problem, we employ a numerical method to get an approximate solution. The Finite element method (FEM) is one such numerical technique, which has been widely popular for solving complex structural mechanics problems.

In order to solve the partial differential equation (PDE) using FEM, first it is required to develop its weak form. Eq. 2.7 is a fourth order differential equation, hence we choose the test function $\tilde{w}(r,\theta)$ as follows:

$$\tilde{w} \in V_w = \left\{ \tilde{w} \,\middle|\, \tilde{w} \in H^2,\ \tilde{w}\big|_{r=r_i} = \left.\frac{\partial \tilde{w}}{\partial r}\right|_{r=r_i} = 0 \right\} \tag{2.9}$$

Multiplying both side of eq. 2.7 and integrating it over the disk area R we get:

$$\int_R \tilde{w}\left[\rho h\left(\frac{\partial^2 w}{\partial t^2} + 2\Omega\frac{\partial^2 w}{\partial t\partial\theta} + \Omega^2\frac{\partial^2 w}{\partial\theta^2}\right) + D\nabla^4 w - \frac{\partial}{r\partial r}\left(r q_r \frac{\partial w}{\partial r}\right) - \frac{\partial}{r\partial\theta}\left(q_\theta \frac{\partial w}{r\partial\theta}\right) - p\right] \mathrm{d}A = 0 \tag{2.10}$$

Simplifying eq. 2.10 we get the weak form as follows:

$$\rho h \int_R \tilde{w}\ddot{w}\mathrm{d}A + 2\rho h\rho h \int_R \tilde{w}\frac{\partial \dot{w}}{\partial\theta}\mathrm{d}A - \rho h\Omega^2 \int_R \frac{\partial \tilde{w}}{\partial\theta}\mathrm{d}A + \int_R \tilde{\boldsymbol{\epsilon}}_b^L\, \mathbf{D}_b\, \boldsymbol{\epsilon}_b^L \mathrm{d}A + \int_R \tilde{\boldsymbol{\Theta}}^T \mathbf{Q}\, \boldsymbol{\Theta}\mathrm{d}A = \int_R \tilde{w} p\, \mathrm{d}A \tag{2.11}$$

where

$$\mathbf{D}_b = \frac{Eh^3}{12(1-\nu^2)}\begin{bmatrix} 1 & \nu & 0 \\ \nu & 1 & 0 \\ 0 & 0 & (1-\nu)/2 \end{bmatrix},$$

$$\dot{w} = \frac{\partial w}{\partial t} \quad , \quad \ddot{w} = \frac{\partial^2 w}{\partial t^2} \quad ,$$

$$\boldsymbol{\epsilon}_b^L = \begin{Bmatrix} -\frac{\partial^2 w}{\partial r^2} \\ -\left(\frac{\partial w}{r\partial r} + \frac{\partial^2 w}{r^2\partial\theta^2}\right) \\ -2\left(\frac{\partial^2 w}{r\partial r\partial\theta} - \frac{\partial w}{r^2\partial\theta}\right) \end{Bmatrix} \quad , \quad \boldsymbol{\Theta} = \begin{Bmatrix} \frac{\partial w}{\partial r} \\ \frac{\partial w}{r\partial r} \end{Bmatrix} \quad \text{and} \quad \mathbf{Q} = \begin{bmatrix} q_r & 0 \\ 0 & q_\theta \end{bmatrix}.$$

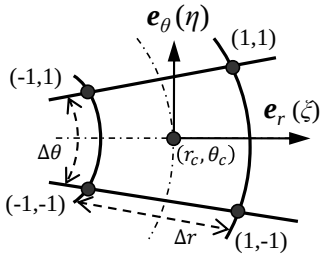

Figure 2.2: A annular sector element

A special annular sector element (Fig. 2.2) is used for spacial discretization of the disk, as shown in Fig. 2.3. These are conforming elements that have merit over the conventional triangular or quadrilateral elements, as they do not introduce any geometric error during discretization. Each element contains 4 nodes and every node has 4 degree of freedoms (DOF), which are the disk's transverse displacement (w), its radial slope ($\partial w/\partial r$), its circumferential slope ($\partial w/\partial\theta$) and its curvature ($\partial^2 w/\partial r\partial\theta$).

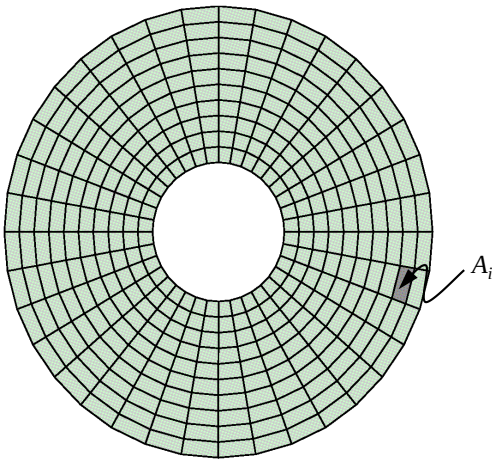

Figure 2.3: A FEM mesh for disk

The weak form (2.11) can be re-written as the summation of the integrals on the disk elements as follows:

$$\sum_{i=1}^{N_e}\Bigg[\rho h\int_{A_i}\tilde{w}\ddot{w}\mathrm{d}A+2\rho h\rho h\int_{A_i}\tilde{w}\frac{\partial\dot{w}}{\partial\theta}\mathrm{d}A-\rho h\Omega^2\int_{A_i}\frac{\partial\tilde{w}}{\partial\theta}\mathrm{d}A \\ +\int_{A_i}\tilde{\boldsymbol{\epsilon}}_b^L\,\mathbf{D}_b\,\boldsymbol{\epsilon}_b^L\mathrm{d}A+\int_{A_i}\tilde{\boldsymbol{\Theta}}^T\mathbf{Q}\,\boldsymbol{\Theta}\mathrm{d}A-\int_{A_i}\tilde{w}p\,\mathrm{d}A\Bigg]=0 \qquad \forall\tilde{w}\in V_w \quad (2.12)$$

where the disk area R is the union of element areas A_i. The polar coordinates (r, θ) of the annular elements are parameterized as follows:

$$r(\xi) = r_c + \frac{\Delta r}{2}\xi \tag{2.13a}$$

$$\theta(\eta) = \theta_c + \frac{\Delta \theta}{2}\eta \tag{2.13b}$$

Using the parametrization (eq. 2.13), the field variable w can be approximated in terms of nodal DOFs as follows:

$$w(r,\theta) = w(\xi,\eta) = [N(\xi,\eta)]_{1\times 16} \left\{ (w)_1, \left(\frac{\partial w}{\partial r}\right)_1, \left(\frac{\partial w}{\partial \theta}\right)_1, \left(\frac{\partial^2 w}{\partial r \partial \theta}\right)_1, \cdots \left(\frac{\partial^2 w}{\partial r \partial \theta}\right)_4 \right\}_{16\times 1} \tag{2.14}$$

where the components of $\mathbf{N}(\xi, \eta)$ are called the shape functions.

Using the above approximation (eq. 2.14), the weak form for the PDE can be reduced to the following set of standard of finite element equations:

$$[M]\{\ddot{w}\} + [G_{gyro}]\{\dot{w}\} + [K]\{w\} = \{f\} \tag{2.15}$$

where M, G_{gyro} and K are the disk's inertia, gyroscopic and stiffness matrices respectively. $\{w\}$ is the unknown DOF vector and $\{f\}$ is the applied external load on the disk. The disk's system matrices are evaluated by assembling the corresponding element matrices, which are defined as follows:

$$[M^e] = \rho h \iint_{A^e} [N(\xi,\eta)]^T [N(\xi,\eta)]\, J(\xi,\eta)\, \mathrm{d}\xi \mathrm{d}\eta \tag{2.16a}$$

$$[G^e] = 2\rho h \iint_{A^e} [N(\xi,\eta)]^T \left[\frac{\partial N(\xi,\eta)}{\partial \eta}\right] \left(\frac{2}{\Delta\theta}\right) J(\xi,\eta)\, \mathrm{d}\xi \mathrm{d}\eta \tag{2.16b}$$

$$\begin{aligned} [K^e] &= -\rho h \Omega^2 \iint_{A^e} \left[\frac{\partial N(\xi,\eta)}{\partial \eta}\right]^T \left[\frac{\partial N(\xi,\eta)}{\partial \eta}\right] \left(\frac{4}{\Delta\theta^2}\right) J(\xi,\eta)\, \mathrm{d}\xi \mathrm{d}\eta \\ &+ \iint_{A^e} [B(\xi,\eta)]^T [D] [B(\xi,\eta)]\, J(\xi,\eta)\, \mathrm{d}\xi \mathrm{d}\eta \\ &+ \iint_{A^e} [F(\xi,\eta)]^T [Q] [F(\xi,\eta)]\, J(\xi,\eta)\, \mathrm{d}\xi \mathrm{d}\eta \end{aligned} \tag{2.16c}$$

where

$$[F(\xi,\eta)] = \begin{bmatrix} \left(\frac{2}{\Delta r}\right)\left[\frac{\partial N((\xi,\eta))}{\partial \xi}\right] \\ \left(\frac{2}{\Delta\theta}\right)\left(\frac{1}{r(\xi)}\right)\left[\frac{\partial N((\xi,\eta))}{\partial \eta}\right] \end{bmatrix} \quad \text{and}$$

$$[B(\xi,\eta)] = \begin{bmatrix} \left(\frac{4}{\Delta r^2}\right)\left[\frac{\partial^2 N(\xi,\eta)}{\partial \xi^2}\right] \\ -\left[\left(\frac{2}{\Delta r}\right)\left(\frac{1}{r(\xi)}\right)\left[\frac{\partial N(\xi,\eta)}{\partial \xi}\right] + \left(\frac{4}{\Delta\theta^2}\right)\left(\frac{1}{r^2(\xi)}\right)\left[\frac{\partial^2 N(\xi,\eta)}{\partial \eta^2}\right]\right] \\ -2\left[\left(\frac{4}{\Delta r \Delta\theta}\right)\left(\frac{1}{r(\xi)}\right)\left[\frac{\partial^2 N(\xi,\eta)}{\partial \xi \partial \eta}\right] - \left(\frac{2}{\Delta\theta}\right)\left(\frac{1}{r^2(\xi)}\right)\left[\frac{\partial N(\xi,\eta)}{\partial \xi}\right]\right] \end{bmatrix}.$$

Proportional damping is used to model the intrinsic damping present in the disk. In this method, the system damping matrix C_{prop} is expressed as a linear combination of the system inertia and stiffness matrices as follows:

$$[C_{prop}] = \alpha\,[M] + \beta\,[K] \tag{2.17}$$

where α and β are called the damping coefficients. Introducing C_{prop} in eq. 2.15, we get the following set of finite element equations for the disk's transverse motion:

$$[M]\,\{\ddot{w}\} + [G]\,\{\dot{w}\} + [K]\,\{w\} = \{f\} \tag{2.18}$$

where $[G] = [G_{gyro}] + [C_{prop}]$.

The natural boundary conditions for the traction-free outer edge are accounted for during the weak form formulation. The kinematic displacement boundary conditions prescribed at the clamped inner edge ($\forall$ nodes at $r = r_i$) are as follows:

$$(w)_i = 0\ , \qquad \left(\frac{\partial w}{\partial r}\right)_i = 0\ , \qquad \left(\frac{\partial w}{\partial \theta}\right)_i = 0 \quad \text{and} \quad \left(\frac{\partial^2 w}{\partial r \partial \theta}\right)_i = 0. \tag{2.19}$$

2.3 Load-Unload Ramp Modeling

Some years ago, when the HDD was non-operational, the slider rested on a laser textured zone present near the inner diameter of the disk. This is known as contact start stop (CSS) technology. This method can cause serious wear problems if it were to be used for mobile drives. To overcome this drawback, most of the commercial mobile drives use load-unload (L/UL) technology [Hitachi 2007c]. In this method, when the HDD power is turned off, the slider is lifted off the disk and parked on fixed ramp near the outer edge of the disk (Fig. 2.4). However, the proximity of the ramp to the spinning disk increases the possibility of a collision between the disk and the ramp during an operational shock. Hence it is important to model the interaction between the parking ramp and the spinning disk to understand its effect on the HDI stability during the shock.

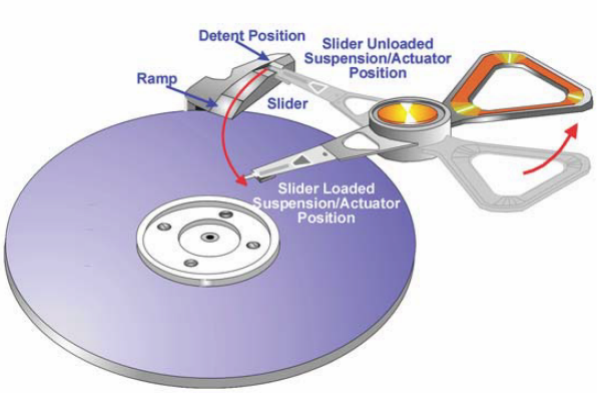

Figure 2.4: The load/unload technology [Hitachi]

In order to save computational cost, we model the LUL ramp as a rigid body as shown in Fig. 2.5. Two L/UL ramps are placed symmetrically on the two sides of the disk at equidistance. The constraint imposed by the ramp on the spinning disk can be expressed as follows:

$$|w(r_{ramp}, \theta_{ramp})| \leq w_{ramp} \tag{2.20}$$

where w_{ramp} is the minimum clearance between the disk and ramp. The governing equation for the disk transverse motion has been derived for the rotatory frame and hence the coordinates for the ramp location $(r_{ramp}, \theta_{ramp})$ changes its position on the FE grid with time. Since the disk is fixed at its ID, it is only the angular coordinates of the ramp that changes as follows:

$$\theta_{ramp}(t) = \theta^0_{ramp} - \Omega t \tag{2.21}$$

where θ^0_{ramp} is the initial angular coordinate for the ramp.

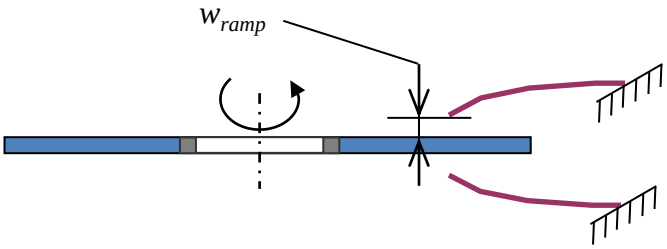

Figure 2.5: A rigid body model for L/UL ramp

A Lagrange multiplier method is used to implement the constraints on the disk model.

This method requires that the boundary conditions (eq. 2.19) and the ramp constraint (eq. 2.20) be expressed together in the following matrix form:

$$[C]\{w\} = \{w_c\} \tag{2.22}$$

where $[C]$ is called the constraint matrix. The reaction force $\{\lambda\}$ arising due to the constraint (eq. 2.22) is added to the FEM equations as follows:

$$[M]\{\ddot{w}\} + [G]\{\dot{w}\} + [K]\{w\} + [C]^T\{\lambda\} = \{f\} \tag{2.23}$$

2.4 Transient Solution

It is a common practice to use a finite difference method (FDM) to solve the ordinary differential equation resulting from time dependent problem in FEM. Newmark-Beta [Katona and Zienkiewicz 1985] is one such popular FDM scheme used extensively in structural mechanics problems. In this section, we show the implementation of the Newmark-Beta scheme to solve the current problem.

Discretizing the time into uniform time steps of Δt, we obtain the equation of motion with BCs at time $t = t_{n+1}$ is given as follows:

$$[M]\{\ddot{w}\}_{n+1} + [G]\{\dot{w}\}_{n+1} + [K]\{w\}_{n+1} + [C]^T_{n+1}\{\lambda\}_n + 1 = \{f\}_{n+1} \tag{2.24a}$$

$$[C]_{n+1}\{w\}_{n+1} = \{w_c\}_{n+1} \tag{2.24b}$$

where $t_n = n\Delta t$.

In the Newmark Beta scheme, the velocity and the displacement vectors at time t_{n+1} are expressed in terms of the acceleration vector as follows:

$$\{\dot{w}\}_{n+1} = \{\dot{\breve{w}}\}_{n+1} + \beta_1 \Delta t \{\ddot{w}\}_{n+1} \tag{2.25a}$$

$$\{w\}_{n+1} = \{\breve{w}\}_{n+1} + \beta_2 \frac{\Delta t^2}{2}\{\ddot{w}\}_{n+1} \tag{2.25b}$$

where $\{\breve{w}\}_{n+1}$ and $\{\dot{\breve{w}}\}_{n+1}$ are, respectively, the projected displacement and the velocity vectors at $t = t_{n+1}$. They are evaluated using the dynamic variables at $t = t_n$ as follows:

$$\{\dot{\breve{w}}\}_{n+1} = \{\dot{w}\}_n + (1 - \beta_1)\Delta t\{\ddot{w}\}_n \tag{2.26a}$$

$$\{\breve{w}\}_{n+1} = \{w\}_n + \Delta t\{\dot{w}\}_n + (1 - \beta_2)\frac{\Delta t^2}{2}\{\ddot{w}\}_n \tag{2.26b}$$

Table 2.1: The disk parameters for model verification studies

Inner Radius	53.35 mm
Outer Radius	178.00 mm
Thickness	0.78 mm
Young's Modulus	210×10^9 GPa
Poisson's Ration	0.3
Density	7800 Kg/m^3

Substituting the value for $\{\dot{w}\}_{n+1}$ and $\{w\}_{n+1}$ from eq. 2.25 into eq. 2.24 and rearranging it, we get following set of algebraic equations:

$$\begin{bmatrix} [A] & [C]_{n+1}^T \\ [C]_{n+1} & [0] \end{bmatrix} \begin{Bmatrix} \{\ddot{w}\}_{n+1} \\ \{\lambda\}_{n+1} \end{Bmatrix} = \begin{Bmatrix} \{X\}_{n+1} \\ \{Y\}_{n+1} \end{Bmatrix} \tag{2.27}$$

where

$$[A] = [M] + \beta_1 \Delta t + [G] + \frac{\beta_2}{2} \Delta t^2 [K] \tag{2.28a}$$

$$\{X\}_{n+1} = \{f\}_{n+1} - [G] \{\breve{\dot{w}}\}_{n+1} - [K] \{\breve{w}\}_{n+1} \tag{2.28b}$$

$$\{Y\}_{n+1} = \left(\frac{2}{\Delta t^2 \beta_2} \right) \left(\{w_c\} - [C]_{n+1} \{\breve{w}\}_{n+1} \right) \tag{2.28c}$$

Eq. 2.27 is solved for the unknown acceleration $\{\ddot{w}\}_{n+1}$ and reaction forces $\{\lambda\}_{n+1}$. Furthermore, the disk displacement and velocity at t_n can be evaluated using eq. 2.25.

2.5 Modal Validation

In order to assure the accuracy of the results, we benchmarked the current disk model against the previously published studies. Two test studies are conducted to validate the finite element disk model. In the first study, the natural frequencies of the disk in its stationary state are evaluated and compared with the other available numerical solutions. In the second study, the current model is used to exhibit the well-known *mode splitting* phenomenon found in spinning disks. The disk geometry and its material properties used for the benchmark studies are listed in Table 2.1.

2.5.1 Modal Analysis

In order to evaluate the natural frequencies (ω_{mn}) of a spinning disk and its respective mode shapes $\{w_{mn}\}$, it is required to solve the following generalized eigenvalue problem:

$$\omega_{mn}^2 [M] \{w_{mn}\} + [K] \{w_{mn}\} = 0 \tag{2.29}$$

where $[M]$ and $[K]$ have been defined in eq. 2.16a and eq. 2.16c, respectively.

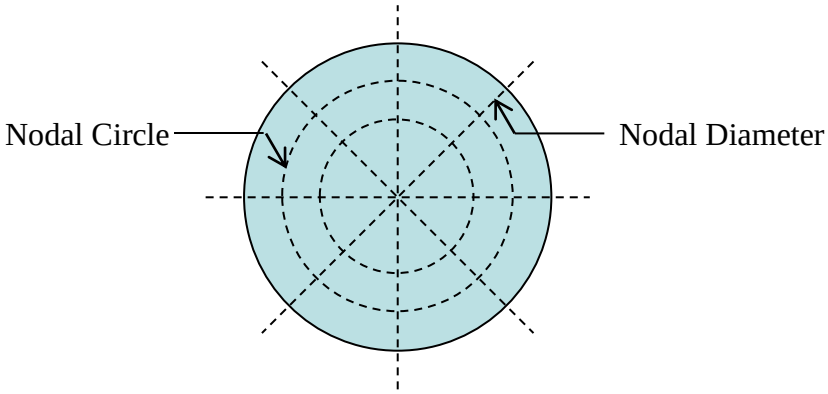

Figure 2.6: A schematic diagram for explaining disk mode shapes

The basic mode shapes of a spinning disk can be explained with the help of Fig. 2.6. The dotted lines shown in the figure are called the nodal lines. During the vibration, the disk displacement at these lines remains zero. A general mode shape can consist of m modal circles and n modal diameters, and it is referred as mode (m, n). When the disk is excited in a$(m, 0)$ mode, its response is axisymmetric i.e. $\partial w/\partial\theta = 0$. These modes are excited when the disk is subject to a symmetric load. For the disk used in current study, the first few basic mode shapes are shown in Fig. 2.7.

To show the validity of the current finite element disk model, we compared the results from the modal analysis with a commercial FEM package ANSYS as well as another FDM based numerical scheme [Kirpekar 2006]. A uniform annular mesh for the disk (containing 10 radial and 24 circumferential elements) was used in all the numerical techniques being compared. The error in prediction of the natural frequency was computed using the analytical solution provided by D'Angelo. The summary of results is shown in Table 2.2. It can be observed that the current method consistently gives the least error while predicting the natural frequency of the stationary disk.

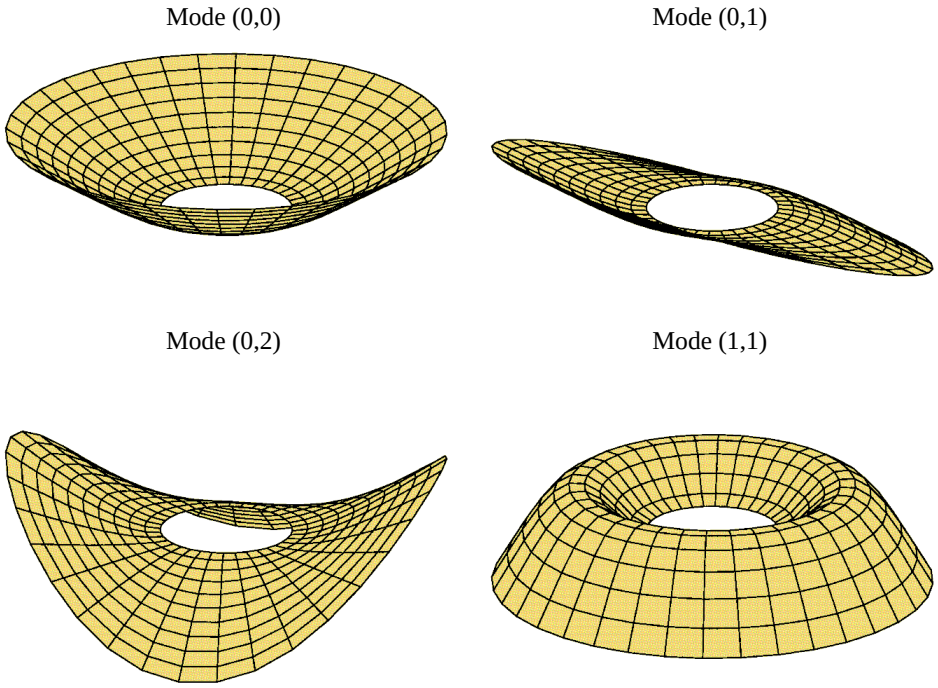

Figure 2.7: Mode shapes of a stationary disk

Table 2.2: Comparison of disk natural frequencies

Mode	Analytical	ANSYS		Spectral FDM		Current FEM	
	Frequency	Frequency	Error	Frequency	Error	Frequency	Error
$(0,0)$	39.73 Hz	41.21 Hz	3.72%	40.00 Hz	0.68%	40.68 Hz	2.40%
$(0,1)$	39.08 Hz	40.61 Hz	3.93%	36.00 Hz	-7.88%	40.02 Hz	2.40%
$(0,2)$	47.76 Hz	49.18 Hz	2.97%	46.00 Hz	-3.69%	48.61 Hz	1.77%
$(0,3)$	79.18 Hz	81.89 Hz	3.43%	77.00 Hz	-2.75%	81.16 Hz	2.50%
$(0,4)$	131.64 Hz	136.88 Hz	3.98%	124.00 Hz	-5.80%	135.04 Hz	2.58%

2.5.2 Mode Splitting

There have been many analytical and experimental investigations [Mote 1970; Moeller and Iwan 1976] in the past to study the effect of disk rotation on its natural frequencies. Its well known that during an axi-symmetric excitation of the disk, the rotation speed does not have much effect on the frquencies of axi-symmetric modes $(m, 0)$. However, when the disk is excited in one of its asymmetric $(0, n)$ modes, due to the spinning action of the disk, these modes split into a forward and a backward traveling wave. This phenomenon is called mode splitting, and it can be explained based on the classical theory [Southwell 1922]. The frequency of a general mode w_{mn} for an angular velocity Ω is given by:

$$\omega_{mn}(\Omega) = \omega^{\circ}_{mn} \pm n\Omega \tag{2.30}$$

where ω°_{mn} is the natural frequency of the stationary disk.

In order to reproduce the phenomenon of mode splitting, we conducted a dynamic simulation in which a mode shape w_{mn} was used as an initial displacement for the spinning disk. The frequencies of the traveling waves were determined using the fast Fourier transform (FFT) of the disk displacement at point $(r_{Ref}, \theta_{Ref}(t))$ fixed in a stationary frame. The coordinates for the point of observations can be located on the disk mesh using the similar formulation (eq. 2.21) as that developed for locating the L/UL ramp. The FFT spectrum for the first few disk modes are shown in Fig. 2.8.

It can be observed that for the axi-symmetric $(0, 0)$ mode, there is only a slight increase in the natural frequency ω_{00} with an increase in disk RPM. However, for all the asymmetric modes ($(0, 1)$, $(0, 2)$ and $(1, 1)$) shown in Fig. 2.8, the natural frequencies clearly splits into forward traveling (increasing) and backward traveling modes as expected. Hence the current numerical model is satisfactorily able to show the mode splitting phenomenon.

2.6 Closure

A finite element based numerical model for a spinning disk was introduced in this chapter. This model has capability of simulating the disk dynamics for any generalized transverse excitation $(p(r, \theta, t))$. It can also predict the disk behavior during its collision with stationary parking ramp. Even though, the finite element formulation presented in this chapter was developed for a disk clamped at its ID, it can be readily extended to the case where the disk has a flexible mounting $(w(r_i, \theta) \neq 0)$. A modal analysis was presented at the end of

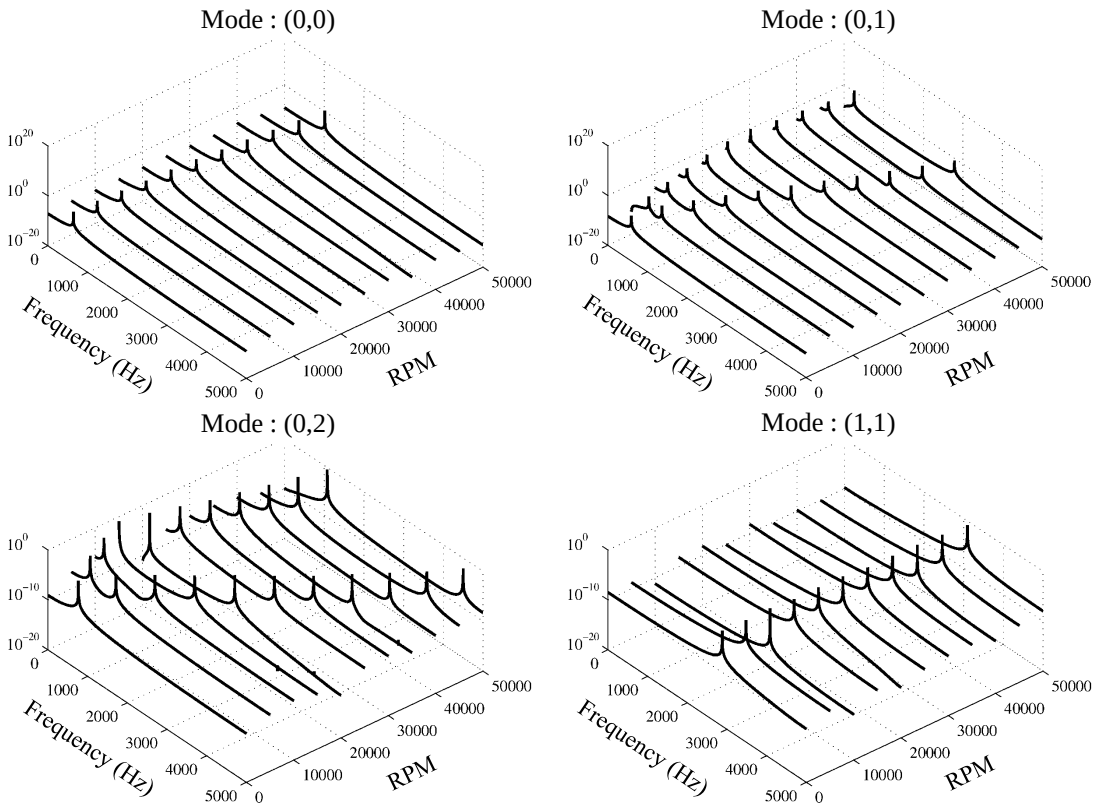

Figure 2.8: Mode splitting in a spinning disk

this chapter to show the better accuracy of the current FE based disk model over other alternative numerical techniques.

Chapter 3

Disk support system

In the previous chapter, we have presented a model for the spinning disk that is mounted on a rigid base. However, in an actual HDD, the disk is clamped onto a hub of a spindle motor that is mounted on a base plate. The rotor dynamics of the spindle motor and the flexibility of the base plate can affect the disk response to an external disturbance. In this chapter we extend the spinning disk model to include the effect of the flexible disk-support system present in a mobile HDD. The following sections give the details about the design and the modeling of a disk support assembly used in the current study. A section is included at the end of this chapter describing the numerical techniques used to reduce the computational effort required for the dynamic analysis.

3.1 Spindle Motor

A spindle motor is an integral part of every hard disk drive. It rotates the stack of magnetic disk mounted on a hub. The construction of a typical spindle motor used in a commercial mobile HDD is shown in Fig. 3.1. The structural components of a spindle motor can be broadly categorized into a rotating hub and a stationary housing. The particular design shown in Fig. 3.1 has its shaft attached to the rotating hub constituting the rotor unit of the motor. A permanent NdFeB magnet is attached to the hub, which is actuated by the set of electromagnetic coils present outside the shaft's sleeve. Conventionally ball bearings (BB) were used in a spindle motor to reduce the friction between the rotating shaft and its sleeve. However, the imperfections in the rolling ball can cause serious vibration problems during the operation. Furthermore, in ball bearings, shock loads are absorbed

by point contact between the rolling element and the mating surfaces. This concentrated force can lead to permanent deformation of the surface. All this contributes to high non-repeatable run-out (NRRO) error which degrades the tracking capabilities of an actuator following a particular track. Hence in order to minimize the NRRO error for high track density products, the hard disk industry has gradually moved to the fluid dynamic bearing (FDB) based spindle motors [Source: Hitachi]. A thin film of lubricant spreads out evenly between the rotating and stationary surface and allows a vibration free operation. The fluid provides the additional mechanical damping, which improves the shock performance of the system. The reduced NRRO error, lower acoustic noise and high reliability have made FDB a standard choice for hard disk spindle motors. A good comparison study between the ball bearings and fluid dynamic bearings can be found in Ku 1996.

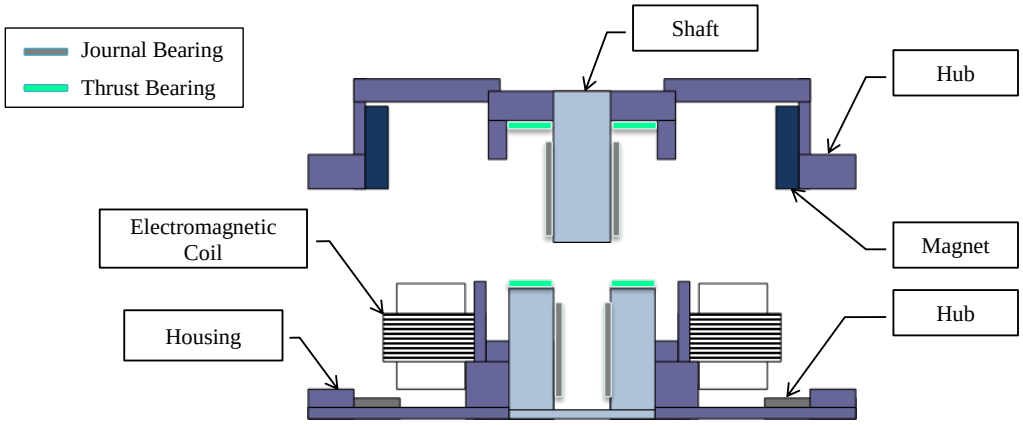

Figure 3.1: A schematic diagram of a spindle motor used in a mobile HDD

Several researchers have investigated the problem of spindle motor dynamics. In 1997, Shen et. al. [Shen and Ku 1997] presented a non-classical theory for modeling the disk-spindle system which, consists of multiple elastic disks mounted on a rigid spindle. They evaluated the natural frequencies and modal shapes for the assembly undergoing infinitesimal rigid body motion. In a follow-up study [Shen and Ku 1997], they computed a closed form solution for the forced response of the disk-spindle system. Park et al. improved their model by including the effect of hydrodynamic bearings (FDB). They used a spring-dashpot system to represent the FDB. However, in their model, the value of the dynamics coefficients for the equivalent model was not evaluated for their specific design. Later, they extended their model from the rigid spindle to a flexible rotor/housing using the component mode synthesis

(CMS) method [Shen 2003; Shen et al. 2004]. In a different approach, Jang et. al. focused their efforts on understanding the effect of the bearing design on the performance of the FDB in a spindle motor [Jang and Yoon 2002a,b]. They developed a detailed model for the FDB which contains details such as groove design, its location, cavitation etc. They used lubrication theory to solve the fluid dynamics problem for the hydrodynamic bearing. The finite element substructuring technique [Jang et al. 2005] was used for the modeling of the structural components present in a spindle motor. Their method was highly accurate, but solving the Reynolds lubrication equation made the process computationally expensive. In order to save on simulation time, they proposed an alternative approach [Jang and Lee 2006] to model the FDB behavior using an equivalent spring-damper system. They presented a perturbation method to evaluate the dynamic coefficients (stiffness and damping) for a given spindle motor design.

All of the models presented above were focused on the disk-spindle motor assembly response. In the current study, the system under consideration contains more HDD components. As indicated, using these detailed motor models can make the simulator computationally expensive and practically unusable. Hence it is required to develop a model that is computationally efficient yet accurate. In the following sections we describe the spindle motor model developed for the current study.

3.1.1 Structural modeling

The finite element method was used to model the response of the structural units present in a spindle motor. A full 3D finite element model (Fig. 3.2) of the rotor assembly and the stationary housing was developed using a commercial package (ANSYS). Due to the high number of DOFs ($\sim$ 100000) present in the complete system, the finite element reduction technique [Guyan 1965] was used to reduce the computational efforts. In this method, the number of DOFs present in a system is reduced while retaining the low frequency response of the system. In the reduction process, the retained DOFs are called *master* DOFs. In the current model, the reduction process was carried out in two steps. In the first step, a commercial software ANSYS was used to reduce the full system inertia M^{full} and stiffness K^{full} matrices to the reduced matrices (M^{red}_{ANSYS} and K^{red}_{ANSYS}) with 1000 DOFs. Later, the number of DOFs of the system was further reduced using an iterative reduction scheme (IRS)[Friswell et al. 1995]. This iterative technique provides a better accuracy in retaining the system's lowest natural frequencies by removing one DOF at a time, which in turns

makes the process computationally expensive. Hence this method is used on the reduced system that already has a comparatively small number of DOFs. The *master* DOFs in this process were selected based on the criterion proposed by Shah and Raymund. However, the nodes present at the FDB locations on the rotor and housing surface are always retained even if it violates the Shah and Raymund criterion. These nodes are required for evaluating the FDB response. The equations of motion for the reduced system are:

$$[M^{hub}]\{\ddot{u}^{hub}\} + [C^{hub}]\{\dot{u}^{hub}\} + [K^{hub}]\{u^{hub}\} = \{f^{hub}\} \tag{3.1a}$$

$$[M^{hsng}]\{\ddot{u}^{hsng}\} + [C^{hsng}]\{\dot{u}^{hsng}\} + [K^{hsng}]\{u^{hsng}\} = \{f^{hsng}\} \tag{3.1b}$$

where $\{u^{hub}\}$ and $\{u^{hsng}\}$ are the displacements of the retained *master* DOFs for rotating hub and stationary housing respectively. Rayleigh proportional damping [Meirovitch 1996] was used to model the damping behavior of the reduced system.

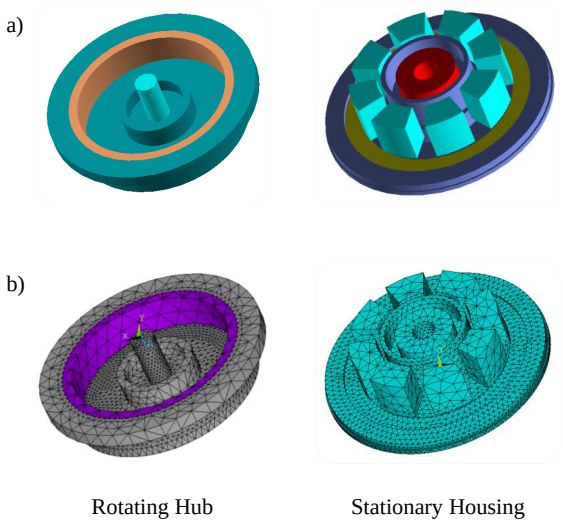

Figure 3.2: Modeling of a spindle motor structural components a) 3-D Design b) FE Mesh

3.1.2 Fluid dynamic bearings

The primary function of a bearing in a spindle motor is to reduce the friction between the rotating and stationary parts. The bearings present in a spindle motor can be broadly categorized into journal and thrust bearings. They are differentiated based on their load carrying capacities (Fig. 3.1). The journal bearing is formed between the rotating shaft and

its sleeve and carries the radial load between them, whereas the thrust bearing is formed between the hub and the top of the sleeve to support the axial load. The shaft surface has two separate sets of herringbone groves (pump-up and pump down) to help the lubricant flow between the mating surfaces (Fig. 3.3a). A groove-less area separates them, divides the journal bearing into its top and bottom journal bearings. Similarly, spiral grooves are present on the hub surface to aid the lubricant flow in the thrust bearing (Fig. 3.3b).

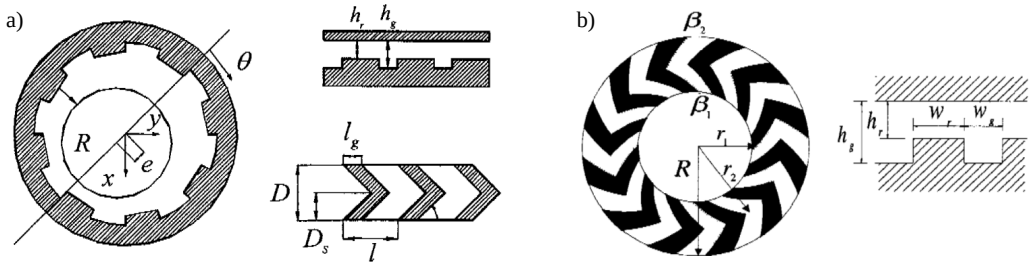

Figure 3.3: Schematic of a) Herringbone groove journal bearing b) Spiral groove thrust bearing with rectangular grooves in spindle motor [Oh and Rhim 2001]

The flow of the thin layer of lubricant in the bearing is governed by the Reynolds equation. It is derived from the Navier-Stokes equation assuming that the pressure variation over the thin lubricant layer is negligible. Eq. 3.2a and eq. 3.2b are the Reynolds equation for a journal and a thrust bearing in cylindrical coordinates (r, θ, z), respectively.

$$\frac{\partial}{R\partial\theta}\left(\frac{h^3}{12\mu}\frac{\partial p}{R\partial\theta}\right)+\frac{\partial}{\partial z}\left(\frac{h^3}{12\mu}\frac{\partial p}{R\partial z}\right)=\frac{R\Omega}{2}\frac{\partial h}{\partial\theta}+\frac{\partial h}{\partial t} \tag{3.2a}$$

$$\frac{\partial}{r\partial r}\left(r\frac{h^3}{12\mu}\frac{\partial p}{\partial r}\right)+\frac{\partial}{r\partial\theta}\left(\frac{h^3}{12\mu}\frac{\partial p}{r\partial\theta}\right)=\frac{r\Omega}{2}\frac{\partial h}{r\partial\theta}+\frac{\partial h}{\partial t} \tag{3.2b}$$

where p, h, μ, R and Ω are the pressure, film thickness, coefficient of viscosity, radius of shaft and motor angular speed, respectively.

The above eq. 3.2 is required to be solved numerically for the pressure distribution $p(r, \theta, z, t)$ in a given configuration $h(r, \theta, z)$. Since eq. 3.2 is non-linear, it has to be solved iteratively with the structural dynamics (rotor and housing) equations to get the complete system response at a given time. This iterative method results in higher computational time. In order to reduce the effort, we follow the approach suggested by Jang and Lee. The hydrodynamic bearings are represented by a set of equivalent spring-dashpot systems as shown in Fig. 3.4. The damping and stiffness coefficients for a spring-dashpot system are evaluated by solving the perturbed Reynolds equations. The perturbation equations can be derived from

the Reynolds equation by substituting the first-order expansion of film thickness h (eq. 3.3a), its derivative $\partial h/\partial t$ (eq. 3.3b) and pressure p (eq. 3.3c) with respect to small displacements and velocities into the eq. 3.2.

$$h = h_0 + \sum_{i=1}^{3} \frac{\partial h}{\partial \xi_i} \Delta\xi_i \qquad (\xi_i = x, y, z) \tag{3.3a}$$

$$\frac{\partial h}{\partial t} = \frac{\partial h_0}{\partial t} + \sum_{i=1}^{3} \frac{\partial h}{\partial \xi_i} \Delta\dot{\xi}_i + \sum_{i=1}^{3} \frac{\partial}{\partial t}\left(\frac{\partial h}{\partial \xi_i}\right) \Delta\xi_i \tag{3.3b}$$

$$p = p_0 + \sum_{i=1}^{3} \frac{\partial p}{\partial \xi_i} \Delta\xi_i + \sum_{i=1}^{3} \frac{\partial p}{\partial \dot{\xi}_i} \Delta\dot{\xi}_i \tag{3.3c}$$

where h_0 and p_0 are the quasi-static film thickness and pressure, respectively. Substituting eq. 3.3 in eq. 3.2, we get the following perturbed form of the Reynolds equation:

$$\frac{\partial}{R\partial\theta}\left(\frac{h^3}{12\mu}\frac{\partial p_\xi}{R\partial\theta}\right) + \frac{\partial}{\partial z}\left(\frac{h^3}{12\mu}\frac{\partial p_\xi}{\partial z}\right) = f_\xi^J \tag{3.4a}$$

$$\frac{\partial}{r\partial r}\left(r\frac{h^3}{12\mu}\frac{\partial p_\xi}{\partial r}\right) + \frac{\partial}{r\partial\theta}\left(\frac{h^3}{12\mu}\frac{\partial p_\xi}{r\partial\theta}\right) = f_\xi^T \tag{3.4b}$$

where the definitions of f_ξ^J and f_ξ^J are as follows:

$$f_\xi^J = \begin{cases} \frac{R\Omega}{2}\frac{\partial h_0^2}{\partial\theta} + \frac{\partial h_0}{\partial t} & : \xi = 0 \\ -\frac{\partial}{R\partial\theta}\left(\frac{h_0}{4\mu}\frac{\partial p_0}{R\partial\theta}\cos\theta\right) - \frac{\partial}{\partial z}\left(\frac{h_0^2}{4\mu}\frac{\partial p_0}{\partial z}\cos\theta\right) + \frac{R\Omega}{2}\frac{\partial\cos\theta}{R\partial\theta} & : \xi = x \\ -\frac{\partial}{R\partial\theta}\left(\frac{h_0^2}{4\mu}\frac{\partial p_0}{R\partial\theta}\sin\theta\right) - \frac{\partial}{\partial z}\left(\frac{h_0^2}{4\mu}\frac{\partial p_0}{\partial z}\sin\theta\right) + \frac{R\Omega}{2}\frac{\partial\sin\theta}{R\partial\theta} & : \xi = y \\ 0 & : \xi = z \\ \cos\theta & : \xi = \dot{x} \\ \sin\theta & : \xi = \dot{y} \\ 0 & : \xi = \dot{z} \end{cases} \tag{3.5}$$

$$f_\xi^T = \begin{cases} \frac{r\Omega}{2}\frac{\partial h_0}{r\partial\theta} + \frac{\partial h_0}{\partial t} & : \xi = 0 \\ 0 & : \xi = x \\ 0 & : \xi = y \\ \frac{\partial}{r\partial r}\left(r\frac{h_0^2}{4\mu}\frac{\partial p_0}{\partial r}\right) + \frac{\partial}{r\partial\theta}\left(\frac{h_0^2}{4\mu}\frac{\partial p_0}{r\partial\theta}\right) & : \xi = z \\ 0 & : \xi = \dot{x} \\ 0 & : \xi = \dot{y} \\ 1 & : \xi = \dot{z} \end{cases} \tag{3.6}$$

In order to get the solution for the perturbed pressure p_ξ, it is first required to solve the standard Reynolds equation (eq. 3.2) for pressure the p_0. The finite element method was used to solve it numerically. Once the perturbed equation is solved, the dynamic coefficients for the FDB can be evaluated by integrating the perturbed pressure over the bearing area as follows:

$$\mathbf{K}^J = \iint_J \begin{Bmatrix} -\cos\theta \\ -\sin\theta \\ 0 \end{Bmatrix} \begin{Bmatrix} p_x & p_y & p_z \end{Bmatrix} \mathrm{d}A = \begin{bmatrix} K^J_{xx} & K^J_{xy} & K^J_{xz} \\ K^J_{yx} & K^J_{yy} & K^J_{yz} \\ 0 & 0 & 0 \end{bmatrix} \tag{3.7a}$$

$$\mathbf{C}^J = \iint_J \begin{Bmatrix} -\cos\theta \\ -\sin\theta \\ 0 \end{Bmatrix} \begin{Bmatrix} p_{\dot{x}} & p_{\dot{y}} & p_{\dot{z}} \end{Bmatrix} \mathrm{d}A = \begin{bmatrix} C^J_{xx} & C^J_{xy} & C^J_{xz} \\ C^J_{yx} & C^J_{yy} & C^J_{yz} \\ 0 & 0 & 0 \end{bmatrix} \tag{3.7b}$$

$$\mathbf{K}^T = \iint_T \begin{Bmatrix} 0 \\ 0 \\ -1 \end{Bmatrix} \begin{Bmatrix} p_x & p_y & p_z \end{Bmatrix} \mathrm{d}A = \begin{bmatrix} 0 & 0 & 0 \\ 0 & 0 & 0 \\ K^T_{zx} & K^T_{zy} & K^T_{zz} \end{bmatrix} \tag{3.7c}$$

$$\mathbf{C}^T = \iint_T \begin{Bmatrix} 0 \\ 0 \\ -1 \end{Bmatrix} \begin{Bmatrix} p_{\dot{x}} & p_{\dot{y}} & p_{\dot{z}} \end{Bmatrix} \mathrm{d}A = \begin{bmatrix} 0 & 0 & 0 \\ 0 & 0 & 0 \\ C^T_{zx} & C^T_{zy} & C^T_{zz} \end{bmatrix} \tag{3.7d}$$

where $\mathbf{K}^J$, $\mathbf{C}^J$, $\mathbf{K}^T$ and $\mathbf{C}^T$ are the stiffness and damping coefficients for journal and thrust bearing, respectively.

In the current model, we need to evaluate three set of stiffness and damping coefficients, one each for a thrust, a top and a bottom journal bearings. Each of these bearings is represented by a set of four spring-dashpot systems located symmetrically along the circumference of the shaft as shown in Fig. 3.4. For simplicity, the spring-dashpot system in the schematic are shown to be one-dimensional. However in the actual model, they are 3-dimensional. The reaction forces on the rotor ($\mathbf{f}^r = (f^r_x, f^r_y, f^r_z)^T$) and the housing ($\mathbf{f}^s = (f^s_x, f^s_y, f^s_z)^T$) units due to deformation of FDB can be written as:

$$\mathbf{f}^r = -\mathbf{f}^s = -\mathbf{K}^{FDB}\left(\mathbf{u}^r - \mathbf{u}^s\right) - \mathbf{C}^{FDB}\left(\dot{\mathbf{u}}^r - \dot{\mathbf{u}}^s\right) \tag{3.8}$$

where $\mathbf{u}^r = (u^r_x, u^r_y, u^r_z)^T$ and $\mathbf{u}^s = (u^s_x, u^s_y, u^s_z)^T$ are the displacement vectors of the rotor and the housing at a particular equivalent FDB location, respectively.

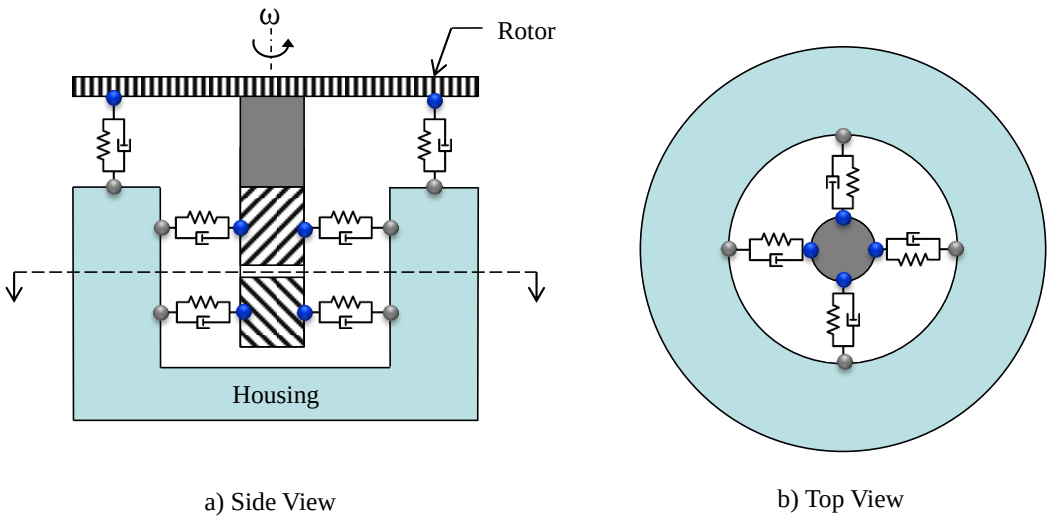

Figure 3.4: An equivalent spring-dashpot representation for FDB

3.2 Base Plate

The spindle motor that carries the stack of magnetic disks is mounted on a aluminum casing known as the *base plate*. The construction of a typical base plate used in a commercial mobile HDD is shown in Fig. 3.5. In addition to the spindle motor, it also supports the voice coil motor and a bracket containing the on-board electronic chips. The dynamics of the base plate is modeled using the two-step FE reduction method described in sec. 3.1.1. The compatibility of the displacements between the housing and base plate is used to couple their responses during the excitation. In order to implement it, the nodes located on the housing - base plate interface (Fig. 3.6) are retained during the reduction process. Mathematically, the compatibility conditions can be expressed as follows:

$$\mathbf{u}_{hsng} = \mathbf{u}_{base} \tag{3.9}$$

where $\mathbf{u}_{hsng}$ and $\mathbf{u}_{base}$ are the displacements $(u_x, u_y, u_z)^T$ of the housing and base plate interface nodes respectively. Using the compatibility condition (eq. 3.9), we can express

equation of motion for the stationary unit of the support system assembly as follows:

$$\begin{bmatrix} M_{ss}^h & M_{si}^h & 0 \\ M_{is}^h & M_{ii}^h + M_{ii}^b & M_{is}^b \\ 0 & M_{si}^b & M_{ss}^b \end{bmatrix} \begin{Bmatrix} \ddot{u}_s^h \\ \ddot{u}_i^h \\ \ddot{u}_s^b \end{Bmatrix} + \begin{bmatrix} G_{ss}^h & G_{si}^h & 0 \\ G_{is}^h & G_{ii}^h + C_{ii}^b & C_{is}^b \\ 0 & C_{si}^b & C_{ss}^b \end{bmatrix} \begin{Bmatrix} \dot{u}_s^h \\ \dot{u}_i^h \\ \dot{u}_s^b \end{Bmatrix} + \begin{bmatrix} K_{ss}^h & K_{si}^h & 0 \\ K_{is}^h & K_{ii}^h + K_{ii}^b & K_{is}^b \\ 0 & K_{si}^b & K_{ss}^b \end{bmatrix} \begin{Bmatrix} u_s^h \\ u_i^h \\ u_s^b \end{Bmatrix} = \begin{Bmatrix} f_s^h \\ f_i^h \\ f_s^b \end{Bmatrix} \quad (3.10)$$

where the superscript h and b are used for the motor housing and the base plate, respectively. The subscripts i and s are used to distinguish between *interface* and *non-interface* nodes.

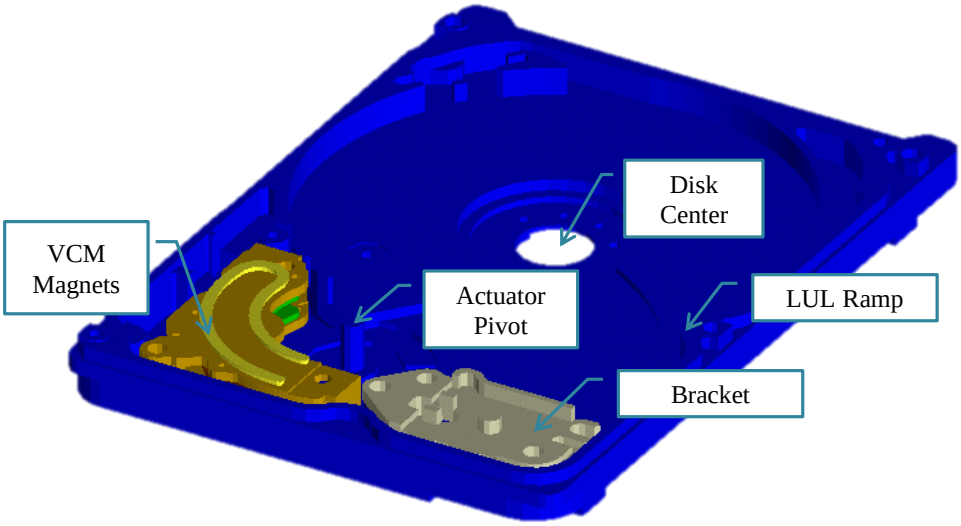

Figure 3.5: Construction of a base plate used in a mobile HDD

3.3 Support System Assembly

Once the model for the individual components of the disk-support system are developed, it is required to couple them together in order to get the complete system response. In the first step of this process, the disk is mounted on the motor hub assuming there is no clamping distortion. The displacement compatibility condition is used to couple their responses together, which can be expressed as follows:

$$\{w_i^{disk}\} = \{w_i^{hub}\} \quad (3.11)$$

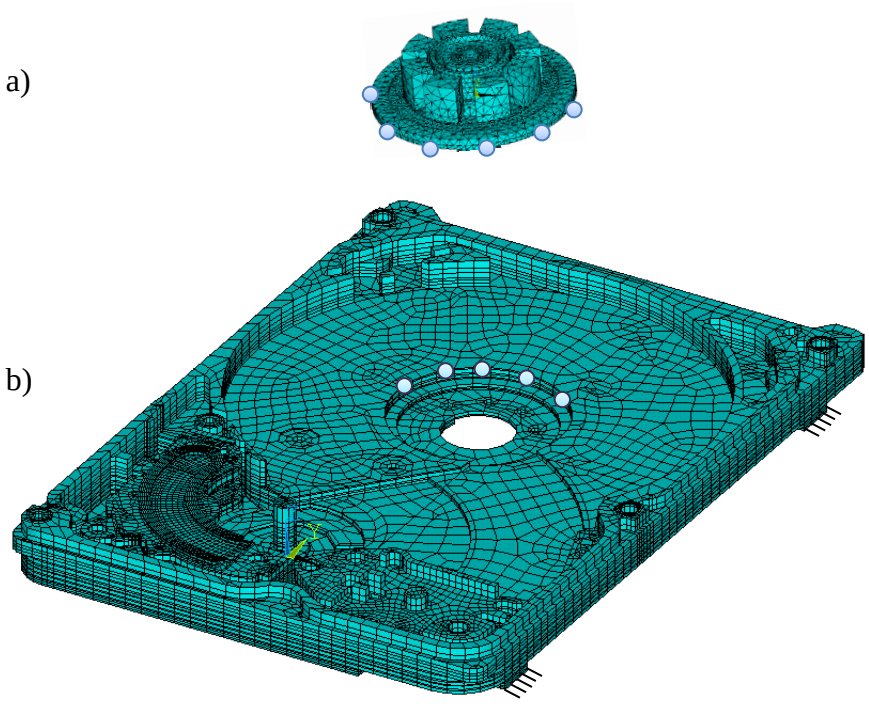

Figure 3.6: Coupling of base plate and motor housing

where $\{w_i^{disk}\}$ and $\{w_i^{hub}\}$ are the z displacements of the nodes present at the disk-hub interface (Fig. 3.7). Using the compatibility relations (eq. 3.11), we can combine the equations of motion of the rotating disk (eq. 2.18) and the hub (eq. 3.1a) as follows:

$$\begin{bmatrix} M_{ss}^d & M_{si}^d & 0 \\ M_{is}^d & M_{ii}^d + M_{ii}^h & M_{is}^h \\ 0 & M_{si}^h & M_{ss}^h \end{bmatrix} \begin{Bmatrix} \ddot{w}_s^d \\ \ddot{w}_i^d \\ \ddot{u}_s^h \end{Bmatrix} + \begin{bmatrix} G_{ss}^d & G_{si}^d & 0 \\ G_{is}^d & G_{ii}^d + C_{ii}^h & C_{is}^h \\ 0 & C_{si}^h & C_{ss}^h \end{bmatrix} \begin{Bmatrix} \dot{w}_s^d \\ \dot{w}_i^d \\ \dot{u}_s^h \end{Bmatrix} + \begin{bmatrix} K_{ss}^d & K_{si}^d & 0 \\ K_{is}^d & K_{ii}^d + K_{ii}^h & K_{is}^h \\ 0 & K_{si}^h & K_{ss}^h \end{bmatrix} \begin{Bmatrix} w_s^d \\ w_i^d \\ u_s^h \end{Bmatrix} = \begin{Bmatrix} f_s^d \\ f_i^d \\ f_s^h \end{Bmatrix} \quad (3.12)$$

where the superscripts d and h are used for the disk and the hub, respectively. It should be noted that the equations of motion (eq. 3.12) for the rotating unit presented here are derived for the rotational frame.

The governing equations for the rotor (eq. 3.12) and the stationary units (eq. 3.10) of the

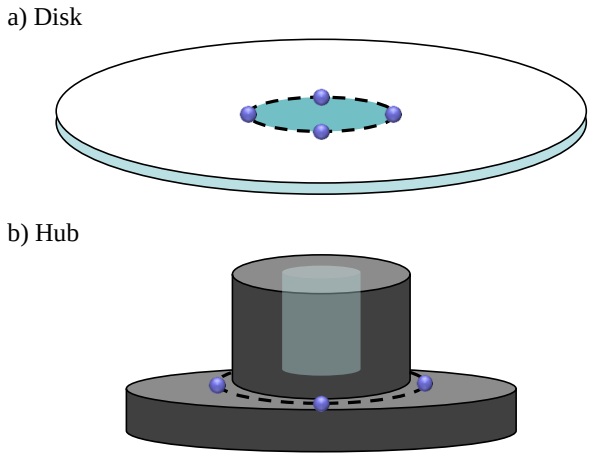

Figure 3.7: Mounting of the disk on a spindle motor hub

disk support assembly can be re-written as follows:

$$\begin{bmatrix} M^r_{oo} & M^r_{of} \\ M^r_{fo} & M^r_{ff} \end{bmatrix} \begin{Bmatrix} \ddot{u}^r_o \\ \ddot{u}^r_f \end{Bmatrix} + \begin{bmatrix} C^r_{oo} & C^r_{of} \\ C^r_{fo} & C^r_{ff} \end{bmatrix} \begin{Bmatrix} \dot{u}^r_o \\ \dot{u}^r_f \end{Bmatrix} + \begin{bmatrix} K^r_{oo} & K^r_{of} \\ K^r_{fo} & K^r_{ff} \end{bmatrix} \begin{Bmatrix} u^r_o \\ u^r_f \end{Bmatrix} = \begin{Bmatrix} 0 \\ f^r_f \end{Bmatrix} + \begin{Bmatrix} F^r_o \\ F^r_f \end{Bmatrix} \quad (3.13a)$$

$$\begin{bmatrix} M^s_{ff} & M^s_{fo} \\ M^s_{of} & M^s_{oo} \end{bmatrix} \begin{Bmatrix} \ddot{u}^s_f \\ \ddot{u}^s_o \end{Bmatrix} + \begin{bmatrix} C^s_{ff} & C^s_{fo} \\ C^s_{of} & C^s_{oo} \end{bmatrix} \begin{Bmatrix} \dot{u}^s_f \\ \dot{u}^s_o \end{Bmatrix} + \begin{bmatrix} K^s_{ff} & K^s_{fo} \\ K^s_{of} & K^s_{oo} \end{bmatrix} \begin{Bmatrix} u^s_f \\ u^s_o \end{Bmatrix} = \begin{Bmatrix} f^s_f \\ 0 \end{Bmatrix} + \begin{Bmatrix} F^s_f \\ F^s_o \end{Bmatrix} \quad (3.13b)$$

where the superscripts r and s denotes the the rotor and the stationary units, respectively. The subscript f is used for the nodes located on the meshing surfaces of the shaft and the sleeve at the location of the equivalent spring-dashpots representing the FDB. $\boldsymbol{F}$ represents the force acting on the system due to the external disturbance whereas $\boldsymbol{f}$ represents the reaction forces (eq. 3.8) due to deformation of the hydrodynamic bearings.

Due to the rotation of the spindle shaft, the spring-dashpot system nodes keep changing their positions on the sleeve surface. Since the number of nodes present on the sleeve is finite, the sleeve end of the spring-dashpot system often gets intercepted between the sleeve nodes as shown in Fig. 3.8. In such conditions, the reaction force due to the deformation of

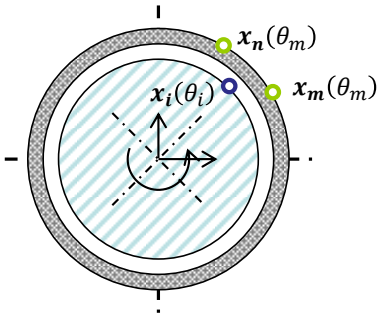

Figure 3.8: Rotating shaft nodes intercepted between sleeve nodes

the equivalent damper system can be obtained by modifying the eq. 3.8 as follows:

$$\mathbf{f}^r = -\mathbf{f}^s = -\mathbf{K}^{FDB}\left(\mathbf{u}^r - \tilde{\mathbf{u}}^s\right) - \mathbf{C}^{FDB}\left(\dot{\mathbf{u}}^r - \dot{\tilde{\mathbf{u}}}^s\right) \tag{3.14}$$

where $\tilde{\mathbf{u}}^s = (\tilde{u}^s_x, \tilde{u}^s_y, \tilde{u}^s_z)^T$ is the projected displacement of the sleeve at a point overlapping with the shaft node containing the equivalent FDB system. The projected sleeve displacement $\mathbf{u}^s$ can be obtained using linear interpolation of the displacements of the intercepting nodes m and n as shown in Fig. 3.9 as follows:

$$\mathbf{u}^s = \mathbf{u}^s_m\left(\frac{\theta_n - \theta}{\theta_n - \theta_m}\right) + \mathbf{u}^s_n\left(\frac{\theta - \theta_m}{\theta_n - \theta_m}\right) \tag{3.15}$$

where θ, θ_m and θ_n are the angular coordinates of the shaft node and its intercepting nodes m and n, respectively. The projected displacement evaluated in eq. 3.15 is specified in the stationary housing frame. It is required to be transformed to the shaft rotational frame in order to get the FDB deformation. Let $\theta_r(t)$ be the angular separation between the hub and the housing coordinate frames, then the sleeve displacement ($\tilde{\mathbf{u}}^s$) in the shaft frame can be written as follows:

$$\begin{Bmatrix} \tilde{u}^s_x \\ \tilde{u}^s_y \\ \tilde{u}^s_z \end{Bmatrix} = \begin{bmatrix} \cos\theta_r & \sin\theta_r & 0 \\ -\sin\theta_r & \cos\theta_r & 0 \\ 0 & 0 & 1 \end{bmatrix} \begin{Bmatrix} u^s_x \\ u^s_y \\ u^s_z \end{Bmatrix} \tag{3.16}$$

Once the reaction forces on the housing ($\tilde{\mathbf{f}}^s$) are evaluated using the eq. 3.14, they are required to be transformed back into the stationary frame as follows:

$$\begin{Bmatrix} f^s_x \\ f^s_y \\ f^s_z \end{Bmatrix} = \begin{bmatrix} \cos\theta_r & -\sin\theta_r & 0 \\ \sin\theta_r & \cos\theta_r & 0 \\ 0 & 0 & 1 \end{bmatrix} \begin{Bmatrix} \tilde{f}^s_x \\ \tilde{f}^s_y \\ \tilde{f}^s_z \end{Bmatrix} \tag{3.17}$$

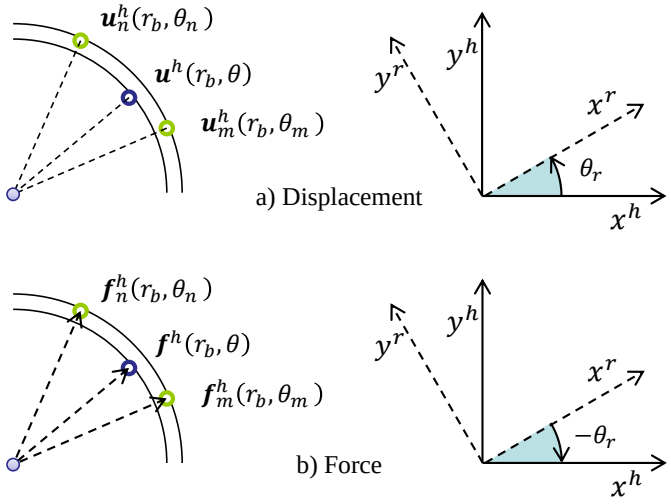

Figure 3.9: Interpolation formulation for the FDB equivalent system reaction forces

The FDB deformation forces acting at the spring-dashpot nodes are redistributed on the sleeve nodes as follows:

$$\mathbf{f}_m^s = \mathbf{f}^s\left(\frac{\theta_n-\theta}{\theta_n-\theta_m}\right) \quad \text{and} \quad \mathbf{f}_n^s = \mathbf{f}^s\left(\frac{\theta-\theta_m}{\theta_n-\theta_m}\right) \tag{3.18}$$

Substituting the value for FDB reaction forces (eq. 3.14 and 3.18) into eq. 3.13, we get the following equations of motion for the disk support system assembly:

$$\begin{bmatrix} M_{oo}^r & M_{of}^r & 0 & 0 \\ M_{fo}^r & M_{ff}^r & 0 & 0 \\ 0 & 0 & M_{ff}^s & M_{fo}^s \\ 0 & 0 & M_{of}^s & M_{oo}^s \end{bmatrix} \begin{Bmatrix} \ddot{u}_o^r \\ \ddot{u}_f^r \\ \ddot{u}_f^s \\ \ddot{u}_o^s \end{Bmatrix} + \begin{bmatrix} C_{oo}^r & C_{of}^r & 0 & 0 \\ C_{fo}^r & C_{ff}^r + C_{FDB}^{rr}(t) & C_{FDB}^{rs}(t) & 0 \\ 0 & C_{FDB}^{sr}(t) & C_{ff}^s + C_{FDB}^{ss}(t) & C_{fo}^s \\ 0 & 0 & C_{of}^s & C_{oo}^s \end{bmatrix} \begin{Bmatrix} \dot{u}_o^r \\ \dot{u}_f^r \\ \dot{u}_f^s \\ \dot{u}_o^s \end{Bmatrix} + \begin{bmatrix} K_{oo}^r & K_{of}^r & 0 & 0 \\ K_{fo}^r & K_{ff}^r + K_{FDB}^{rr}(t) & K_{FDB}^{rs}(t) & 0 \\ 0 & K_{FDB}^{sr}(t) & K_{ff}^s + K_{FDB}^{ss}(t) & K_{fo}^s \\ 0 & 0 & K_{of}^s & K_{oo}^s \end{bmatrix} \begin{Bmatrix} u_o^r \\ u_f^r \\ u_f^s \\ u_o^s \end{Bmatrix} = \begin{Bmatrix} F_o^r \\ F_f^r \\ F_f^s \\ F_o^s \end{Bmatrix} \tag{3.19}$$

where $C_{FDB}^{\alpha\beta}$ and $K_{FDB}^{\alpha\beta}$ $(\alpha,\beta = r,s)$ are the damping and stiffness contributions by the

FDB.

3.4 Numerical Techniques

The presence of the various components in the disk support assembly makes the simulation process time consuming. In the following section, we present two numerical techniques that have been used in the current model to reduce the computational cost.

3.4.1 Block Factorization

The equations of motion for the disk-motor-base plate assembly (eq. 3.19) are solved numerically using the *Newmark-Beta* scheme discussed in Sec. 2.4. The coefficient matrix A defined in eq. 2.28a can be expressed in block matrix form as follows:

$$\begin{bmatrix} A_{11} & A_{12} & A_{13} \\ A_{21} & A_{22}(t_n) & A_{23} \\ A_{31} & A_{32} & A_{33} \end{bmatrix} = \begin{bmatrix} M_{11} & M_{12} & M_{13} \\ M_{21} & M_{22} & M_{23} \\ M_{31} & M_{32} & M_{33} \end{bmatrix} + \beta_1 \Delta t \begin{bmatrix} C_{11} & C_{12} & C_{13} \\ C_{21} & C_{22}(t_n) & C_{23} \\ C_{31} & C_{32} & C_{33} \end{bmatrix} + \frac{\beta_2}{2} \Delta t^2 \begin{bmatrix} K_{11} & K_{12} & K_{13} \\ K_{21} & K_{22}(t_n) & K_{23} \\ K_{31} & K_{32} & K_{33} \end{bmatrix} \tag{3.20}$$

where C_{22} and K_{22} are the damping and stiffness sub-matrices of the disk and its support system having the time varying FDB contribution. As the coefficient matrix A changes at every time step, using a direct scheme like *Guass Elimination* to solve the system of equations (eq. 2.27) can be computationally expensive. However, the change in the matrix A is limited to the central block A_{22} and this can be exploited to speed up the computation. In order to achieve this goal, a *block factorization* scheme is proposed for the LU decomposition of the coefficient matrix A. In this method, the lower triangular matrix L and the upper triangular matrix U are expressed in the following block matrix form:

$$\begin{bmatrix} A_{11} & A_{12} & A_{13} \\ A_{21} & A_{22}(t_n) & A_{23} \\ A_{31} & A_{32} & A_{33} \end{bmatrix} = \begin{bmatrix} L_{11} & 0 & 0 \\ L_{21} & L_{22}(t_n) & 0 \\ L_{31} & L_{32}(t_n) & L_{33}(t_n) \end{bmatrix} \begin{bmatrix} U_{11} & U_{12} & U_{13} \\ 0 & U_{22}(t_n) & U_{23}(t_n) \\ 0 & 0 & U_{33}(t_n) \end{bmatrix} \tag{3.21}$$

Expanding the eq. 3.21 in component form, we can observe that following matrices are required to be evaluated only once:

$$
\begin{aligned}
L_{11}U_{11} &= A_{11} &&: L_{11} \text{ and } U_{11} \text{ are computed by LU decomposition} \\
L_{11}U_{12} &= A_{12} &&: \text{Columns of } U_{12} \text{ computed using forward substitution} \\
L_{11}U_{13} &= A_{13} &&: \text{Columns of } U_{13} \text{ computed using forward substitution} \\
L_{21}U_{11} &= A_{21} &&: \text{Rows of } L_{21} \text{ computed using forward substitution} \\
L_{31}U_{11} &= A_{31} &&: \text{Rows of } L_{31} \text{ computed using forward substitution}
\end{aligned}
$$

However, the rest of the L and U matrices are computed at every time step as follows:

$$
\begin{aligned}
L_{22}U_{22} &= A_{22} - L_{21}U_{12} &&: L_{22} \text{ and } U_{22} \text{ are computed by LU decomposition} \\
L_{22}U_{23} &= A_{23} - L_{21}U_{13} &&: \text{Columns of } U_{23} \text{ computed using forward substitution} \\
L_{32}U_{22} &= A_{23} - L_{31}U_{12} &&: \text{Rows of } L_{32} \text{ computed using forward substitution} \\
L_{33}U_{33} &= A_{33} - L_{31}U_{13} - L_{32}U_{33} &&: L_{33} \text{ and } U_{33} \text{ are computed by LU decomposition}
\end{aligned}
$$

Fig. 3.10 shows the sizes of the block matrices defined in eq. 3.21 generated in a disk support assembly model. It can be observed that the LU matrices that need to be evaluated at every time step are relatively smaller and hence take require less effort. The block LU factorization scheme presented in this section is able to speed up the solution process by a factor of 10.

$$
\begin{array}{r}
 \overset{m}{\longleftrightarrow} \quad \overset{n}{\longleftrightarrow} \quad \overset{p}{\longleftrightarrow} \\
m \approx 1850 \updownarrow \\
n \approx 150 \updownarrow \\
p \approx 300 \updownarrow
\end{array}
\begin{bmatrix}
A_{11} & A_{12} & A_{13} \\
A_{21} & A_{22}(t_n) & A_{23} \\
A_{31} & A_{32} & A_{33}
\end{bmatrix}
$$

Figure 3.10: Size of block matrices generated in a disk support assembly model

3.4.2 Sparse Map

Fig. 3.11 shows the non-zero entries in a stiffness matrix of the disk support assembly. It can be observed that the matrix shown here is sparsely populated. Storing only the non-zero elements of the matrices does not only help in reducing the dynamic memory requirement

but it can also help in cutting down the simulation time. The system matrices in the current analysis are stored symbolically using a special technique called *sparse-map*. In this method, the non-zero entries in each row of the matrix are identified by their column number and recorded in a map as shown in Fig. 3.12. This technique is able to reduce the simulation time by half.

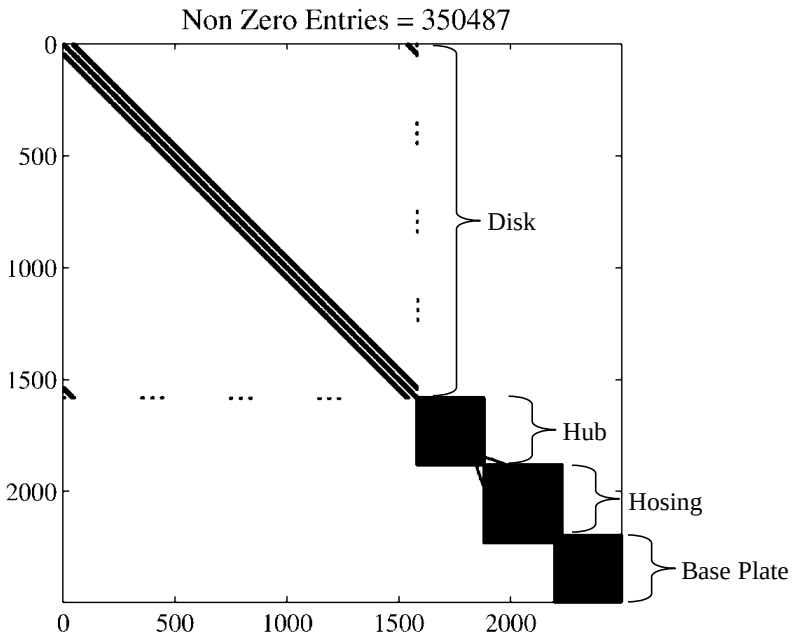

Figure 3.11: Non-zero entries in a stiffness matrix for the disk support assembly

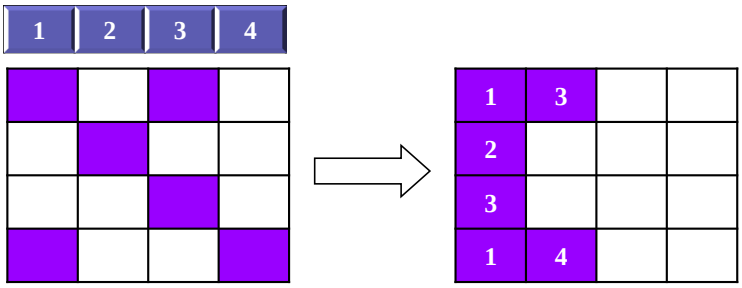

Figure 3.12: An example of sparse-map symbolic storage

3.5 Closure

A detailed model for the disk support system is presented in this chapter which consists of a FDB based spindle motor mounted on a flexible base plate. This model has the capability of simulating the disk dynamics for a generalized excitation. The numerical techniques used to increase the computational efficiency of the model are also discussed in this chapter.

Chapter 4

System integration

In this chapter, we present a methodology used for coupling the different components present in a HDD in order to get the complete system response. The numerical methods used for modeling of the actuator assembly and the air bearing are discussed. For a better understanding of the operational shock simulator, we include in this chapter a schematic diagram showing the disk geometry and a flowchart explaining the simulation process.

4.1 Actuator Modeling

As discussed earlier, the slider containing the read/write head is loaded onto a spinning disk with the help of a suspension. Fig. 4.1 shows a schematic diagram of a slider attached to the suspension. This is known as the head gimbal assembly (HGA). The slider is mounted on the suspension's *flexure beam*, which is pressed onto the disk by the *load beam* through a *dimple*. During the unloading process, a tab present on the tip of load beam gets engaged with the parking ramp and pulls the slider up from the disk. However, due to the sub-ambient pressure created in the air bearing, the slider gets pulled down, which opens up the dimple and increases the gap between the flexure and the load beam. Eventually when the air bearing breaks down, if the separation between the two beams is too large, the spring back action of the flexure beam can cause damage to the system. In order to avoid it, *limiters* are provided in the suspension, which get engaged when the separation between the two beams exceeds a certain threshold. The head gimbal assembly is mounted on an E-block which provides the in-plane actuation for the slider seeking a particular track on the disk. Continuing the approach used for structural modeling for the disk support system,

we use a FE reduction method to model the response of the actuator assembly. During an axial disturbance, the opening of dimple and engaging of limiters can affect the slider dynamics. A technique proposed by Hughes et al. is used to model the contact between the pairs mentioned above. In order to implement this method, it is required to identify the contact nodes and retain them during the reduction process. More details about the actuator modeling can be found in Bhargava 2008.

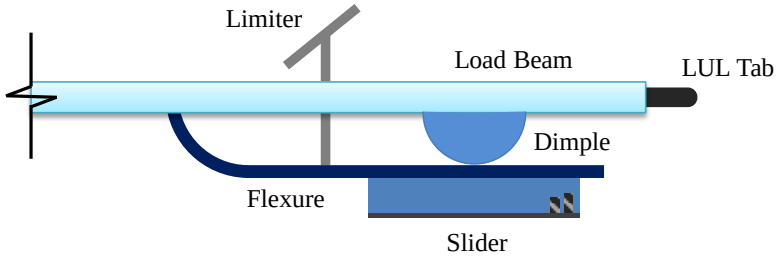

Figure 4.1: A schematic diagram of a head gimbal assembly

4.2 Air Bearing

The ability of the head-disk interface (HDI) to withstand an operational shock depends on the robustness of the air bearing formed between them. In order to get a satisfactory HDI response, it is important to accurately capture the dynamic behavior of the air bearing during the disturbance. Fig. 4.2 shows the design of the slider's air bearing surface (ABS) used in a commercial HDD. The particular form factor ($1.25mm \times 1.00mm$) shown here has an industrial name of *pico* slider. Different colors polygons on the slider's surface represents the different etch depths with the base recess represented by the white background. The narrow channels provided near the slider's trailing edge helps to remove any contamination particles that get trapped during the operation. The design of the ABS is a critical parameter in determining the slider's flying characteristics.

The air flow under the slider is governed by the Reynolds lubrication equation, which is written as follows:

$$\frac{\partial}{\partial x}\left(Q\left(K_n\right)ph^3\frac{\partial p}{\partial x}-6U\mu ph\right)+\frac{\partial}{\partial y}\left(Q\left(K_n\right)ph^3\frac{\partial p}{\partial y}-6V\mu ph\right)=12\mu\frac{\partial}{\partial t}\left(ph\right) \qquad (4.1)$$

where p, h, μ, U and V are the air pressure, head disk separation, coefficient of air viscosity, air flow velocity components along x and y directions, respectively. The minimum separation

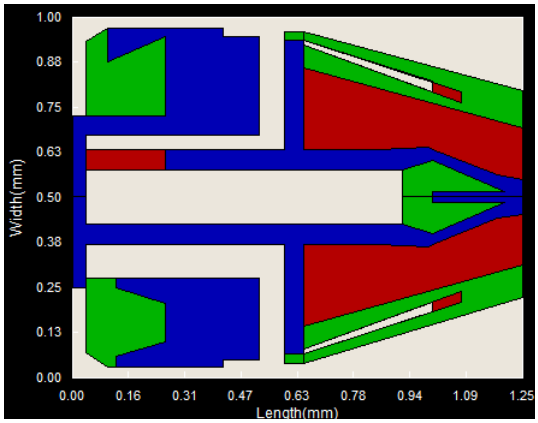

Figure 4.2: An air bearing surface design of a *pico* slider

between the slider and disk ($\sim 10nm$) is of the order of the mean free path of air and hence the viscous no-slip assumptions at their surfaces is not appropriate. A correction factor Q is introduced into the Reynolds equation to accommodate the *slip* effect at the boundary. There have been various models proposed in the literature for evaluating the slip correction factor. A good comparison study about the different slip models can be found in Chen and Bogy 2010. The correction factor evaluated by Fukui and Kaneko is used in the current system. In their study, they have numerically solved the linearized *Boltzman* equation to generate a database for the correction factor Q as a function of the Knudsen number K_n, which is defined as the ratio of air mean free path λ to the local clearance h. While solving the Reynolds equation, Q is evaluated for a given Knudsen number by interpolating the FK database.

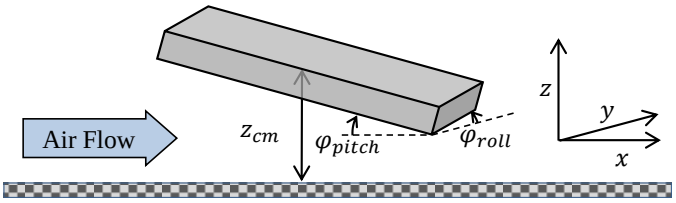

Figure 4.3: Slider orientation with respect to the spinning disk

The Reynolds equation for the air bearing is solved numerically to get the pressure distribution under the slider for a given HDI configuration. The clearance h between the two surfaces at a given point (x, y) can be determined by the slider's orientation, which is specified

in terms of the z-height z_{cm}, pitch ϕ_{pitch} and roll ϕ_{roll} as shown in Fig. 4.3. The eq. 4.1 can be expressed as a standard convection-diffusion partial differential equation (PDE). A finite volume method (FVM) is a popular numerical method to solve this class of PDEs [Patankar 1980]. In this method, the air bearing surface is divided into small rectangular cells and the pressure is evaluated for each cell. During the discretization process, it is ensured that all of the geometrical features present on the ABS are captured by the rectangular grid. Hence for a complex air bearing design, a denser mesh is required to capture its geometry which in turns increases the simulation time. A multigrid scheme was implemented to increase the computational speed [Briggs et al. 2000]. A detailed description of the implementation of this method can be found in Lu 1997.

4.3 Contact Forces

The failure of the head-disk interface is often accompanied by a contact between the slider and the disk. The magnitude and the pressure of the contact force are often used to measure the seriousness of the HDI failure. The contact force between the slider and the disk consists of two components, the *asperity contact* force and the *impact* force. In the following section, we explain the process of evaluating these two types of contact forces.

4.3.1 Asperity Contact

The contacting surfaces of the slider and disk are not perfectly smooth (Fig. 4.4) and hence when they come close to each other, asperities present on their surface start interacting with each other. The *Greenwood-Williamson* model [Greenwood and Williamson 1966] is used to evaluate the force arising due to asperity contact. In their approach, they assumed that all asperity summits have the same radius but different heights. The normal force arising from the elastic deformation of the asperity is computed using the *Hertzian* contact model. The surface material properties such as Young's Modulus (E) and Poisson's ratio (ν) and its roughness parameters which include asperity density (η), radius (β) and the distribution of the asperity heights ($\phi(z)$), are required to compute the asperity contact force. In the simulation, asperity contact forces are only evaluated when the minimum clearance (h_{min}) between the slider and disk is lower than a certain threshold limit. This clearance is known as the *glide height* (GH).

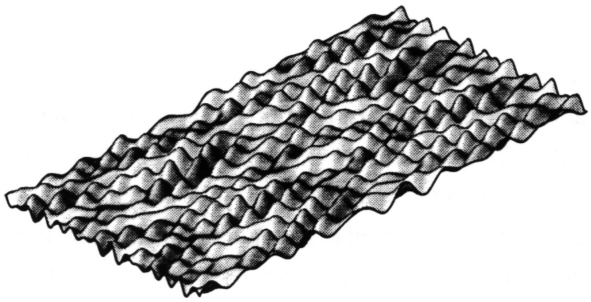

Figure 4.4: Surface roughness

4.3.2 Impact Force

The impact force is generated due the bulk deformation of the elastic (glass) disk substrate by the relatively rigid (AlTiC) slider block. A semi-analytical technique, proposed by Bhargava is used to evaluate the contact force during the slider - disk collision. In this method, they have modeled the disk deformation as a quasi-static process in which the concentrated force acts on a semi infinite elastic medium. In linear elasticity this is knowns as the *Boussineq* problem in which deformation **u** is determined for the given point force **F**. The boundary element method (BEM) is used to solve the inverse problem of finding the contact pressure p_{impact} for a given deformation profile. The analytical solution for Boussineq problem [Luré 2005] is used as a *Green's* function for the BEM. In this model, the effect of various overcoats present on the disk surface was neglected.

4.4 Proximity Forces

As the clearance between the HDI reduces to less than 5nm, forces due to intermolecular and electrostatic attraction become significant. These forces shows an inverse relationship with head media spacings and they can make the HDI unstable at low clearances. In the following section we explain the process involved in computing these proximity forces between the slider and disk surfaces.

4.4.1 Intermolecular Forces

All the atoms and molecules exhibit intermolecular forces, even if they are neutral. The origin of these forces can be explained on the basis of wave theory for the atomic particles.

The pair potential for two molecules can be obtained by summing up the attractive and repulsive components. On integrating the potential of one molecule interacting with the infinite area of the opposite surface, we can get the potential per unit area (U_{IMF}). The force normal to the interacting surfaces can be obtained by differentiating the potential with respect to the normal distance as follows:

$$f_{IMF}(z) = -\frac{\mathrm{d}U_{IMF}}{\mathrm{d}z} = -\frac{A}{6\pi}\iint_A \frac{\mathrm{d}A}{z^3} + \frac{B}{45\pi}\iint_A \frac{\mathrm{d}A}{z^9} \tag{4.2}$$

where A and B are the Hamaker constants which depend on the dielectric constant and refractive index of the media. More details about this formulation can be found in Gupta and Bogy 2006a,b.

4.4.2 Electrostatic Forces

When a slider flies very close to the disk surface, there can be a charge build up on its surface due to the frictional contact. This phenomenon is known as *tribocharging* [Kiely and Hsia 2002]. An electrostatic force of attraction is experienced by the slider-disk pair due to the potential difference developed between them. The normal component of the electrostatic force f_{Elec} can be computed by differentiating the electrostatic potential U_{Elec} defined per unit surface area and then integrating it over the slider's surface as shown:

$$f_{Elec}(z) = -\frac{\mathrm{d}U_{Elec}}{\mathrm{d}z} = -\frac{\epsilon_0 k_e V^2}{2}\iint_A \frac{\mathrm{d}A}{z^2} \tag{4.3}$$

where ϵ_0, k_e and V are the permittivity constant, dielectric constant for air and potential difference between slider and disk.

4.5 HDD Geometry

In order to couple the response of the different components present in a mobile HDD, it is important to know their relative positions with respect to each other. Fig. 4.5 shows the location of a slider, a L/UL ramp, the spindle motor and the actuator pivot in a HDD base plate. The slider's position can be defined by specifying its radial distance from the disk center r_a, the actuator length x_{act} (actuator pivot to slider mass center distance) and the skew angle ϕ which is defined as the angular separation between the actuator axis and air flow velocity vector (Fig. 4.6). This location is known as the slider's *reference position*. The slider's track seeking motion can be specified by defining the actuator separation from the

reference position. Once the slider is located, the distance between the actuator pivot and the spindle motor center x_0 can be calculated. In order to locate the disk-motor assembly, in addition to the center to center distance x_0, it also required to specify the base angle θ_{base}, which is shown in Fig. 4.5. The location of the L/UL ramp can be specified similarly by defining its radial position x_{ramp} and the angular separation θ_{ramp} with respect to slider's reference position.

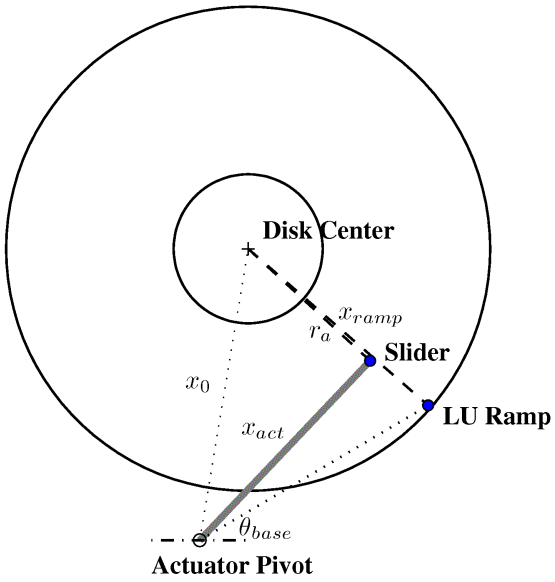

Figure 4.5: A schematic digram showing the HDD geometry

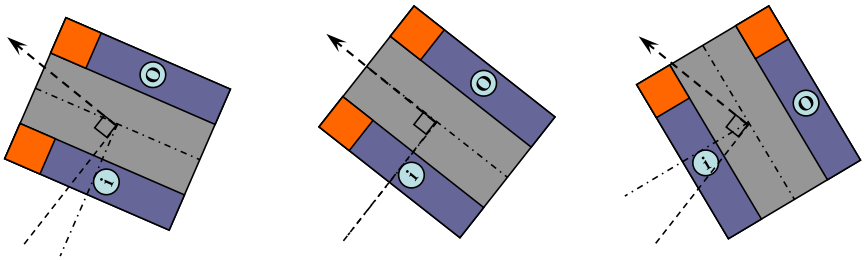

Figure 4.6: IDEMA convention for determining slider skew

4.6 Simulation Algorithm

The flowchart shown in Fig. 4.7 summarizes the *op-shock* simulation process. In the beginning, a rectangular grid is generated for the air bearing surface. The FE matrices for the spinning disk are then computed and coupled with the imported reduced matrices for the support assembly structural components. The simulations starts with an initial guess for slider's flying attitude $\mathbf{x}_o^t$, which include nominal flying height (NFH), pitch and roll. The deformation of the disk $\mathbf{x}_d^t$ mounted on the flexible support system is computed at that particular time step t_n. It is then used to determine the slider's orientation with relative to the deformed disk. During the simulation, it was observed that the effect of slider's load on the disk displacement was negligible in comparison to the inertia load during the shock. Hence one-way coupling is implemented in the simulator. If the minimum clearance between the slider and disk is less than the glide height, then the time step size (Δt) is reduced to one tenth in order to capture the slider's dynamics. The Reynolds equation is solved to get the pressure distribution under the slider, which is further integrated to get the air bearing forces and moments. The contributions from the intermolecular, electrostatic and contact forces are also added to the air bearing force get the net force acting on the slider. By solving the force equilibrium problem, we determine the new attitude $\mathbf{x}_n^t$ for the suspension mounted slider. If the difference between the two slider attitudes is higher then the threshold ε, then the whole process is repeated by using $\mathbf{x}_n^t$ as the new slider orientation. This technique is known as the *fixed point* iteration scheme. Once the convergence is reached at a particular time step, the actuator and disk are advanced to their new location.

4.7 Closure

In this chapter, we have explained the process of assembling the individual components present in a mobile HDD to get the complete system response during a dynamic event. A brief description about the modeling of the actuator assembly and the air bearing is also included in this chapter.

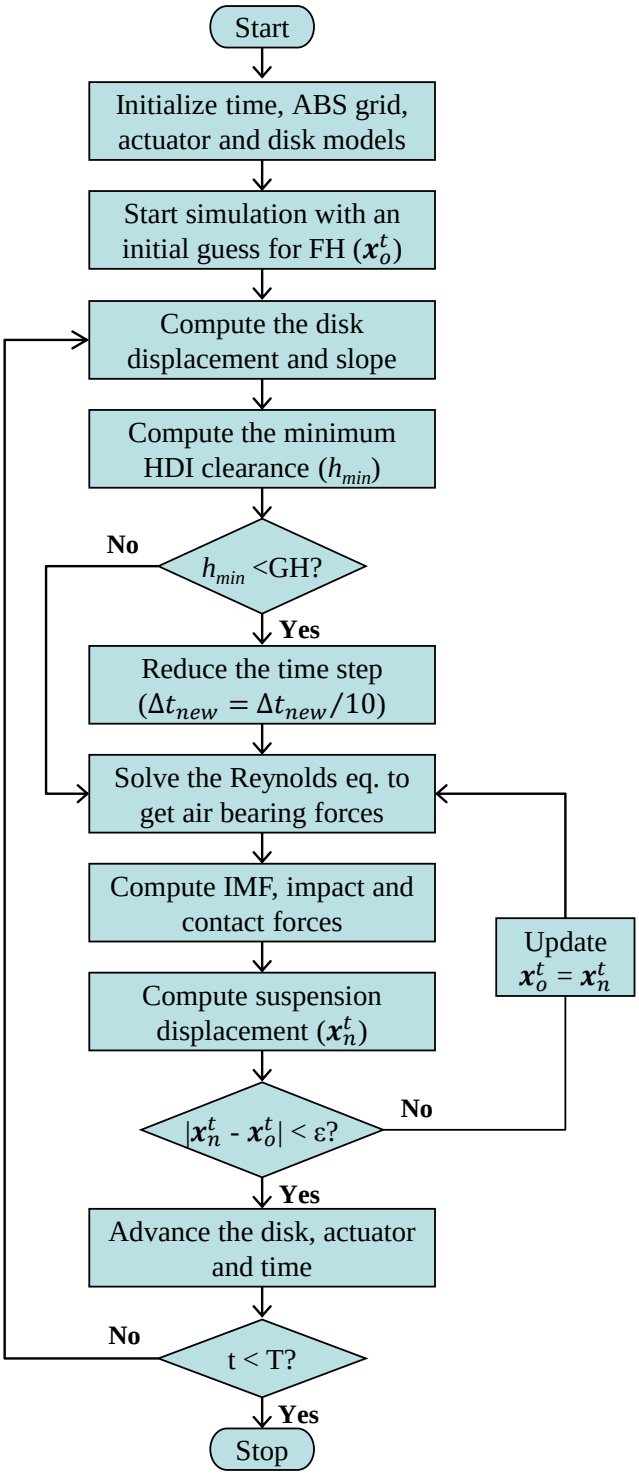

Figure 4.7: A flowchart explaining the CML *op-shock* simulator's algorithm

Chapter 5

Study of vertical operational shocks

In this chapter we present a case study to understand the effect of HDD components' dynamics on the stability of a head disk interface during an axial operational shock. The terminology used for describing a shock is introduced in the section 5.1. Section 5.2 gives the details about the design of the mobile disk drive used in the current study. The rest of this chapter discusses the effect of individual components such as the disk and its support assembly on the shock performance of the HDI. The results from the numerical investigations are summarized in the end.

5.1 Shock Terminology

In this section we explain the terminology used for defining a shock event. The convention used for defining the orientation of a vertical shock is also discussed.

5.1.1 Waveform

In this study, shock is modeled as a half sine acceleration wave as shown in Fig. 5.1. It is defined by its amplitude (A) and its pulse width (T_{pw}). The amplitude measures the intensity of shock whereas the pulse width can be used to characterize the HDD's working environment. For an example, if a laptop falls from a desk, the height of the fall will determine the shock amplitude whereas the pulse width will depend on the impacting surface. A wooden floor will have a shorter pulse width in comparison to a carpeted floor. The excitation frequency

f_{shock} for a shock pulse is determined by its pulse width as follows:

$$f_{shock} = \frac{1}{2T_{pw}} \tag{5.1}$$

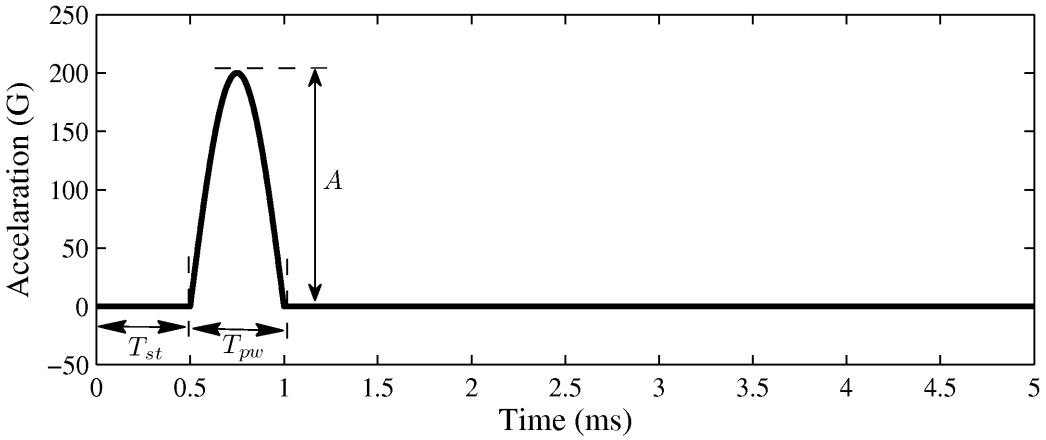

Figure 5.1: A half sine wave representing a shock pulse

5.1.2 Orientiation

Vertical shocks are categorized as *positive* or *negative* depending on the orientation of the drive relative to the direction of the impact. A positive shock is defined as one that causes the disk to move towards the slider (Fig. 5.2). In a negative shock the disk is followed by the slider. It should be noted that the orientation discussed here is defined for a slider-disk pair. In a commercial HDD, sliders are present on both sides of the spinning disk. Hence a positive shock for a slider flying on top of the disk will be a negative shock for the other slider.

5.2 HDD Design

The numerical study is conducted on a commercial 2.5 inch mobile HDD that uses a *femto* air bearing slider as shown in Fig 5.3. Its design parameters are summarized in Table 5.1.

As suggested by the form factor, a glass disk of outer diameter 65 mm (2.5 in) and thickness 0.64 mm is used in this study. The material properties of the glass disk are listed in Table 5.2.

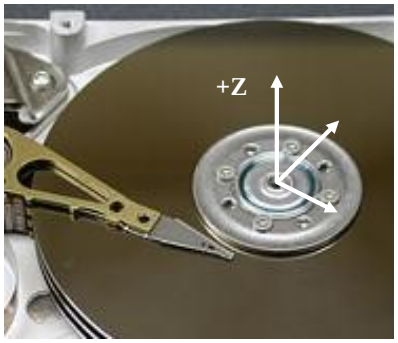

Figure 5.2: Sign convention for vertical shock

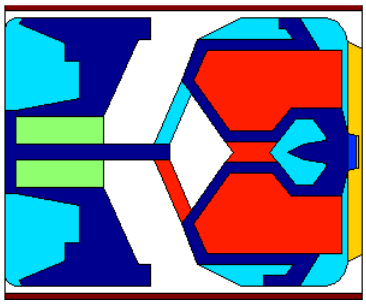

Figure 5.3: Air bearing surface design for a *femto* slider

Table 5.1: Femto slider design parameters

Dimensions	0.85 mm × 0.70 mm × 0.23 mm
Suspension Load	2.5 gms
Disk RPM	5400
Nominal Flying Height	13.0 nm
Pitch	60.0 μrad
Roll	3.0 μrad

Table 5.2: Material properties of glass disk

Young's Modulus	75 GPa
Poisson's Ratio	0.3
Density	2710 Kg/m^3

The disk drive model contains a FDB based spindle motor. The stiffness and the damping coefficients for the equivalent spring-dashpot systems representing the FDB (sec. 3.1.2) are shown in Tables 5.3 and 5.4, respectively.

Table 5.3: Stiffness coefficients for FDB equivalent system

Location	K_{xx}	K_{xy}	K_{zz}
Top Journal Bearing	3.12×10^6 N/m	5.94×10^6 N/m	0
Bottom Journal Bearing	1.61×10^6 N/m	2.25×10^6 N/m	0
Thrust Bearing	0	0	1.31×10^5 N/m

Table 5.4: Damping coefficients for FDB equivalent system

Location	C_{xx}	C_{xy}	C_{zz}
Top Journal Bearing	1.94×10^4 N-s/m	5.05×10^4 N-s/m	0
Bottom Journal Bearing	2.03×10^4 N-s/m	4.50×10^4 N-s/m	0
Thrust Bearing	0	0	1.27×10^3 N-s/m

During a vertical shock, the disk's displacement is maximum near its outer edge. Hence during the simulation, the slider is placed near the disk OD (Fig. 4.5) to capture the worst case scenario during a operational shock.

5.3 Modal Analysis

The proximity of the excitation frequency to the HDD components' natural frequencies can result in *resonance*. The high vibration amplitude caused during the resonance has an adverse effect on the stability of a HDI. In the current analysis, the HDD is subjected to shocks with the pulse widths ranging from 0.2 ms to 3.0 ms, which corresponds to excitation frequencies of 133 - 2500 Hz (eq. 5.1). The first few frequency modes of the HDD components are listed in Table 5.5.

The stiffness of the FDB in a spindle motor is much smaller in comparison to the rigidity of its structural components. Hence, during an op-shock, the response of the motor is governed by the FDB dynamics.

Table 5.5: HDD Components natural frequencies

Spinning Disk			Base Plate		Actuator Assembly	
Mode	Frequency		Mode	Frequency	Mode	Frequency
	Forward	Backward				
$(0,0)$	1043 Hz	1043 Hz	Umbrella	1313 Hz	1^{st} Bending	445 Hz
$(0,1)$	1210 Hz	850 Hz	Bending	2241 Hz	Flexure Bending	1046 Hz
$(0,2)$	1604 Hz	885 Hz	Twisting	3329 Hz	2^{nd} Bending	1642 Hz

5.4 Effect of Disk Dynamics

In this section we investigate the effect of the spinning disk's dynamics on the operational shock performance of the HDI. In order to isolate the effect of the spinning disk, it is first mounted on a rigid base. The minimum clearance between the slider and the disk surface (h_{min}) is used as the failure criterion. When h_{min} becomes less than zero, the HDI is 'failed'.

Fig. 5.4 shows the response of a spinning disk for a positive shock of 200G in the absence of a L/UL ramp. For a pulse width less than or equal to 0.5 ms the disk vibrates with constant amplitude after the initial impulse, whereas at a larger pulse width it has an initial peak displacement followed by residual vibrations. This change in the disk's behavior is expected to affect the mechanism of the HDI failure at different pulse widths.

Fig. 5.5 shows a comparison of the response of the HDI for two different orientations of the HDD when it is subjected to a vertical op-shock of pulse width 0.2 ms and amplitude 650G. The variation of h_{min} in the two configurations is similar except during the shock pulse. Due to the shock the HGA gets excited in its 2^{nd} bending mode (Figs. 5.5(c) and (d)) causing a phase difference between the disk's and the slider's motion. After the initial impulse, a sustained disk vibration continues to excite the HDI, and eventually the phase difference causes its failure as shown in Fig. 5.5(e). On further increase in the shock amplitude, the point contact between the slider and disk gradually becomes a line contact along the slider's edge resulting in a monotonic increase in contact force.

At a larger pulse width (2.0 ms) the orientation of the HDD during an op-shock (600G) has its effect on the behavior of the HDI as shown in Fig. 5.6. At this pulse width the disk has its peak displacement during the shock pulse interval (Fig. 5.4) and hence h_{min} attains its minimum value during the same period.

In the case of a positive shock the suspension, being more flexible, has a larger displacement than the spinning disk (Fig. 5.6(a)). As the separation between the slider and disk

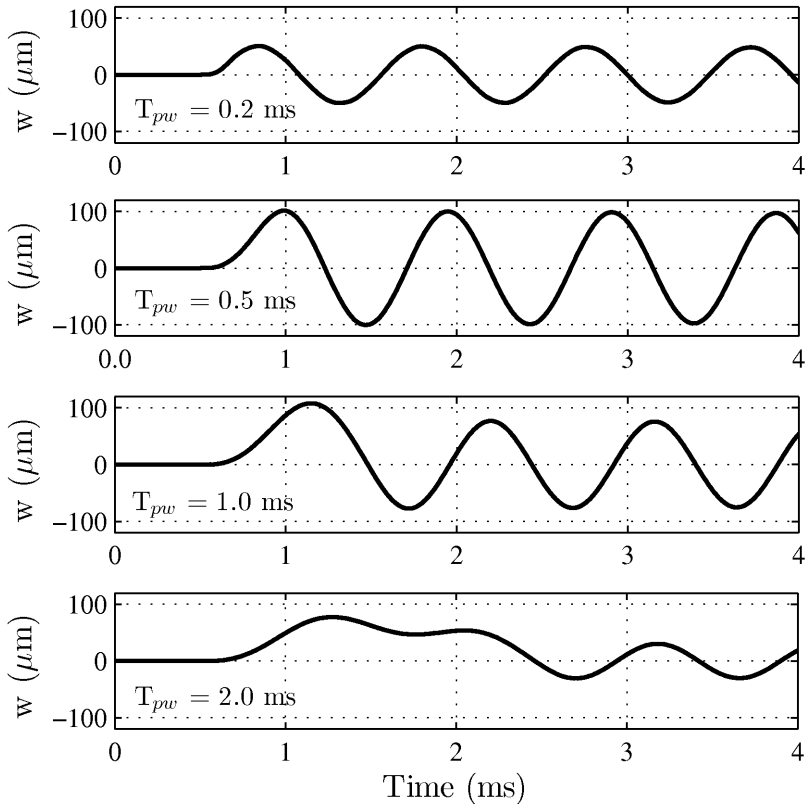

Figure 5.4: Disk displacement at the OD for positive shock of 200G

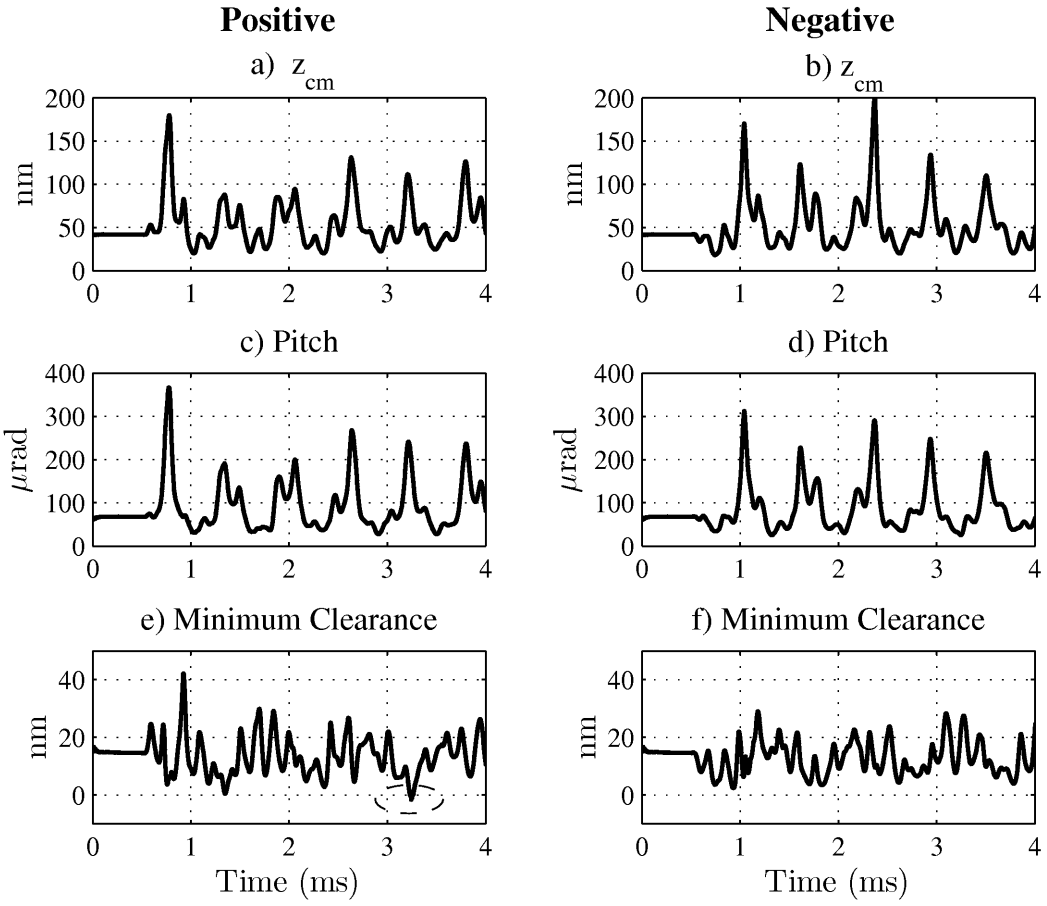

Figure 5.5: HDI response during an op-shock of pulse width 0.2 ms

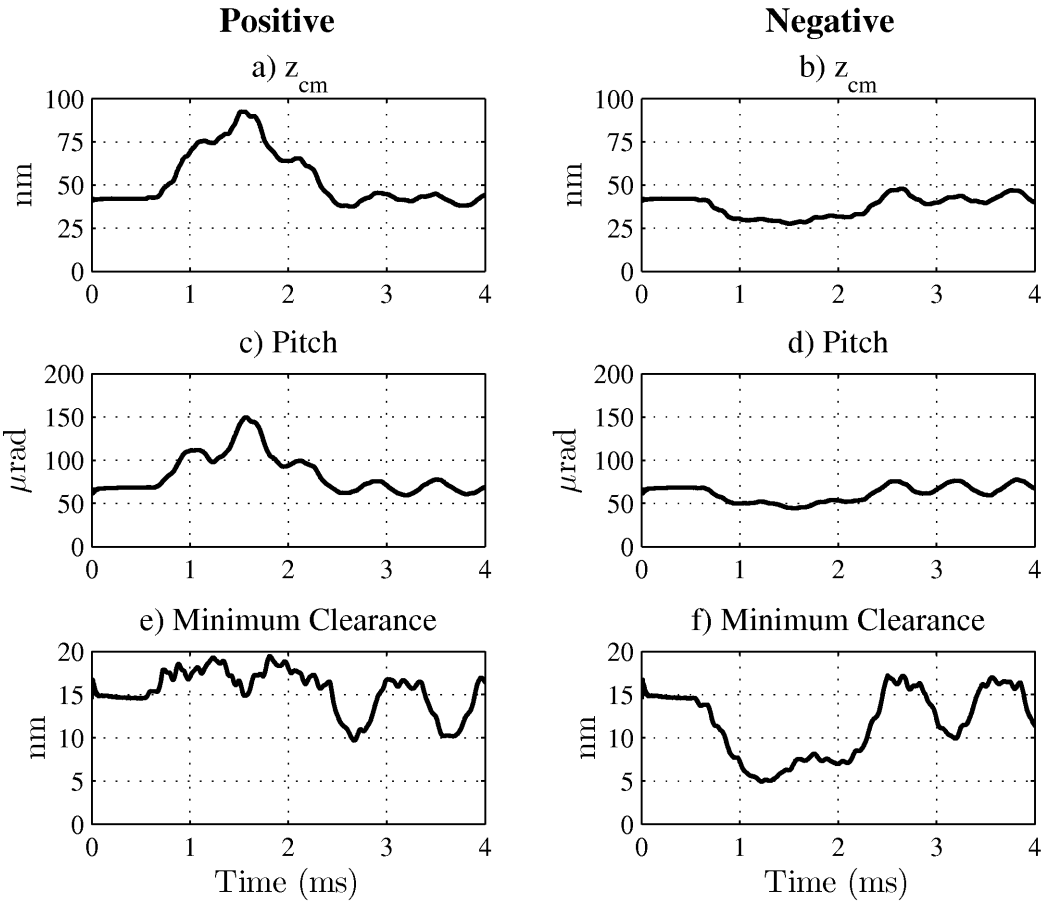

Figure 5.6: HDI response during an op-shock of pulse width 2.0 ms

increases with the shock amplitude, the resistive (positive) pressure from the air bearing starts diminishing. However, the negative pressure from the air bearing decays slowly and keeps the disk and suspension motion coupled together (Fig. 5.7 (a)). With further increase in the shock amplitude (990G), the air bearing eventually collapses, allowing the suspension to oscillate freely. During the oscillation, when the slider's motion returns towards the disk, its high momentum does not allow the formation of an air bearing. In absence of any resistive force, the slider directly crashes into the disk with a high impact force (2455 mN). This HDI failure mechanism is known as *head-slap*. The high contact force resulting from the slider-disk collision can cause wear of the magnetic layer.

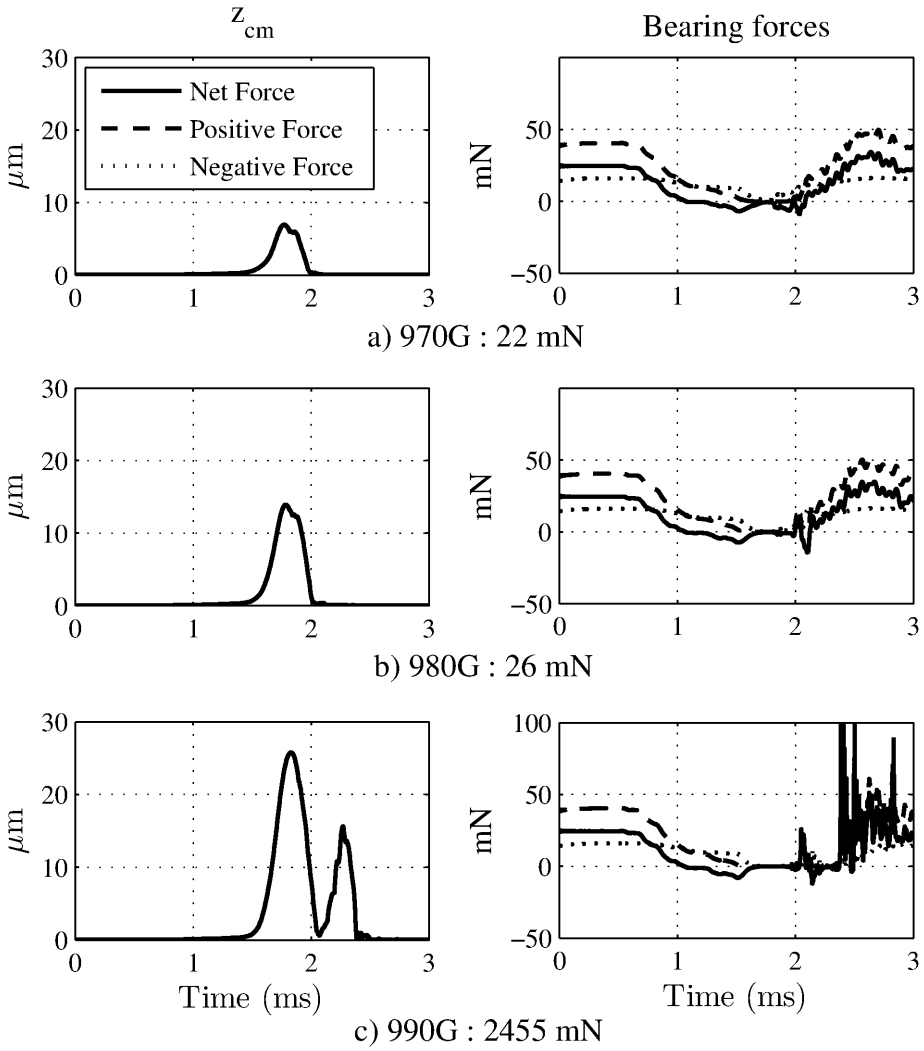

Figure 5.7: Failure of HDI due the *head-slap*

In the other orientation the HDI responds differently to the shock. Due to the flexibility difference between the slider and disk the air bearing gets compressed during the shock pulse. Higher air bearing forces caused by the compression restricts the free bending motion of the HGA causing the slider to *flatten* down (pitch reduces) on the disk surface during the shock as shown in Fig. 5.6(d). In this orientation the failure of the HDI occurs only when the inertia forces due to the shock can overcome the resistive air bearing forces (Fig. 5.8).

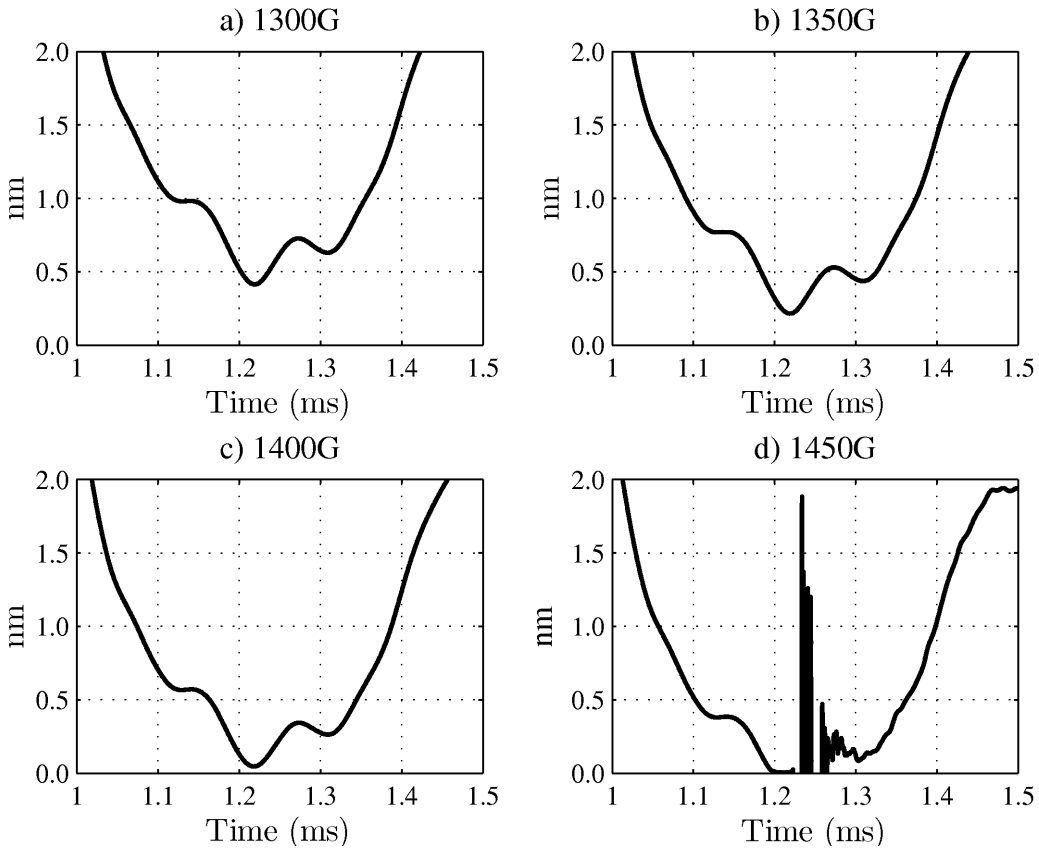

Figure 5.8: Failure of HDI due the air bearing compression

Fig. 5.9(a) compares the responses of a stationary and a spinning disk to a negative op-shock (A = 200G and T_{pw} = 2.0 ms) in the presence of a L/UL ramp. It can be observed that using the stationary disk deformation to predict the response of a spinning disk during a disk-ramp collision is not a good approximation. Fig. 5.9(b) shows the frequency spectrum for the spinning disk's transverse displacement. The peaks shown in the figure correspond to the high frequency asymmetric disk's modes that get excited during the disk's collision with the stationary ramp.

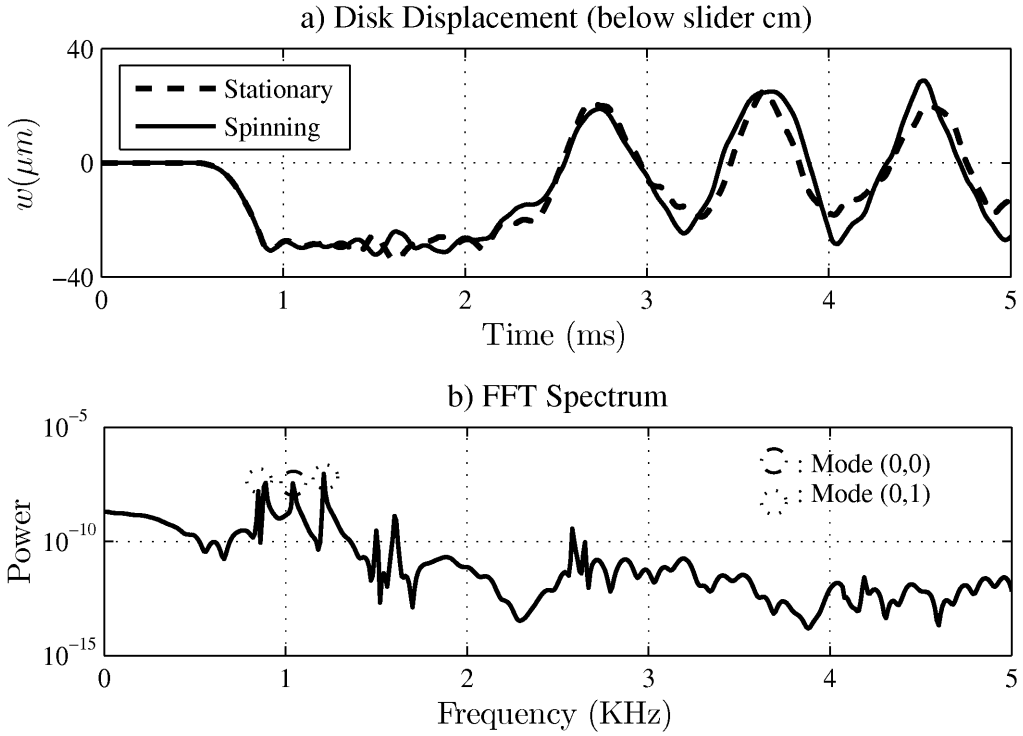

Figure 5.9: Effect of ramp contact on the disk dynamics

The effect of the disk-ramp collision on the HDI stability is discussed next. Fig. 5.10 shows the response of the HDI to a positive shock of pulse width 2.0 ms and amplitude 250G. During the collision the disk's motion is intercepted by the parking ramp, while the HGA's motion remains unrestricted, resulting in a phase difference. In addition, the contact force applied by the LUL ramp excites the spinning disk in asymmetric vibration dominated by the (0,1) mode (1027 Hz) as shown in Fig. 5.10(b). The phase difference and the high frequency content of the disk's asymmetric vibration excites the air bearing modes (Fig. 5.10(c)) resulting in HDI failure as shown in Fig. 5.10(d).

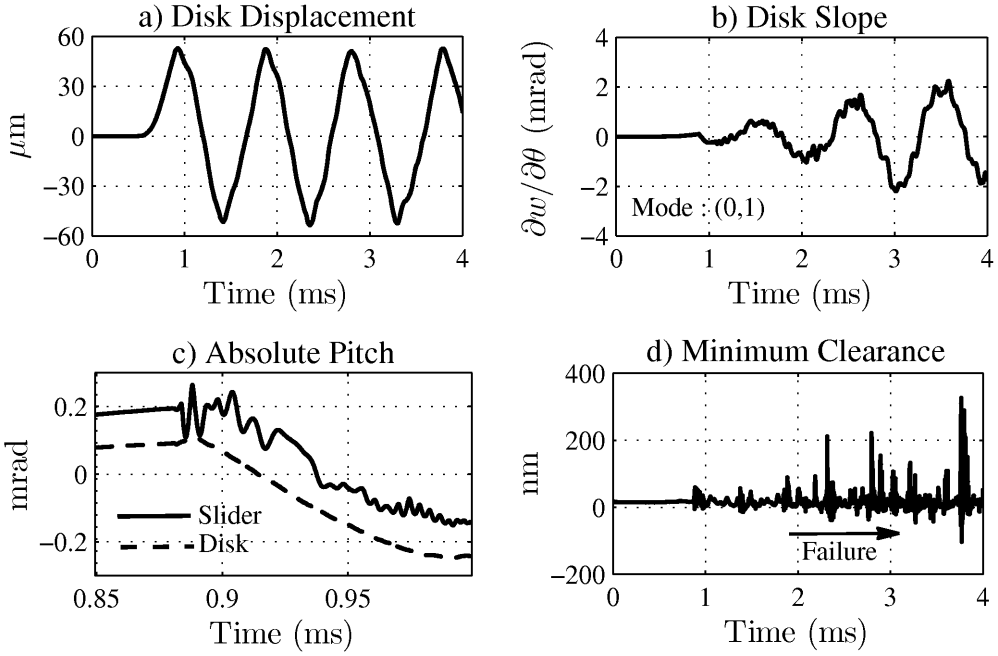

Figure 5.10: HDI response during collision of spinning disk with LUL ramp

Table 5.6 shows the variation of contact force between the slider and the disk during a negative op-shock. In the absence of the LUL ramp in the system, when the shock amplitude is increased above the shock resistance, there is monotonic increase in the contact force. Such behavior is not exhibited when the parking ramp is present in the system.

In the absence of disk-ramp contact, the disk has axisymmetric motion during the op-shock. In such a deformation the disk's radial slope increases monotonically with the shock amplitude, and there is no circumferential slope. But when the disk collides with the LUL ramp, it introduces a 2D curvature in the disk's surface. This changes the monotonic behavior of the radial slope and also introduces a circumferential slope in the disk. The presence of

Table 5.6: Variation of contact force with shock amplitude

Ramp : Absent		Ramp : Present	
1410 G	0.046 mN	270 G	0.05 mN
1420 G	0.049 mN	280 G	101.34 mN
1430 G	0.052 mN	290 G	12.09 mN
1440 G	0.281 mN	300 G	22.44 mN
1450 G	0.388 mN	310 G	164.56 mN

the dual disk slopes in a spinning disk and its non-monotonic behavior explains the variation of contact force.

Shock resistance is used as a measure to determine the reliability of a mobile disk drive. In this study it is defined as the minimum shock amplitude at which the HDI fails. Fig. 5.11 shows the shock resistance as a function of the excitation pulse width. In the absence of the LUL ramp constraint, for pulse widths less than or equal to 0.5 ms, the shock resistance is independent of HDD orientation. In this range HDI failure occurs due to excitation of the HGA bending mode. At larger pulse widths the shock resistance is higher in the negative direction. This is because an air bearing in compression offers higher resistance to HDI failure. The shock resistance achieves its minimum value at a pulse width of 0.5 ms (1000 Hz) due to its proximity with the disk's (0,0) modal frequency.

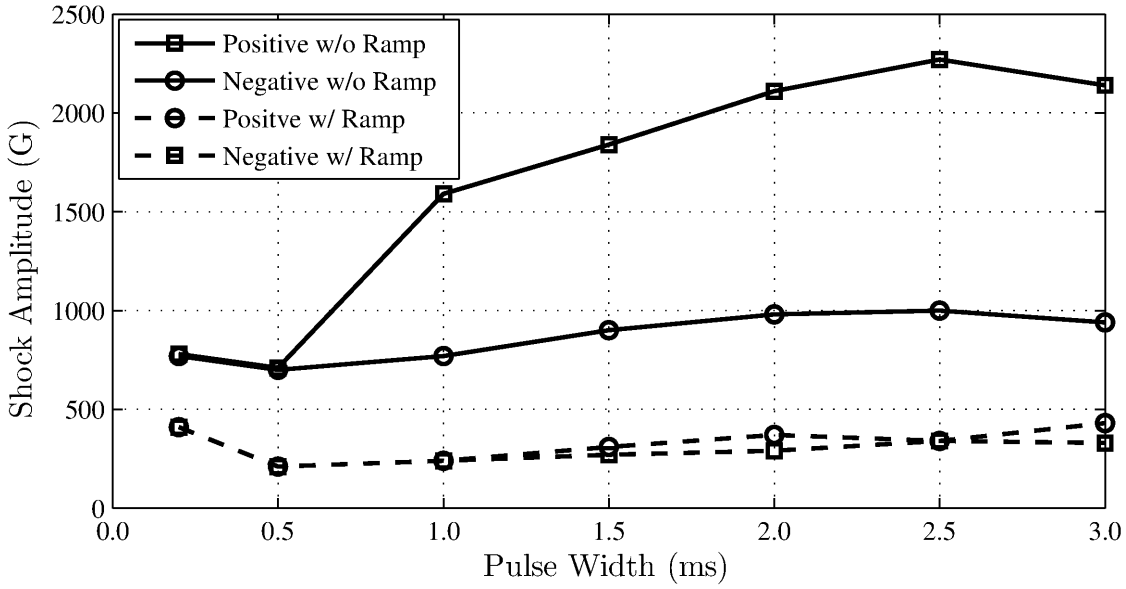

Figure 5.11: Variation of shock resistance with pulse width

The collision of the disk with the parking ramp reduces the shock resistance of a HDD. During the contact the disk's high frequency asymmetric modes get excited and destabilize the HDI causing its failure. In the HDD model studied here, LUL ramps are present on either side of the disk at equal distances. Due to such ramp placement the disk collides with a ramp at the same shock amplitude irrespective of HDD orientation. Hence the presence of parking ramps in a HDD reduces its sensitivity to the shock direction.

5.5 Effect of Spindle Motor

In this section, we discuss the effect of spindle motor dynamics on the HDI shock resistance. In order to eliminate the effect of base plate flexibility on the disk response, we fixed the motor housing to a rigid base. During the investigation it was found that the motor dynamics does not change the HDI failure mechanism during operation. However, it causes a uniform shift in the shock resistance for a pulse width greater than 0.5 ms as shown in Fig. 5.12. This change in shock resistance can be explained with the aid of a schematic diagram shown in Fig. 5.13. When a disk is mounted on a spindle motor the net stiffness of the system (K_{motor}) is lower as compared to the case when it is mounted to a rigid base (K_{rigid}). In the case of a positive shock, the HDI failure occurs due to the head slap phenomenon explained in the previous section. When the disk support system flexibility increases, higher shock amplitude is required to break the air bearing. Hence in this orientation, the motor mounting increases the shock resistance. However, the HDI failure during a negative shock occurs when the inertia forces exceed the resistive air bearing pressure. Due to the reduced stiffness of the support system, the motor-disk-air bearing system offers less resistance and hence failure occurs at lower shock amplitude.

Fig. 5.14(a) shows the effect of flexible disk mounting on the disk's transverse displacement during the disk-ramp contact. For a better understanding the rotor dynamics, we show the displacements of the four nodes located at the disk-hub interface (axi-symmetrically around the disk inner radius) in Fig. 5.14(b). The response for the rotating hub can be captured by plotting the displacements of the interface nodes relative to the hub center as shown in Figs. 5.14(c) and (d). It can be observed that the displacement of opposite nodes are mirror images of each other, which means that during the collision, the hub moves as a rigid body inside the the motor housing. This causes the rotating disk - hub assembly to wobble about its axis of rotation resulting in higher disk displacement as shown in Fig. 5.14(a).

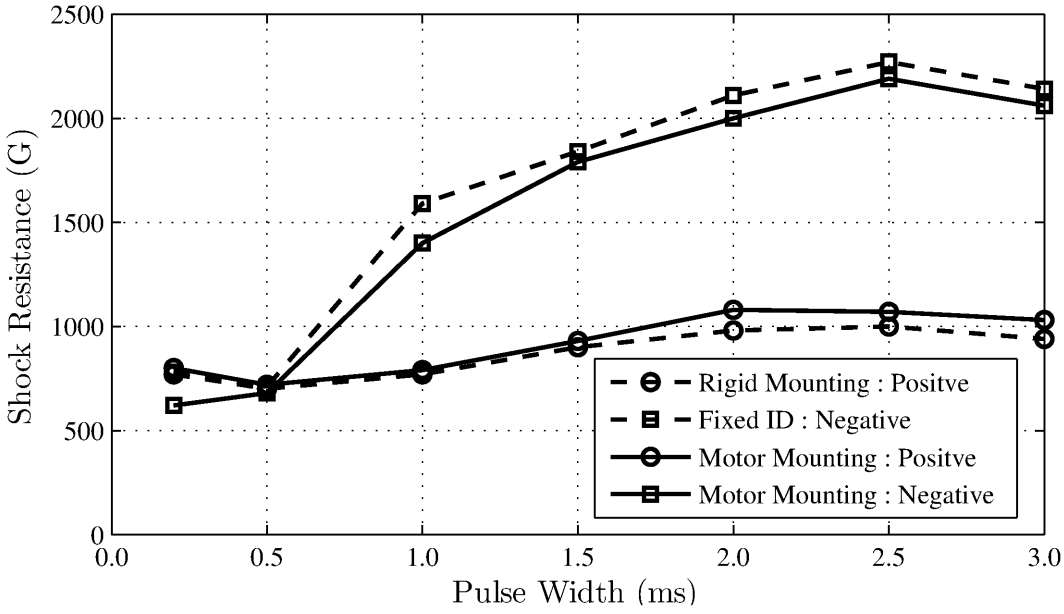

Figure 5.12: Effect of spindle motor support on the HDI shock resistance

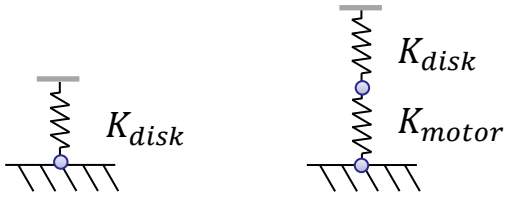

Figure 5.13: Schematic diagram showing the effect of motor flexibility

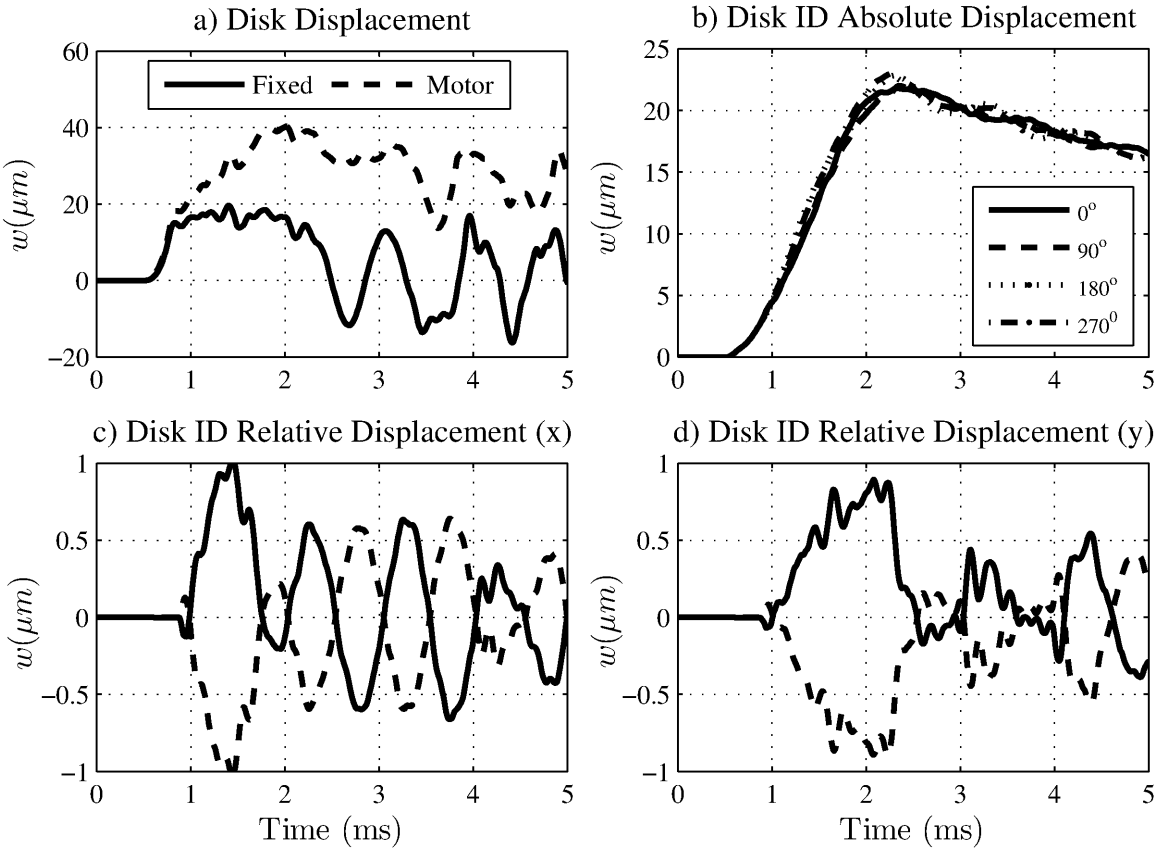

Figure 5.14: Wobbling of the rotating hub due to disk-ramp collision

Fig. 5.15 shows the variation of the shock resistance in the presence of a L/UL ramp. As discussed before, in the presence of a parking ramp the HDI is less sensitive to the shock direction. Hence, for simplicity, only the variation for positive shock is shown in Fig. 5.15. As discussed before, the cause of HDI failure in the current setup is the disk-ramp collision that excites the high frequency air bearing modes. For a disk mounted on a flexible spindle motor, the disk contact with the stationary ramp occurs at lower shock amplitude. However, flexible motor mounting does not cause a significant drop in the shock resistance due to the motor mounting. This is because the ramp contact at lower shock amplitude gets compensated by the absorption of the collision energy by the fluid dynamic bearing during the hub wobbling.

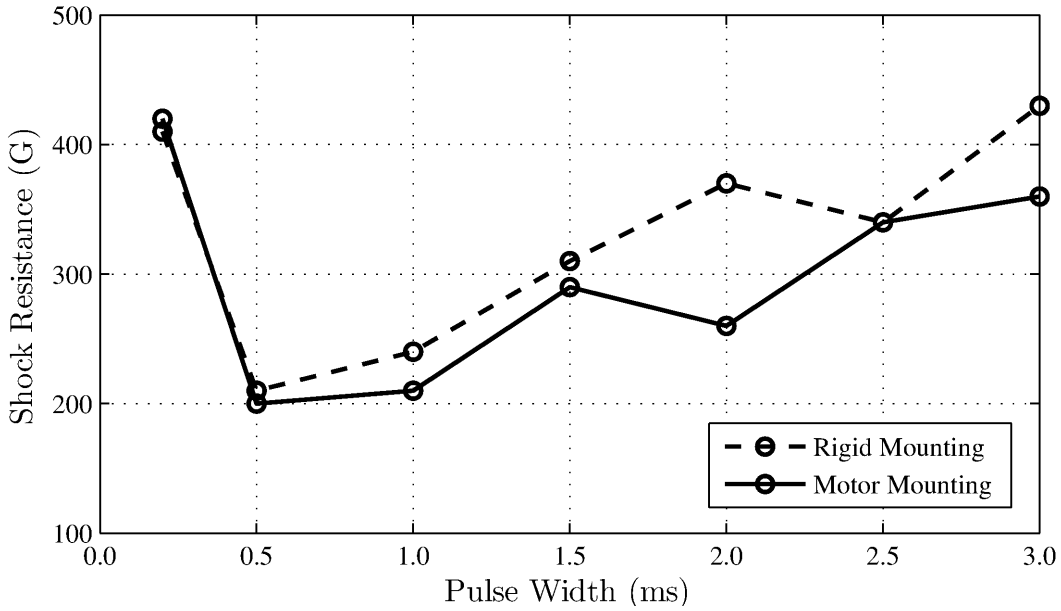

Figure 5.15: Variation of shock resistance in presence of L/UL ramp

5.6 Effect of Base Plate Flexibility

In this section we present the results from a numerical study conducted to investigate the effect of base plate flexibility on the shock performance of a HDI. The op-shock simulations were conducted on a complete HDD model. During the simulation the base plate was fixed to a rigid base using the mounting provided on its periphery (Fig. 3.6). Fig. 5.16 shows the disk response to a shock pulse of 200G magnitude and 2.0 ms for two different disk support systems. It can be observed that the increase in the disk support system flexibility due to

the base plate not only increases the amplitude of disk vibration (Fig. 5.16(a)), but also changes its frequency response (Fig. 5.16(b)).

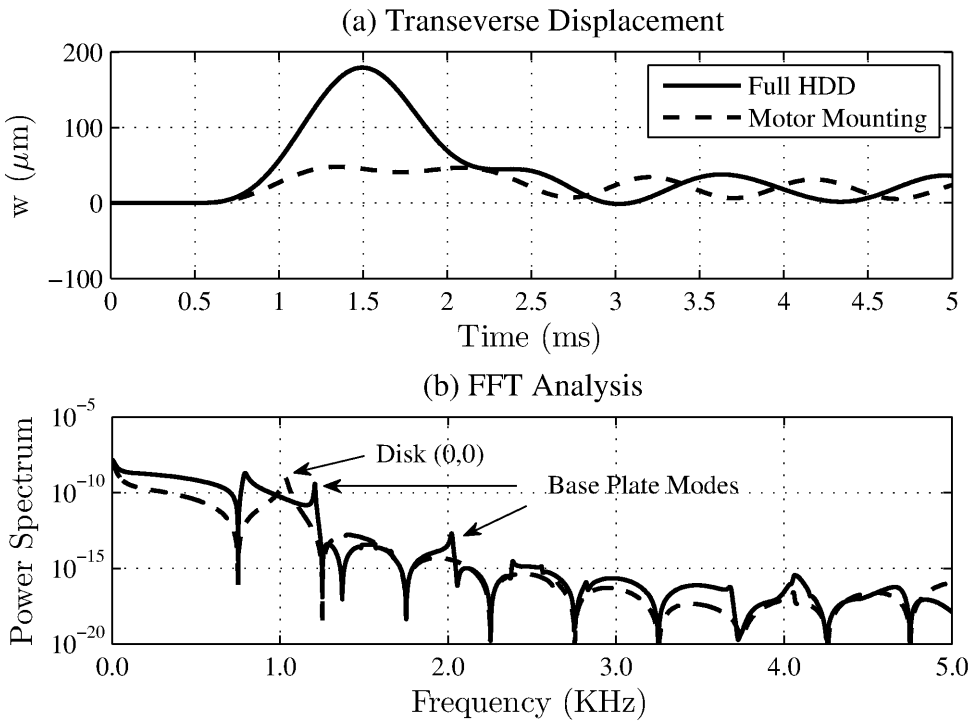

Figure 5.16: Effect of base plate flexibility on the disk transverse response

Fig. 5.17 compares the variation of HDI shock resistance for the two different disk support systems. It can be observed that, in the absence of a LUL ramp in the HDD, mounting the spindle motor on a base plate results in a lower shock resistance for both shock orientations (Fig. 5.17(a)). This decrease in shock resistance is caused by the excitation of the disk's modes with non-zero circumferential slope resulting from the asymmetric design of the base plate. When a slider is located near the disk OD, it lies along the disk's circumferential direction. During a positive shock, the slider moves away from the disk causing the collapse of air bearing which leads to the HDI failure. As shown in Fig. 5.18(a), a non-zero circumferential slope results in higher separation between the slider and disk, and hence it requires a lower shock amplitude to decouple the slider and disk motion, causing the HDI failure. In the case of a negative shock, the HDI failure occurs when the slider gets pushed towards the spinning disk resulting in high impact forces due to the surface contact. However, when the disk's slope along the slider's length is non-zero, the slider's edge gets into contact with the disk causing high impact forces (Fig. 5.18(b)). Edge contact happens at a lower shock

amplitude as compared to the surface contact, which results in lower shock resistance.

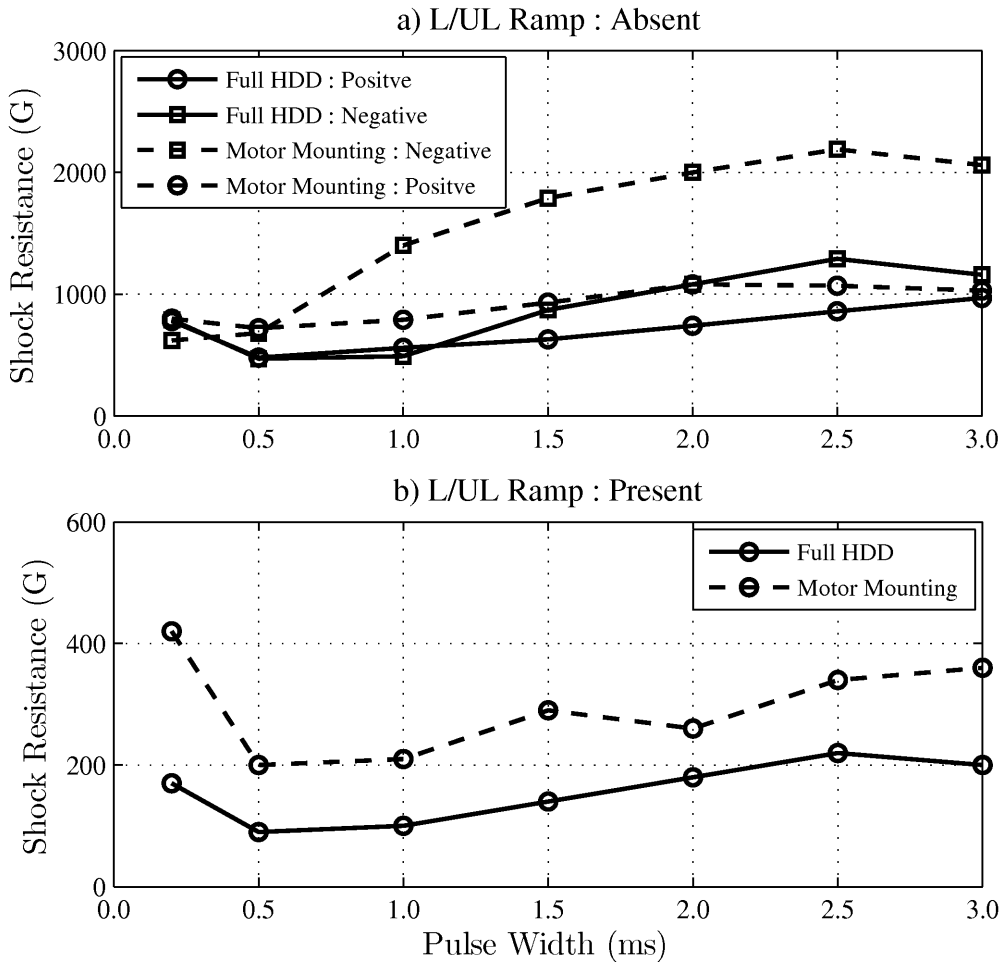

Figure 5.17: Effect of base plate flexibility on the shock resistance

Fig. 5.17(b) shows the effect of the base plate mounting on the shock resistance, in the presence of parking ramps. The significant decrease in the HDI shock resistance is a direct consequence of the increased flexibility of the disk support system. The disk-ramp collision that causes the HDI failure occurs at a lower shock amplitude for a disk supported by a more flexible system.

5.7 Closure

A numerical investigation was conducted to understand the effects of component dynamics and excitation frequency on the failure mechanism of a head-disk interface during an

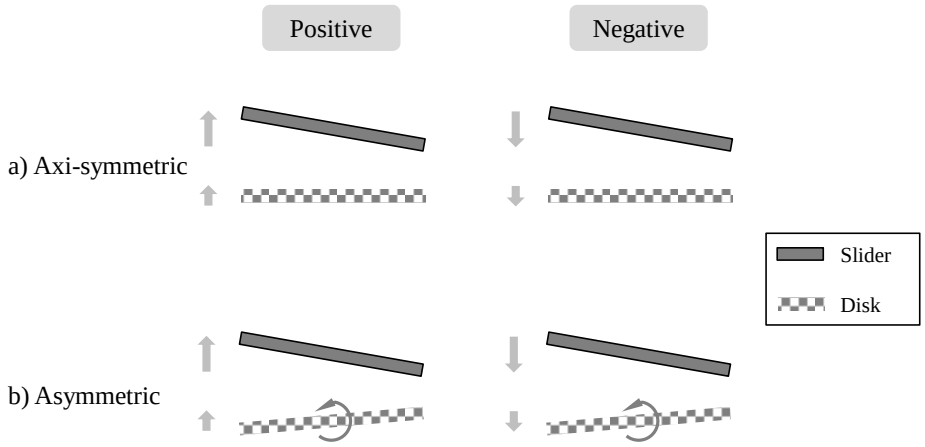

Figure 5.18: Effect of disk asymmetric vibration on the HDI failure mechanism

operational shock. It was found that the proximity of the pulse width (excitation frequency) to the HDD components' natural frequencies reduces its shock resistance. At a given pulse width the HDI offers better shock resistance in compression, i.e. negative shock, when the LUL ramp is absent. However, the presence of the parking ramp lowers the shock resistance, and it becomes independent of the shock direction. The rotor dynamics of the spindle motor does not have much effect on the HDI failure mechanism; however the deformation of the FDB during the shock causes a uniform change in shock resistance. The inclusion of a base plate in the disk support model has an adverse effect on the HDI shock performance which is due to the excitation of disk asymmetric modes. This knowledge about the HDI failure mechanism can help to improve the HDD design for better op-shock performance.

Chapter 6

Study of off-track slider vibration in a laptop HDD

The advancement in processing power in low energy rated CPUs has made applications such as gaming and high-definition multimedia popular on the laptop PCs. For a better experience, these laptops are often accompanied by a powerful built-in speaker. Components present in high end laptops such as multiple cooling fans, built-in speakers and a Blu-ray player excite the HDD and hence can degrade its R/W performance.

Several numerical investigations [Eguchi 2009; Hu et al. 2009] have been conducted in order to understand the HDI's response to an external disturbance. These studies have used a detailed model for the HDD structural components. However the air bearing was represented by a linear spring-damper system. In this study, we use a complete model for a mobile HDD to investigate the effect of excitation frequency and its orientation on the HDI vibration performance during an external disturbance.

6.1 Formulation

The disturbance produced by the laptop components can be represented by an acceleration pulse defined by its components $(\ddot{u}_{HDD}, \ddot{v}_{HDD}, \ddot{w}_{HDD})^T$. This excitation pulse is defined in the stationary HDD frame of reference. However, in order to impose the inertia loading on the actuator assembly, we must transform the acceleration vector to the rotating frame fixed to the E-block as shown in Fig. 6.1.

The relationship between the displacements $(u_{HDD}, v_{HDD}, w_{HDD})^T$ in the HDD stationary

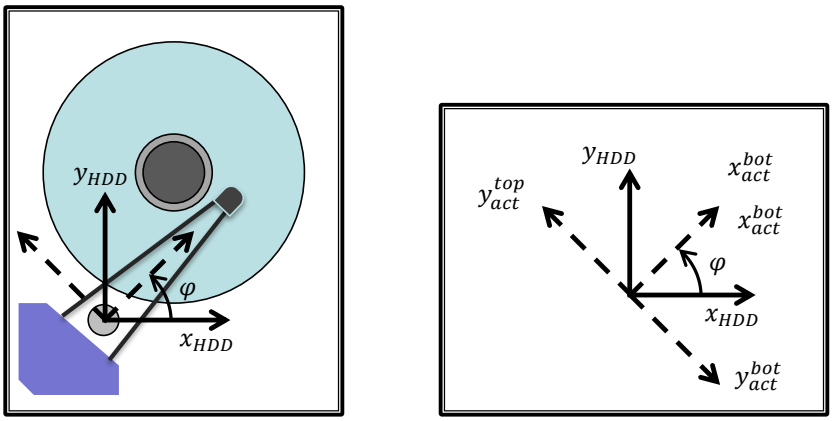

a) HDD Schematic b) Orientation

Figure 6.1: A schematic diagram explaining the orientation of actuator assembly

frame and actuator rotatory frame $(u_{act}, v_{act}, w_{act})^T$ is given as:

$$\begin{Bmatrix} u_{act}^{top} \\ v_{act}^{top} \\ w_{act}^{top} \end{Bmatrix} = \begin{bmatrix} \cos\phi & \sin\phi & 0 \\ -\sin\phi & \cos\phi & 0 \\ 0 & 0 & 1 \end{bmatrix} \begin{Bmatrix} u_{HDD} \\ v_{HDD} \\ w_{HDD} \end{Bmatrix} \tag{6.1a}$$

$$\begin{Bmatrix} u_{act}^{bot} \\ v_{act}^{bot} \\ w_{act}^{bot} \end{Bmatrix} = \begin{bmatrix} \cos\phi & \sin\phi & 0 \\ \sin\phi & -\cos\phi & 0 \\ 0 & 0 & 1 \end{bmatrix} \begin{Bmatrix} u_{HDD} \\ v_{HDD} \\ w_{HDD} \end{Bmatrix} \tag{6.1b}$$

where ϕ is the angular separation between the actuator and HDD coordinate frames (Fig. 6.1). The superscripts *top* and *bot* are used for the actuator assemblies present on the top and bottom of the spinning disk. If the actuator is stationary, i.e. it is not undergoing any seek operation ($\dot{\phi} = \ddot{\phi} = 0$), the transformation of the acceleration pulse is:

$$\begin{Bmatrix} \ddot{u}_{act}^{top} \\ \ddot{v}_{act}^{top} \\ \ddot{w}_{act}^{top} \end{Bmatrix} = \begin{bmatrix} \cos\phi & \sin\phi & 0 \\ -\sin\phi & \cos\phi & 0 \\ 0 & 0 & 1 \end{bmatrix} \begin{Bmatrix} \ddot{u}_{HDD} \\ \ddot{v}_{HDD} \\ \ddot{w}_{HDD} \end{Bmatrix} \tag{6.2a}$$

$$\begin{Bmatrix} \ddot{u}_{act}^{bot} \\ \ddot{v}_{act}^{bot} \\ \ddot{w}_{act}^{bot} \end{Bmatrix} = \begin{bmatrix} \cos\phi & \sin\phi & 0 \\ \sin\phi & -\cos\phi & 0 \\ 0 & 0 & 1 \end{bmatrix} \begin{Bmatrix} \ddot{u}_{HDD} \\ \ddot{v}_{HDD} \\ \ddot{w}_{HDD} \end{Bmatrix} \tag{6.2b}$$

6.2 Generalized Excitation

The disturbance on the laptop is represented by a *Gaussian* white noise wave as shown in Fig. 6.2. The excitation pulse is characterized by its peak-to-peak amplitude A and the cut-off frequency f. It was observed that during an external disturbance, the variation in the slider's flying height was negligible in comparison to its in-plane vibration. Hence the slider's *off-track* displacement (Fig. 6.3) is chosen to evaluate the HDI vibration performance during the external disturbance. In this study, the HDI off-track vibration is defined as the relative in-plane displacement between the slider and the disk along the disk radius.

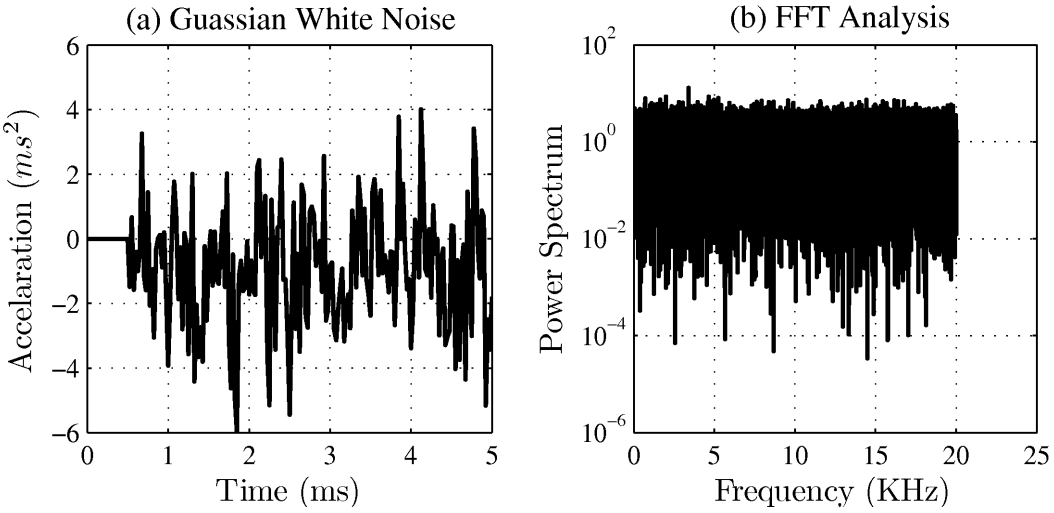

Figure 6.2: Gaussian white noise ($A = 10$ ms^{-2}; $f = 20$ KHz)

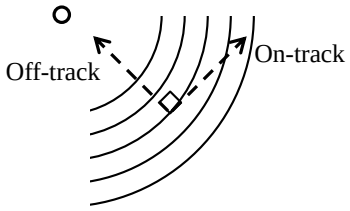

Figure 6.3: Decomposition of slider's in-plane displacement into *off-track* and *on-track* displacements

The laptop HDD is subjected to a white noise excitation of bandwidth 20 KHz along its X, Y and Z axis (Fig. 6.1). Fig. 6.4 shows the variation of the HDI's off-track vibration with the excitation amplitude. The slider's response shown here is normalized with the track

width (150 nm). It can be observed that the 3σ variation in off-track vibration exhibits a non-linear relationship with the excitation amplitude. This means that representing the air bearing by linear spring-dashpot system [Eguchi 2009; Hu et al. 2009] would not be a good approximation in the current analysis.

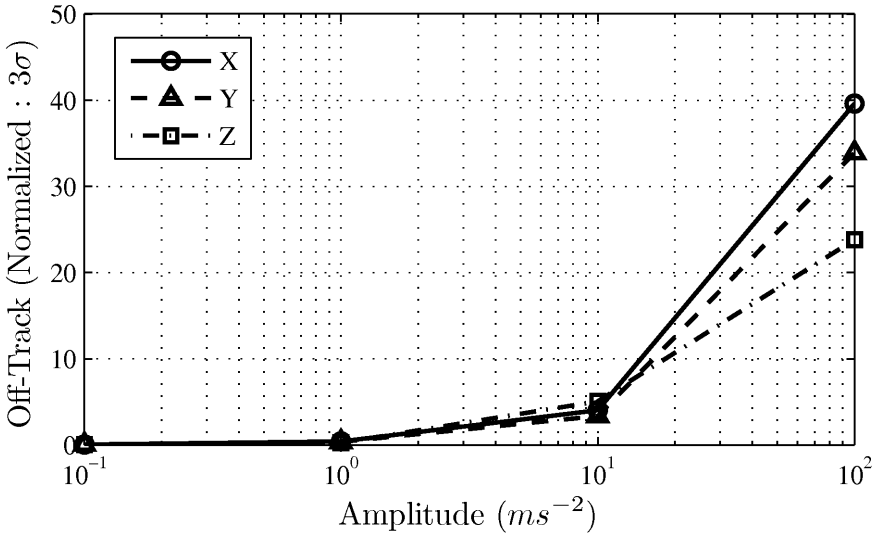

Figure 6.4: Variation of HDI's off-track vibration with excitation amplitude

6.3 Effect of Excitation Orientation

To understand the effect of the orientation of the disturbance relative to the HDD, we subject the HDD to a series of harmonic excitations of different frequencies but constant amplitude (10ms^{-2}). Fig. 6.5 shows the variation of the off-track vibration with the excitation frequency for three different orientations. For a vertical excitation (Z), the frequency peak appears at 1000Hz. However, for disturbances in the disk plane, the slider's off-track vibration attains its maxima at frequencies higher than 5000 Hz.

This change in the slider's behavior can be attributed to the suspension dynamics. For a better understanding, we subject the HDD to a white noise excitation ($A = 10$ ms^{-2}; $f =$ 20 kHz) in three mutually perpendicular directions. Fig. 6.6 shows the frequency spectrum of the slider's off-track displacement during the dynamic event. For an in-plane disturbance, the peak frequency corresponds to the twisting mode of the suspension, which occurs around 4000 Hz. However during an axial excitation, the suspension's bending mode dominates the

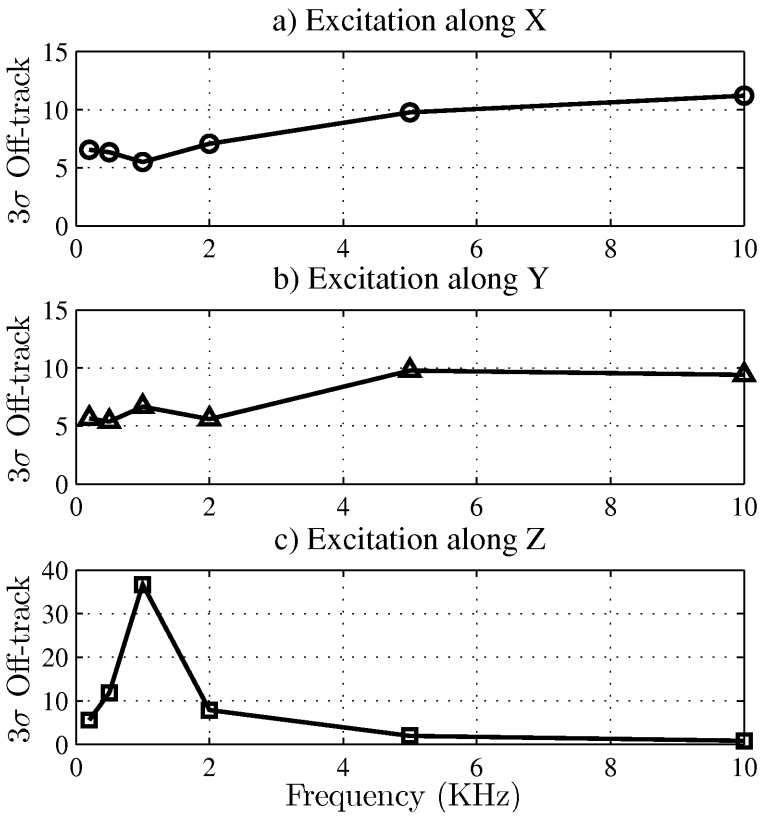

Figure 6.5: Effect of excitation direction on slider's vibration

slider's response. This change in the HGA excitation mode with the direction is responsible for the HDI's behavior shown in Fig. 6.5.

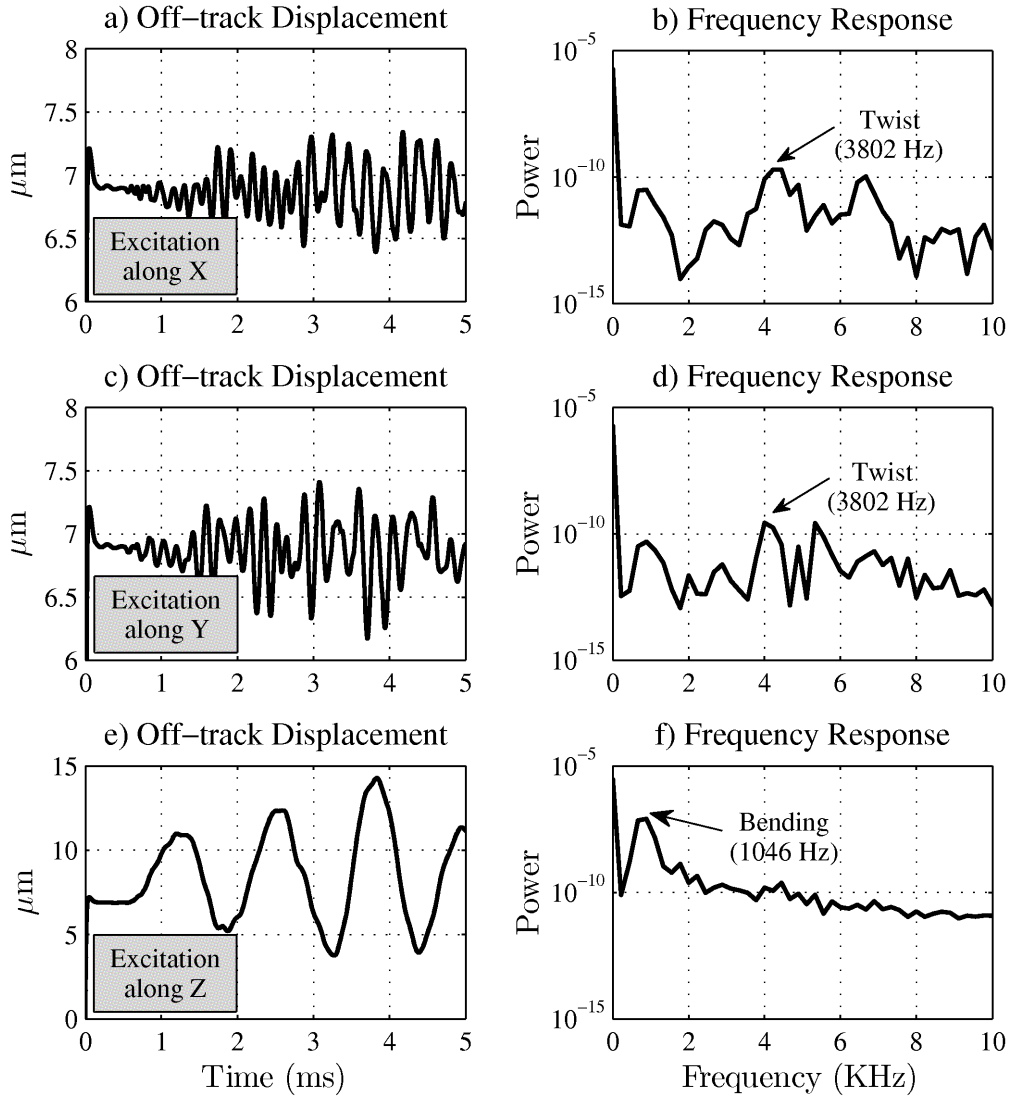

Figure 6.6: Frequency response of slider's off-track displacement

6.4 Effect of Spindle Motor

To understand the effect of the rotor dynamics on the HDI vibration performance, we subjected the HDD to a planar disturbance ($A = 10$ ms^{-2}; $f = 20$ kHz) along the x direction. It can be observed (Fig. 6.7) that the contribution of the disk's displacement to the off-track vibration was much smaller as compared to the slider's displacement. The damping of the

low frequency excitation by the FDB present in the spindle motor is responsible for this behavior.

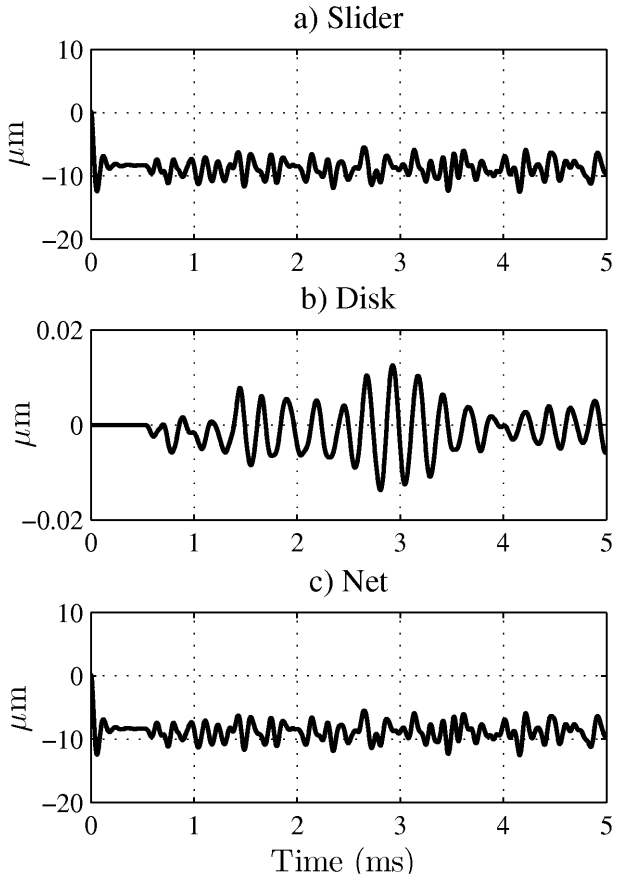

Figure 6.7: HDD off-track response to white noise vibration along X axis

6.5 Closure

A numerical study was conducted to examine the effect of excitation frequency and its direction on the slider's off-track vibration. It was found that the direction of the excitation determines the HGA dynamics, and hence it affects the frequency response of the slider's off-track vibration. The better damping performance by the FDB spindle motor helps improve the vibration performance of the HDI. This knowledge about the vibration characteristics of mobile drives can be used to design better vibration isolation systems for mounting of HDDs in a laptop.

Chapter 7

Conclusions and Future Work

7.1 Conclusions

Over the past decade, there has been a huge increase in the demand for hard disk drives for consumer electronics applications such as digital video recorders and laptop PCs. The reliability of a HDD in such devices depends on its ability to withstand the external disturbances it is subjected to while operating in a harsh environment. In this dissertation we present a comprehensive model for a mobile HDD that can accurately capture the head-disk interface dynamics during an event of a shock or a vibration to aid the design process.

In this study, we developed a detailed model for the disk support system that includes a spinning disk, a FDB based spindle motor and a flexible base plate. The Finite Element method is used to model the structural components in the system. The current model has a capability of predicting the disk's response during its collision with the stationary L/UL ramp. To save computational efforts, the FDBs are represented by a spring-dashpot system whose dynamic coefficients are evaluated using perturbation of the Reynold's lubrication equation. Furthermore, the computational efficiency of the simulator is improved by implementing a reduced FE scheme to decrease the degree of freedoms present in complex structural units such as base plate, actuator assembly, etc. In order to predict the behavior of the HDI during a dynamic event, we coupled the response of the slider and the disk through an air bearing using a fixed-point iteration scheme. The forces resulting from the possible slider-disk contact are also considered while solving the force equilibrium problem.

A numerical investigation was conducted to understand the effects of component dynamics and excitation frequency on the failure mechanism of a head-disk interface during an

operational shock. It was found that the proximity of the pulse width (excitation frequency) to the HDD components' natural frequencies reduces its shock resistance. At a given pulse width the HDI offers better shock resistance in compression, i.e. negative shock, when the LUL ramp is absent. However, the presence of the parking ramp lowers the shock resistance, and it becomes independent of the shock direction. The rotor dynamics of the spindle motor does not have much effect on the HDI failure mechanism; however the deformation of the FDB during the shock causes a uniform change in shock resistance. The inclusion of a base plate in the disk support model has an adverse effect on the HDI shock performance that is due to the excitation of disk asymmetric modes. This knowledge about the HDI failure mechanism can help to improve the HDD design for better op-shock performance.

In another study, a HDD used in a laptop was evaluated for its vibration performance. It was found that the slider's dynamics during an external disturbance depends on its orientation relative to the HDD, and hence it affects the frequency response of the HDI's off-track vibration. The better mechanical damping offered by hydrodynamic bearing used in the spindle motor, helps to improve the vibration performance of the HDI.

The simulation tool (*CML op-shock simulator*) developed as the part of this research has been made available to the industrial members of the Computer Mechanics Laboratory (CML) [CML]. This *op-shock* simulator is currently used in the hard drive industry to evaluate the shock performance of a mobile HDD (private communications).

7.2 Future Work

The HDD model developed in the current study contains much detail. However, there is still some scope for further improvement.

In this analysis, we assumed that the actuator assembly is fixed to a rigid base. However, in a real HDD, the E-block is mounted on an actuator pivot attached to the base plate. During an in-plane excitation, the deformation of the bearings at the actuator pivot can affect the slider's response, and hence its is required to couple the actuator assembly response with the base plate.

We have represented the FDB present in a spindle motor with a linear spring-dashpot system. This linear system is a good approximation in the case of an axial shock where the in-plane displacement of the rotor is small. However during a planar disturbance, a significant change in the shaft position inside the sleeve introduces non-linearity in FDB

behavior. Furthermore, during such events there is also a possibility of metal to metal contact between the shaft and its sleeve. For better accuracy in predicting the HDI response in such situations, it is important to model the non-linearity present in a system.

Currently most of the commercial HDDs use a thermally flying controlled slider for low clearance magnetic recording. In order to extend the current simulator to predict HDI dynamics for TFC sliders, it is required to model the thermal deformation of the slider during the heater operation.

Another direction for future research can be the experimental validation of the current simulation study. A good correlation between two sets of results will improve the credibility of the *op-shock* simulator.

Bibliography

S. H. Advani and P. Z. Bulkeley. Non-linear transverse vibrations and waves in spinning membrane discs. *International Journal of Non-Linear Mechanics*, 4(2):123–127, 1969.

M. Albrecht, C. T. Rettner, A. Moser, M. E. Best, and B. D. Terris. Recording performance of high-density patterned perpendicular magnetic media. *Applied Physics Letters*, 81(15): 2875–2877, 2002.

ANSYS. *ANSYS 11.0 Documentation*, 2010.

R. Baddour and J. W. Zu. A revisit of spinning disk models. Part I: derivation of equations of motion. *Applied Mathematical Modelling*, 25(7):541–559, 2001a.

R. Baddour and J. W. Zu. A revisit of spinning disk models. Part II: Linear transverse vibrations. *Applied Mathematical Modelling*, 25(7):561–578, 2001b.

R. C. Benson and D. B. Bogy. Deflection of a very flexible spinning disk due to a stationary transverse load. *ASME Journal of Applied Mechanics*, 45(3):636–642, 1978.

P. Bhargava and D. B. Bogy. Numerical Simulation of Operational-Shock in Small Form Factor Hard Disk Drives. *ASME Journal of Tribology*, 129(1):153–160, 2007.

Puneet Bhargava. *Numerical simulation of the head-disk interface in hard disk drives*. PhD thesis, University of California, Berkeley, 2008.

W. L. Briggs, V. E. Henson, and S. F. McCormick. *A Multigrid Tutorial*. Society for Industrial and Applied Mathematics, 2 edition, 2000.

D. Chen and D. B. Bogy. Comparisons of slip-corrected Reynolds lubrication equations for the air bearing film in the head-disk interface of hard disk drives. *Microsystem Technologies*, 37(2):191–201, 2010.

CML. CML Air Bearing Design Program. http://cml.berkeley.edu/cmlair.html, 2011.

C. D'Angelo. *Vibration and Aeroelastic stability of a Disk Rotating in a Fluid*. PhD thesis, UC Berkeley, 2001.

E. D. Daniel, C. D. Mee, and M. H. Clark. *Magnetic Recording – The first 100 years*. IEEE Press, New York, 1999.

T. Eguchi. Simulation of position error signal degradation due to operational vibration for hard disk drives in a storage server box. *IEEE Transactions on Magnetics*, 45(11): 5162–5167, 2009.

W. Eversman. Transverse vibrations of a clamped spinning membrane. *AIAA Journal*, 6(7): 1395–1397, 1968.

W. Eversman and R. O. Dodson. Free vibration of a centrally clamped spinning circular disk. *AIAA Journal*, 7(10):2010–2012, 1969.

M. I. Friswell, S. D. Garvey, and J. E. T. Penny. Model reduction using dynamic and iterated IRS techniques. *Journal of Sound and Vibration*, 186(2):311–323, 1995.

S. Fukui and R. Kaneko. A database for interpolation of Poiseuille flow rates for high Knudsen number lubrication problems. *ASME Journal of Tribology*, 112(1):78–83, 1990.

J. A. Greenwood and J. B. P. Williamson. Contact of nominally flat surfaces. *Proceedings of the Royal Society of London. Series A, Mathematical and Physical Science*, 295(1442): 300–319, 1966.

V. Gupta and D. B. Bogy. Effect of intermolecular forces on the static and dynamic performance of air bearing sliders: Part i - effect of initial excitations and slider form factor on the stability. *ASME Journal of Tribology*, 128(1):197–202, 2006a.

V. Gupta and D. B. Bogy. Effect of intermolecular forces on the static and dynamic performance of air bearing sliders: Part ii - dependence of the stability on hamaker constant, suspension preload and pitch angle. *ASME Journal of Tribology*, 128(1):203–208, 2006b.

R. J. Guyan. Reduction of stiffness and mass matrices. *AIAA Journal*, 3(2):380–380, 1965.

J. C. Harrison and M. D. Mundt. Flying height response to mechanical shock during operation of a magnetic hard disk drive. *ASME Journal of Tribology*, 122(1):260–263, 2000.

Hitachi. HDD roadmap. https://www1.hitachigst.com/hdd/hddpdf/tech/hdd_technology2003.pdf, 2003.

Hitachi. Fluid dynamic bearing spindle motors: Their future in hard disk drives. http://hgst.com/hdd/travel/fdbwhitepaper.pdf, 2007a.

Hitachi. Perpendicular magnetic recording technology. http://www.hitachigst.com/tech/techlib.nsf/techdocs/F47BF010A4D29DFD8625716C005B7F34/$file/PMR_white_paper_final.pdf, 2007b.

Hitachi. Ramp Load/Unload Technology in Hard Disk Drives. http://www.hitachigst.com/tech/techlib.nsf/techdocs/9076679E3EE4003E86256FAB005825FB/$file/LoadUnload_white_paper_FINAL.pdf, 2007c.

Y. Y. Hu, S. Yoshida, S. Nakamura, K. Watanabe, W. Z. Lin, E. T. Ong, and J. Q. Mou. Analysis of built-in speaker-induced structural-acoustic vibration of hard disk drives in notebook PCs. *IEEE Transactions on Magnetics*, 45(11):4950–4955, 2009.

T. J. R. Hughes, R. L. Taylor, J. L. Sackman, A. Curnier, and W. Kanoknukulchai. A finite element method for a class of contact-impact problems. *Computer Methods in Applied Mechanics and Engineering*, 8(3):249–276, 1976.

IBM. Ibm 350 disk storage unit. http://www-03.ibm.com/ibm/history/exhibits/storage/storage_350.html, April 2011.

IDEMA. http://www.idema.org/, 2011.

INSIC. http://www.insic.org, 2010.

W. D. Iwan and K. J. Stahl. The response of an elastic disk with a moving mass system. *ASME Journal of Applied Mechanics*, 40(2):445–451, 1973.

G. H. Jang and S. Lee. Determination of the dynamic coefficients of the coupled journal and thrust bearings by the perturbation method. *Tribology Letters*, 22(3):239–246, 2006.

G. H. Jang and C. H. Seo. Finite-element shock analysis of an operating hard disk drive considering the flexibility of a spinning disk-spindle, a head-suspension-actuator, and a supporting structure. *IEEE Transactions on Magnetics*, 43(9):3738–3743, 2007.

G. H. Jang and J. W. Yoon. Nonlinear dynamic analysis of a hydrodynamic journal bearing considering the effect of a rotating or stationary herringbone groove. *ASME Journal of Tribology*, 124(2):297–304, 2002a.

G. H. Jang and J. W. Yoon. Dynamic characteristics of a coupled journal and thrust hydrodynamic bearing in a HDD spindle system due to its groove location. *Microsystem Technologies*, 8(4-5):261–270, 2002b.

G. H. Jang, J. H. Han, and C. H. Seo. Finite element modal analysis of a rotating diskspindle system in a HDD with hydrodynamic bearings considering the flexibility of a complicated supporting structure. *Microsystem Technologies*, 11(7):488–498, 2005.

G. H. Jang, C. H. Seo, and H. S. Lee. Finite element modal analysis of an HDD considering the flexibility of spinning diskspindle, headsuspensionactuator and supporting structure. *Microsystem Technologies*, 13(8-10):837–847, 2006.

E. M. Jayson, J. M. Murphy, P. W. Smith, and F. E. Talke. Effects of air bearing stiffness on a hard disk drive subject to shock and vibration. *ASME Journal of Tribology*, 125(02): 343–349, 2003a.

E. M. Jayson, P. W. Smith, and F. E. Talke. Shock modeling of the head-media interface in an operational hard disk drive. *IEEE Transactions on Magnetics*, 39(05):2429–2431, 2003b.

Z. W. Jiang, K. Takashima, and S. Chonan. Shock-proof design of head disk assembly subjected to impulsive excitation. *JSME International Journal, Series C*, 38(3):411–419, 1995.

M. C. Katona and O. C. Zienkiewicz. A unified set of single step algorithms. Part 3: The beta-m method, a generalization of the Newmark scheme. *International Journal for Numerical Methods in Engineering*, 21(7):1345–1359, 1985.

J. D. Kiely and Y. T. Hsia. Tribocharging of the magnetic hard disk drive headdisk interface. *Journal of Applied Physics*, 91(7):4631–4636, 2002.

S. Kirpekar. *Computing turbulence induced vibrations in hard disk drives.* PhD thesis, UC Berkeley, 2006.

T. Kouhei, T. Yamada, Y. Keroba, and K. Aruga. A study of head-disk interface shock resistance. *IEEE Transactions on Magnetics*, 31(06):3005–3008, 1995.

M. H. Kryder, E. C. Gage, T. W. Mcdaniel, W. A. Challener, R. E. Rottmayer, G. Ju, Y. T. Hsia, and M. F. Erden. Heat Assisted Magnetic Recording. *Proceeding OF The IEEE*, 96 (11):1810–1835, 2008.

C. P. R. Ku. Dynamic characteristics of hard disk drive spindle motorscomparison between ball bearings and hydrodynamic bearings. *ASME Journal of Tribology*, 118(2):402–406, 1996.

S. Kumar, V.D. Khanna, and M. Sri-Jayantha. A study of the head disk interface shock failure mechanism. *IEEE Transactions on Magnetics*, 30(06):4155–4157, 1994.

M. Kurita, J. G. Xu, M. Tokuyama, K. Nakamoto, S. Saegusa, and Y Maruyama. Flying-height reduction of magnetic-head slider due to thermal protrusion. *IEEE Transaction on Magnetics*, 41(10):3007–3009, 2005.

H. Lamb and R. V. Southwell. The vibrations of a spinning disk. *Proceedings of the Royal Society of London. Series A, Containing Papers of a Mathematical and Physical Character*, 99(699):272–280, 1921.

H. Li and F. E. Talke. Numerical Simulation of the Head/Disk Interface for Bit Patterned Media. *IEEE Transaction on Magnetics*, 45(11):4984–4989, 2009.

C. C. Lin. Finite element analysis of a computer hard disk drive under shock. *ASME Journal of Mechanical Design*, 124(1):121–125, 2002.

Sha Lu. *Numerical simulation of slider air bearing.* PhD thesis, University of California, Berkeley, 1997.

A. I. Luré. *Theory of elasticity.* Springer, 1 edition, 2005.

L. Meirovitch. *Principles and Techniques of Vibration.* Prentice Hall, 1 edition, 1996.

T. L. Moeller and W. D. Iwan. The Stability of a Spinning Elastic Disk With a Transverse Load System. *ASME Journal of Applied Mechanics*, 43(3):485–490, 1976.

C. D. Mote. Stability of circular plates subjected to moving loads. *Journal of the Franklin Institute*, 290(4):329–344, 1970.

A. N. Murthy, M. Pfabe, J. Xu, and F. E. Talke. Dynamic response of 1-in. form factor disk drives to external shock and vibration loads. *Microsystem Technologies*, 13(8-10): 1031–1038, 2006.

S. M. Oh and Y. C. Rhim. The numerical snalysis of spindle motor bearing composed of herringbone groove journal and spiral groove thrust bearing. *KSTLE International Journal*, 2(2):93–102, 2001.

J. S. Park, I. Y. Shen, and C. P. R. Ku. A parametric study on rocking vibration of rotating disk/spindle systems with hydrodynamic bearings: rotating-shaft design. *Microsystem Technologies*, 8(6):427–434, 2002.

K. S. Park, Y. P. Park, and N. C. Park. Prospect of Recording Technologies for Higher Storage Performance. *IEEE Transaction on Magnetics*, 47(3):539–545, 2011.

S. Patankar. *Numerical Heat Transfer and Fluid Flow*. Taylor and Francis, 1 edition, 1980.

PC Guide. Construction and operation of the hard disk. http://www.pcguide.com/ref/hdd/op/index.htm, 2001.

R. E. Rottmayer, S. Batra, D. Buechel, W. A. Challener, J. Hohlfeld, Y. Kubota, L. Li, B. Lu, C. Mihalcea, K. Mountfield, K. Pelhos, C. Peng, T. Rausch, M. A. Seigler, D. Weller, and X. Yang. Heat-assisted magnetic recording. *IEEE Transaction on Magnetics*, 42(10): 2417–2421, 2006.

Seagate. Momentus® thin hard drives. http://www.seagate.com/www/en-us/products/laptops/slim-laptop-hard-drives, April 2011.

V. N. Shah and M. Raymund. Analytical selection of masters for the reduced eigenvalue problem. *International Journal for Numerical Methods in Engineering*, 18(1):89–98, 1982.

I. Y. Shen. Vibration of rotating-shaft HDD spindle motors with flexible stationary parts. *IEEE Transactions on Magnetics*, 39(2):794–799, 2003.

I. Y. Shen and C. P. R. Ku. A nonclassical vibration analysis of a multiple rotating disk and spindle assembly. *ASME Journal of Applied Mechanics*, 64(1):165–174, 1997.

J. Y. Shen, C. W. Tseng, and I. Y. Shen. Vibration of rotating disk/spindle systems with flexible housing/stator assemblies. *Journal of Sound and Vibration*, 271(3-5):725–756, 2004.

T. Shiramatsu, T. Atsumi, M. Kurita, Y. Shimizu, and H. Tanaka. Dynamically Controlled Thermal Flying-Height Control Slider. *IEEE Transaction on Magnetics*, 44(11, Part 2): 3695–3697, 2008.

Y. Shiroishi, K. Fukuda, I. Tagawa, H. Iwasaki, S. Takenoiri, H. Tanaka, H. Mutoh, and N. Yoshikawa. Future Options for HDD Storage. *IEEE Transaction on Magnetics*, 45(10, Sp. Iss. SI):3816–3822, 2009.

R. V. Southwell. On the free transverse vibrations of a uniform circular disc clamped at its centre; and on the effects of rotation. *Proceedings of the Royal Society of London. Series A, Containing Papers of a Mathematical and Physical Character*, 101(709):133–153, 1922.

Wikipedia. Hard disk drive. http://en.wikipedia.org/wiki/Hard_disk_drive, April 2011.

Q. H. Zeng and D. B. Bogy. Numerical simulation of shock response of disk-suspension-slider air bearing systems in hard disk drives. *Microsystem Technologies*, 8(4-5):289–296, 2002.